TEMPLATED GROWTH OF PEROVSKITE NANOSHEETS

By

MAYRA ALEJANDRA PEDRAZA

(Under the Direction of Tina T. Salguero)

ABSTRACT

Inorganic perovskites comprise a family of materials that can exhibit piezoelectric and ferroelectric properties. The nanostructuring of these materials is directly related to applications ranging from capacitors to non-volatile random-access memory. Here we describe a templated growth approach to synthesizing nanosheets of these materials, mainly focusing on $PbTiO_3$, $BaTiO_3$, and $SrTiO_3$. The template is $(TBA)_{1.07}Ti_{1.73}O_4$, a well-known 2D-nanostructured analog of TiO_2(B). Nanosheets of tetragonal $PbTiO_3$ were synthesized by a hydrothermal approach whereas nanosheets of $BaTiO_3$ and $SrTiO_3$ were synthesized by flux-based reactions. In this work, I detail optimized synthetic approaches, characterization studies, and initial work to understand the unique properties of these novel nanosheet materials.

INDEX WORDS: Nanosheets, Perovskites, Nanomaterials, $PbTiO_3$, $BaTiO_3$, $SrTiO_3$, ferroelectric, piezoelectric, templated growth.

TEMPLATED GROWTH OF PEROVSKITE NANOSHEETS

By

MAYRA ALEJANDRA PEDRAZA

B.S., The University of Texas at San Antonio, 2015

A Dissertation Submitted to the Graduate Faculty of the University of Georgia in Partial Fulfillment of the Requirements for the Degree

DOCTOR OF PHILOSOPHY

ATHENS, GEORGIA

2020

TEMPLATED GROWTH OF PEROVSKITE NANOSHEETS

By

MAYRA ALEJANDRA PEDRAZA

Major Professor: Tina T. Salguero

Committee: Jin Xie

Paul Schroeder

Electronic Version Approved:

Ron Walcott
Interim Dean of the Graduate School
The University of Georgia
August 2020

DEDICATION

For amazing fiancé and my loving and supporting family.

ACKNOWLEDGEMENTS

I first would like to thank my partner, who has been extremely supporting and understanding throughout the process of writing this thesis. My parents for always believing in my and supporting me to pursue my passions and dreams. My brother that has always being there for me when needed. My partner's mom Christy Craig for always encouraging me and supporting me. I would also like to thank Dr. Tina Salguero, for allowing me to work in her lab and being an amazing mentor and teacher. As well as my committee members Dr. Paul Schroeder and Dr. Jin Xie for helping me through graduate school. Finally, I would like to thank all the students that have been with me throughout the years in the Salguero group for always being helpful and encouraging.

TABLE OF CONTENTS

CHAPTER I

INTRODUCTION TO PEROVSKITE MATERIALS AND LITERATURE REVIEW

Perovskite materials

Perovskites are a class of materials that possess the formula ABO_3, with the first known perovskite being calcium titanium oxide $CaTiO_3$ (mineral name is perovskite). It is a structure that most metal oxides adopt; a cubic unit cell of such a compound has the 'A' atoms sits at the corners of the cube, the 'B' atoms are in the body center position and the 'O' (oxygen) atoms are in the face center positions, as can be observed in **Figure 1.1**.

This group of materials gained more attraction during WWII when there was a need for a better insulator for capacitors, prompting scientists to find a substitute dielectric material, and, before long, they discovered $BaTiO_3$.[2] This titanate is still widely used as a dielectric material, displacing the previously used mica.

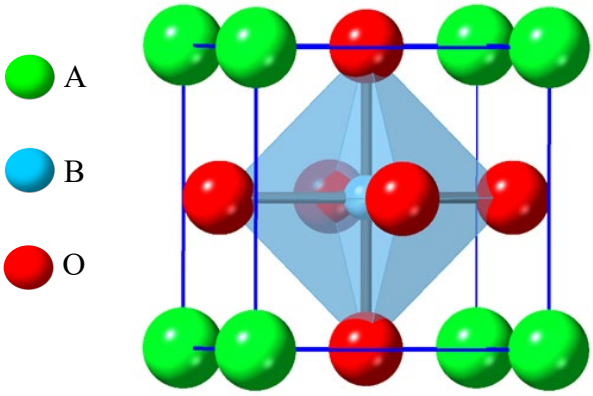

Figure 1.1. Perovskite crystal structure

However, that is not the only useful application for these types of materials. Perovskite materials are dielectric materials that, given their unique structure, can possess different properties that range from piezoelectricity to ferroelectricity because the center or 'B' atom on the structure remains in place, while the different sizes of 'A' atoms make the structure shift slightly upwards, creating an exaggerated dipole moment. This property of perovskites has been extensively studied,

as researchers come up with different compositions derived from this material. They can range from complex double perovskites (Aurivillius oxides) to organometallic halide perovskites.[3] Given all these reasons, my research focus is the synthesis and property studies of perovskite materials.

Dielectric materials

Dielectric materials are those that can be polarized under an electric field. This material will contain polar molecules with random orientations that will align when an electric field is applied, thus polarizing the material. These materials are also an electrical insulator; the difference with normal insulators is that dielectric materials can store energy. This property is very useful and dielectric materials are currently being used for capacitors and radio frequency transmission lines. Even with these applications, more and more research is being done to better the dielectric constants in the materials as well as having lower dielectric loss.[4]

Because the electric charge does not go through the material like it does with electrical conducting materials (hence, why they are insulators), these materials can be polarized under an electric field. When the dielectric material is between two plates, as seen in **Figure 1.2**, there is a decrease in the effective electric field which helps with minimizing any DC leakage current through a capacitor.[5]

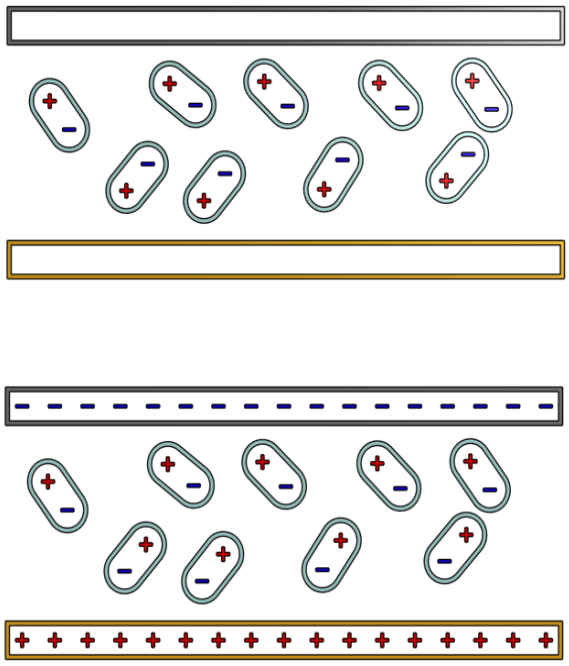

Figure 1.2. Dielectric

Piezoelectricity

The piezoelectric effect is the production of electric polarization by the application of stress to a crystal. Out of all 32 crystallographic point groups, only 20 non-centrosymmetric point groups exhibit piezoelectricity. This effect is the product of the displacement that the 'B' atoms (**Figure 1.1**) display when stress is applied to the structure; this displacement creates a dipole moment in the structure. There are two responses that the material can have, one being the direct piezoelectric response and the second being the converse piezoelectric response. The Direct response (**Figure 1.3a**) happens when a force is applied to the crystal generating a polarization proportional to the stress that produced the displacement converting the mechanical strain into energy. The converse response (**Figure 1.3b**) happens when an external electric field is applied to the material making the crystal contract or expand in response to the strength of the applied electric field allowing it to convert this potential into mechanical strain energy.[6-7] The use of piezoelectric materials range across a wide variety of applications such as sensors,[7] ultrasonic motors,[8] and power harvesting.[9]

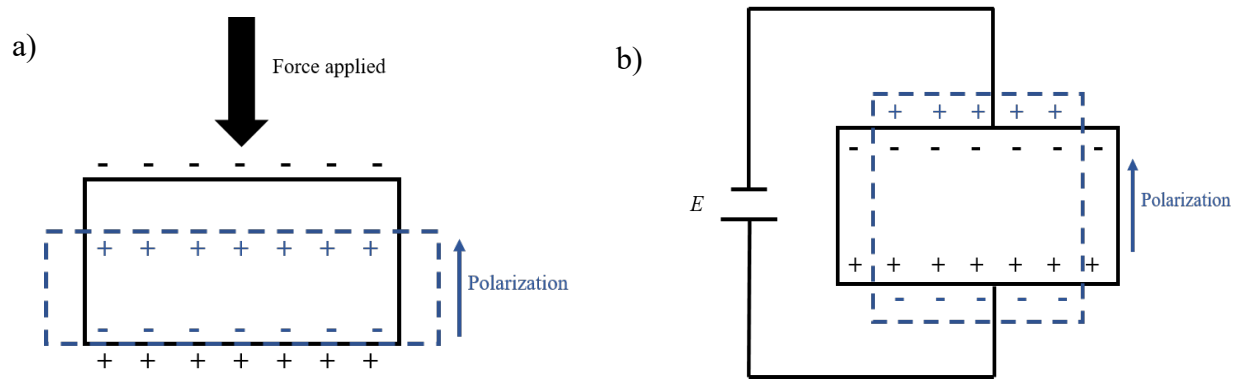

Figure 1.3. a) direct and b) converse piezoelectric response.

Pyroelectricity

The pyroelectric effect is the temperature dependence of the spontaneous polarization in certain materials, meaning that they can generate a temporary voltage when they are heated or cooled. Out of the 20 non-centrosymmetric point groups that exhibit piezoelectricity, 10 of them exhibit pyroelectricity. These materials possess a permanent electric polarization that does not manifest itself, due to the free charge carriers found on the surface of the material (**Figure 1.4a**). However, when the material is heated, the free charge carriers on the surface decrease and the redistribution of free charges to compensate for the change results in a current flow (**Figure 1.4b**).[10]

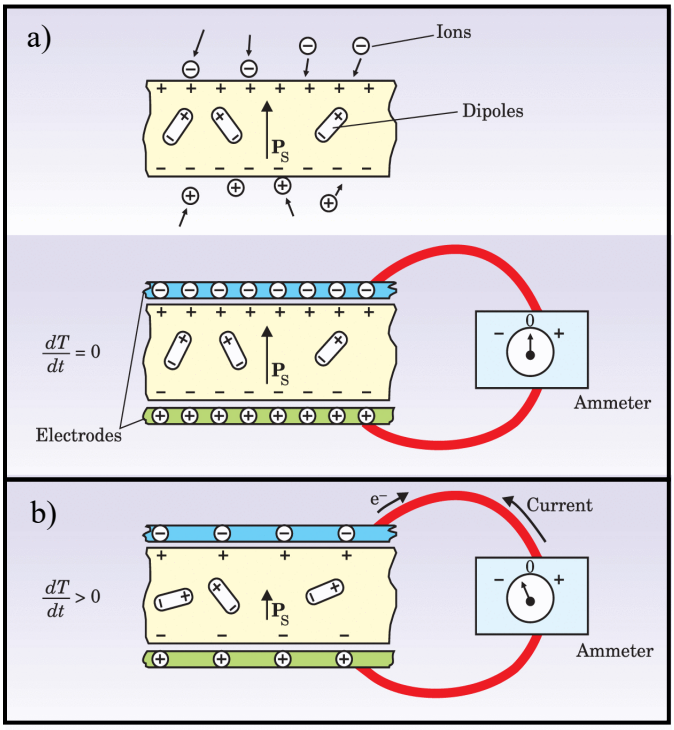

Figure 1.4. Pyroelectric response from ref [1]

It is also important to mention that pyroelectric materials have two effects (or responses). The primary pyroelectric response (the redistribution of free charges) can only be accurately measured when the material is held fixed in place, not allowing the material to expand or contract. Since, pyroelectric materials are inherently piezoelectric too, the secondary effect is caused by the expansion of the crystals when an electric field is applied.[11]

Ferroelectricity

Ferroelectricity is the ability of materials to exhibit spontaneous electric polarization. Out of the 10 non-centrosymmetric point groups that exhibit pyroelectricity, only a few of them are created with an inherent dipole moment. These materials can maintain their polarization even with no electric field and, when one is applied to a material, the polarization becomes a linear response to the strength of the electric field. Comparable to piezoelectricity, the effect on these materials can be linked to the 'B' atom, which in the case of ferroelectric materials is shifted out of plane of the oxygen atoms creating a net dipole moment in the crystal. However, unlike the previously mentioned materials, ferroelectric materials possess a transition temperature called Curie temperature. At elevated temperatures, some ABO_3 materials change from the tetragonal crystal structure to a cubic structure, which results in loss of polarization, as seen in **Figure 1.5**.

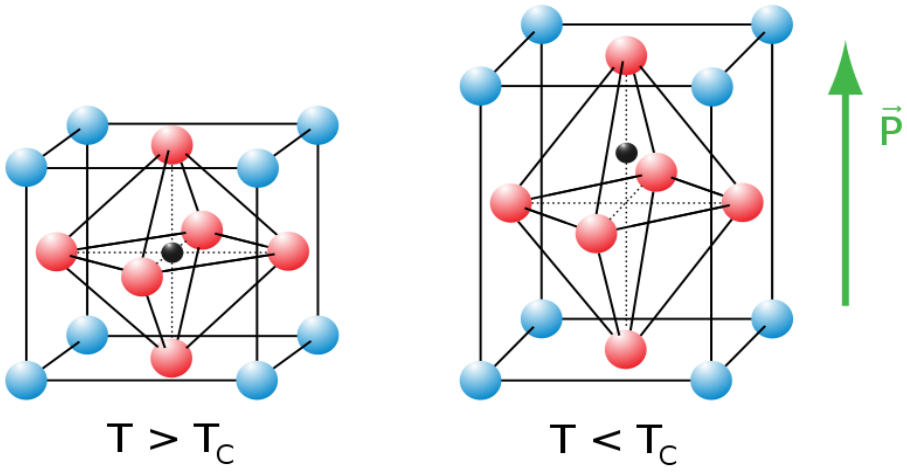

Figure 1.5. Temperature transition of a ferroelectric ABO_3 material. Left: not polarized. Right: polarized structure.

Given these unique properties, ferroelectric materials are highly sought after, with applications ranging from non-volatile memories,[12-14] transducers in sensors and actuators,[15-17] and energy harvesting.[18-20] This wide range in applications can be correlated with the extremely tunable nature of the materials. The internal dipole moment of ferroelectric materials can range in strength when the lattice is modified i.e. changing the "A" atoms on the structure is a straight forward way to change the strength of the dipole moments (e.g. $PbTiO_3$ exhibits a stronger ferroelectric response than $BaTiO_3$).

For these reasons, the focus of my research is perovskite materials that exhibit piezoelectricity and ferroelectricity known as titanate perovskites. More specifically, we are focusing on $PbTiO_3$, $BaTiO_3$, and $SrTiO_3$. These are materials with the formula $ATiO_3$ which are also referred to in literature as the inorganic perovskite oxides.

$PbTiO_3$ - Lead titanate

Lead titanate is considered one of the most important perovskite materials. This material possesses a high curie temperature (490 °C),[21] high pyroelectric coefficient, low dielectric constant (ε_r ~100), and high spontaneous polarization (75 μC/cm^2).[22] Because of these properties, it is one of the most used materials for non-volatile memories,[23] capacitors,[24] thermistors,[25] and infrared detector applications.[26]

$PbTiO_3$ has a strongly tetragonal room temperature structure (*c/a* ratio = 1.06) among the inorganic perovskite materials, giving it an inherent dipole moment and a large piezoelectric response. **Figure 1.6.** shows the tetragonal crystal structure of $PbTiO_3$. You can see the center atom (Ti in blue) is significantly displaced out of the center of the octahedron.

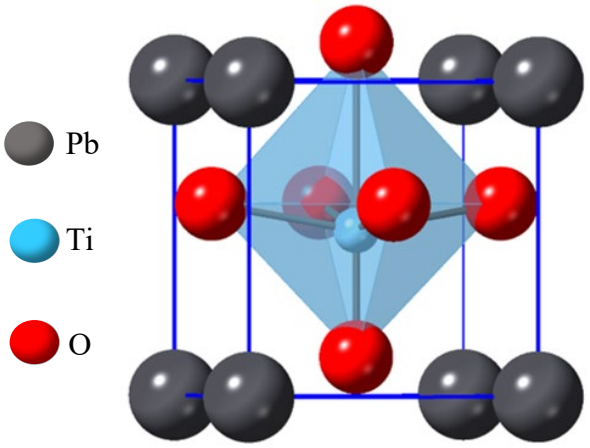

Figure 1.6. $PbTiO_3$ crystal structure

All these properties of $PbTiO_3$ make it a very important material to study. There have been many methods to synthesize lead titanate reported in the literature, but most of them focus on preparing the bulk material. This project focuses on bringing this material into the nanoregime to study the impact of this scaling on the material's properties.

$BaTiO_3$ - Barium titanate

Barium titanate is another very important member of the inorganic perovskite family. This material has been extensively studied as a less toxic counterpart to $PbTiO_3$. This material also possesses a lower transition temperature (130 °C)[21], a spontaneous polarization of 26 μC/cm^2,[2] and a dielectric constant of 5000.[27] Because of these properties, it has been used for applications such as ceramic capacitors,[28] electro optical devices,[29] and as semiconductors.[30]

Barium titanate has a lower tetragonality than $PbTiO_3$, with a *c/a* ratio of 1.011. Even with this value being comparatively small, barium titanate still exhibits strong ferroelectricity because there is enough displacement for the dipole moment to exists. **Figure 1.7**. shows the crystal structure of barium titanate, with the titania atom (in blue) still displaced from the center of the octahedron.

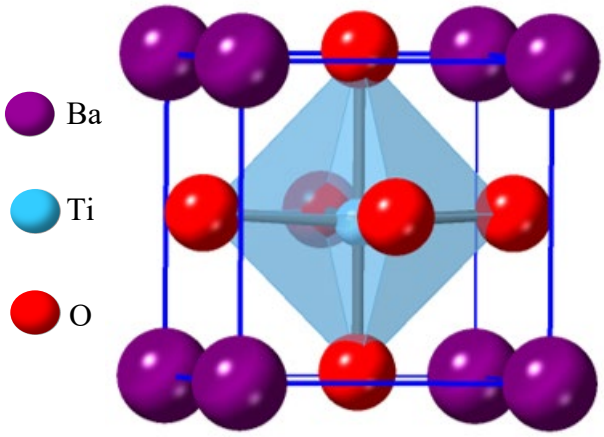

Figure 1.7. $BaTiO_3$ crystal structure

Because of these properties, and the fact that barium titanate is considered better for the environment (lower toxicity), it is also of importance to study the synthesis and properties when bringing this material into the nanoregime. This is another topic that my research covers.

$SrTiO_3$ - Strontium titanate

Strontium titanate is the third and last member of the inorganic perovskite family that I will be focusing on. This material is of great interest as a low-temperature ferroelectric material. This is because the transition temperature for this perovskite is -163 °C (110 K),[31] making it one of the few titanium perovskites that has a cubic structure at room temperature. However, this material is an insulator at room temperature, making it extremely useful as a dielectric material. It also has a band gap of 3.15eV making it possible for this material to be used as a photocatalytic material.

Strontium titanate, like the other inorganic perovskite material, has the formula ABO_3 shown in **Figure 1.8.** In this case, the titanium atom (in blue) is in the center of the octahedron at room temperature, since the structure in the case of strontium titanate is cubic (c/a = 1) giving a small piezoelectric response. However, the low transition temperature of this material makes it a great piezoelectric material for low temperature applications.

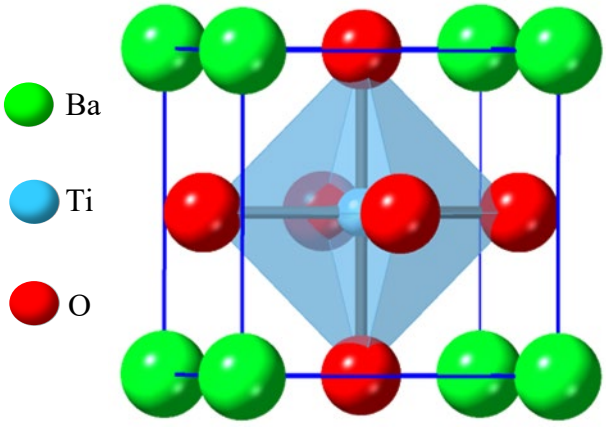

Figure 1.8. $SrTiO_3$ crystal structure

Since this material exhibits such a low temperature piezoelectric response, it has been widely studied for its low-temperature quantum paraelectric ground state.[32] Because of this, my research project also expanded to study the synthesis of $SrTiO_3$ nanosheets.

Nanomaterials

Nanoscience deals with the study (synthesis, characterization, and discovery) of nanostructured materials. These materials are characterized by possessing at least one dimension in the nanometer (1 nm= 10^{-9} m) range.[33] The synthesis of these nanomaterials helps us understand the gap between single atoms and bulk systems. Nanomaterials have shown changes in their chemical and physical properties compared to their bulk counter parts; the study of these property changes, as well as the new applications that can be achieved with these materials, is the basis of nanoscience. Several morphologies have been found for nanomaterials (nanoparticles, nanotubes, quantum dots, etc.) but, out of all those materials, nanosheets have shown remarkable physical and chemical stability. This paired with high tensile strength and specific surface area makes this class of nanomaterials the interest of my research.

Freestanding nanosheets are highly sought after because of their surface-related properties, such as high electron mobility and good thermal conduction. The targeted applications for these materials require an increasing degree of morphology control needing a uniform distribution in thickness, and, thus, it is necessary to find a synthetic route that would yield a uniform distribution of nanosheets with thickness < 10 nm.

As previously stated, inorganic perovskite materials are of great interest in the scientific community due to all the amazing properties they possess, ranging from piezoelectricity to ferroelectricity. Bringing these materials into the nanoregime will enable the fabrication of smaller and faster electronic devices.

Lead titanate and barium titanate nanomaterials have been prepared as nanorods,[34-36] nanoparticles,[37-39]and other forms of nanomorphology[40-41] (not nanosheets). However, the synthesis of nanosheets in this class of materials has not been extensively studied. Nanosheets thicker than 10 nm have been synthesized previously for $PbTiO_3$.[42]One problem with this synthesis, and the other ones that try to do this, is that they require mineralizers and capping agents to isolate the desired morphology. This is a problem because it introduces another reagent that needs to be washed out or, in the case of this specific paper, they had Na^+ ions binding to the nanosheets that they could not get rid of. Because of this feature, the properties of the sheets (ferroelectricity) could be impacted.

The change in the properties of the materials is a real concern even when no mineralizers are used. Literature has shown that bringing materials down to the nanoregime can affect their properties. This is specifically correct in the case of piezoelectric, pyroelectric, and ferroelectric materials because a different degree of ordering is expected on the surfaces making these properties size dependent. Several studies have shown this size dependence on the perovskite family of materials.[43-45]

Another problem that the materials encounter when being sized down into the nanoregime is the loss of tetragonality for $PbTiO_3$ and $BaTiO_3$.[46-47] This has been studied in the literature and the most common solution is annealing; however, this typically causes aggregation and loss of the nanomorphology, or the materials start to break from the heating needed to induce the transition from cubic to tetragonal.[39, 48-49] Because of these reasons, we decided to use a templated growth approach via a hydrothermal synthesis method for the $PbTiO_3$ system and a templated flux-based route for the $BaTiO_3$ and $SrTiO_3$ systems.

Templated growth

For the synthesis of these inorganic perovskites, we decided to utilize a templated growth approach. We employed a nanosheet precursor in order to help guide our material to grow with the same morphology. This synthetic approach has been used effectively in literature to synthesize nanomaterials of different morphologies and sizes.[50] We also utilized the bottom-up approach to synthesize nanomaterials as shown in **Figure 1.9.** This requires the materials to grow from atoms or other building blocks, unlike the top-down approach (**Figure 1.9**) which requires the starting material to be a 'bulk' size to break down into nanosized materials. For these reasons, we are utilizing nanosheets of TiO_2 (bronze polymorph).

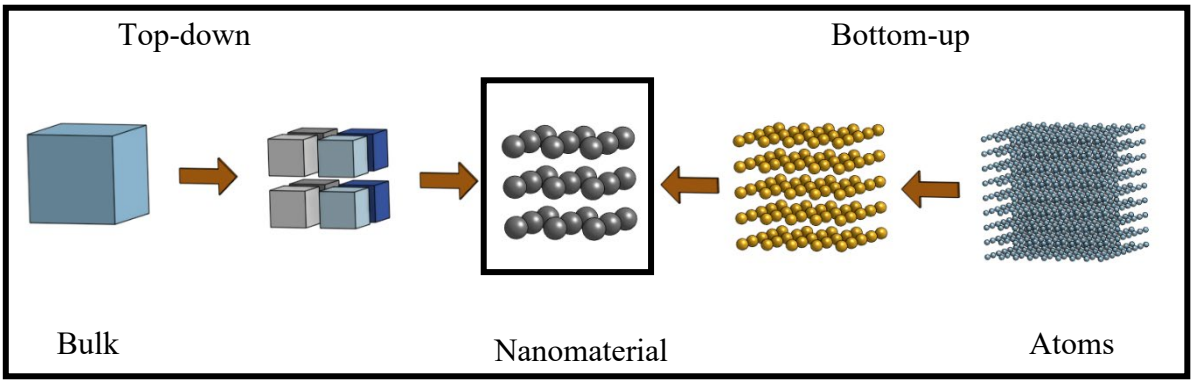

Figure 1.9. Top-down and bottom-up approach

These nanosheets have already been synthesized by Sasaki and coworkers.[51] They start with the anatase polymorph of TiO_2 and use a MoO_3 flux in order to grow crystals of the layered $TiO_2(B)$. These crystals have a formula of $K_{0.8}Ti_{1.73}Li_{0.27}O_4$ and are easily exfoliated by osmotic swelling with the help of the organic base tetrabutylammonium hydroxide, TBA(OH). The synthesis of these nanosheets is detailed in Chapter II.

Hydrothermal synthesis

The reactions in the $PbTiO_3$ system use hydrothermal methods. This synthesis approach has been widely used for the growth of nanomaterials.[52-53] The method works by sealing the aqueous solution of precursors in a Teflon-lined stainless steel autoclave, which is heated to temperatures > 100 °C. The autoclave prevents the water from evaporating, creating a high temperature, high pressure environment, which helps materials dissolve. The dissolution of the materials is extremely crucial for this synthetic approach because it is required for the precursors to interact. However, only one of the materials must be soluble in water. In our case, we will use water soluble lead salts (e.g., PbO, $PbCl_2$) as our dissolvable precursor.

Flux reactions

The syntheses of $BaTiO_3$ and $SrTiO_3$ are accomplished by flux-based methods, which also has proven useful for preparing nanomaterials.[54-55] For these systems we decided to stay away from hydrothermal reactions because the formation of $PbTiO_3$ resulted in problematic side products. We still will be utilizing the templated growth method with the same nanosheet precursor, $TiO_2(B)$. However, for this synthesis, Ba and Sr salts will be used as fluxes to keep the reaction as clean as possible and facilitate the isolate of $BaTiO_3$ and $SrTiO_3$ nanosheets.

Research goals

The goal of my research has been to synthesize nanosheets of $PbTiO_3$, $BaTiO_3$, and $SrTiO_3$ by using a bottom-up templated growth approach. For $PbTiO_3$ we will be using a hydrothermal approach and for $BaTiO_3$ and $SrTiO_3$ we will be using a flux-based method. For all three systems, nanosheets of $TiO_2(B)$ will be used as the templating agent. In order for us to consider the material to be a nanosheet, they have to be less than 10 nm in thickness, a measurement that we will get by using atomic force microscopy. Another big part of this project is to try synthesizing nanosheets of perovskite materials that are in the tetragonal crystal structure. Studies must be performed in order to fully characterize the nanosheets and the structures they adopt.

In Chapter II, I detail several pathways to synthesize nanosheets of $PbTiO_3$ that have been proven successful. PbO proved to be the best lead precursor for these reactions, and the nanosheets of $(TBA)_{1.07}Ti_{1.73}O_4$ had to be treated with $Pb(NO_3)_2$ in order to create a Pb_x-TiO_2 flocculate that is sufficiently reactive. However, the basic lead carbonate plumbonacrite side product proved to easily form and be hard to remove. After several attempts to prevent the formation of plumbonacrite, three different routes to synthesize the material yielded nanosheets of $PbTiO_3$ and no basic lead carbonate: the first being a synthesis between the Pb_x-TiO_2 nanosheets and PbO at

low pH (~6.88), the second being N_2 atmosphere reactions, and the third was the optimization of the ratio between Pb_x-TiO_2 and PbO (1:1.67). These nanosheets were proven to be tetragonal $PbTiO_3$ by PXRD, STEM, EDS, and HRTEM. More studies on the stability of our $PbTiO_3$ nanosheets must be performed.

In Chapter IV, I detail the synthesis of the $BaTiO_3$ nanosheets, as well as the attempts to reproduce a previous synthesis made in our lab. The previous synthesis proved to be unreproducible, forcing us to change routes. The same $(TBA)_{1.07}Ti_{1.73}O_4$ nanosheets were used in a new protocol and, like with the $PbTiO_3$ system, the TBA needed to be exchanged for another cation in order to make the nanosheets reactive; H_x-TiO_2 nanosheets were prepared for this purpose. The flux synthesis proved to work with the hydrated hydroxide salt of barium, if the water of hydration was maintained in the system. We achieved this by utilizing a sealed Schlenk tube vessel for the reactions. At the end, we were able to synthesize nanosheets of $BaTiO_3$.

In Chapter V, I detail the progress made to synthesize $SrTiO_3$. The same solid-state process was used from the $BaTiO_3$ system with the same nanosheet precursor of H_x-TiO_2. However, this synthesis requires more work in order to increase the amount of strontium incorporating into the structure. More studies on the strontium salt used as a precursor are also needed.

In Chapter VI, I detail the synthesis and characterization of plumbonacrite, a little-studied material. With isolated plumbonacrite nanoplatelets, I was able to study the effects of the electron microscope's electron beam on this material.

Overall, inorganic perovskite materials are extremely important because of their amazing electronic properties. The synthesis of this material into the nanoregime is very important for applications that require smaller devices such as non-volatile memories. The biggest drawback found in these materials is the challenge of maintaining tetragonality in the $PbTiO_3$ and $BaTiO_3$ systems. However, our nanosheets have proven to exist in the tetragonal crystal structure at room temperature. In future work, the stability of the nanosheets, as well as the full characterization of the $SrTiO_3$ nanosheets and the full study of the properties of all the nanosheets in the system ($PbTiO_3$ and $BaTiO_3$) have to be performed.

References

1. Marino, A. A., *Modern bioelectricity*. CRC Press: 1988.

2. Jaffe, B., *Piezoelectric ceramics*. Elsevier: 2012; Vol. 3.

3. Bhalla, A.; Guo, R.; Roy, R., The perovskite structure—a review of its role in ceramic science and technology. *Materials Research Innovations* **2000,** *4* (1), 3-26.

4. Sebastian, M. T.; Jantunen, H., Low loss dielectric materials for LTCC applications: a review. *International Materials Reviews* **2008,** *53* (2), 57-90.

5. Lee, B. H.; Kang, L.; Qi, W.-J.; Nieh, R.; Jeon, Y.; Onishi, K.; Lee, J. C. In *Ultrathin hafnium oxide with low leakage and excellent reliability for alternative gate dielectric application*, International Electron Devices Meeting 1999. Technical Digest (Cat. No. 99CH36318), IEEE: 1999; pp 133-136.

6. Damjanovic, D., Ferroelectric, dielectric and piezoelectric properties of ferroelectric thin films and ceramics. *Reports on Progress in Physics* **1998,** *61* (9), 1267.

7. Gautschi, G., Piezoelectric sensors. In *Piezoelectric Sensorics*, Springer: 2002; pp 73-91.

8. Ahmad, A. S.; Usman, M. M.; Abubakar, S. B.; Gidado, A. Y., Review on the application of Piezoelectric materials in the development of ultrasonic motors. Kano University of Science and Technology: 2017.

9. Anton, S. R.; Sodano, H. A., A review of power harvesting using piezoelectric materials (2003–2006). *Smart materials and Structures* **2007,** *16* (3), R1.

10. Lang, S. B., Pyroelectricity: from ancient curiosity to modern imaging tool. *Physics today* **2005,** *58* (8), 31.

11. Zook, J.; Liu, S., Pyroelectric effects in thin film. *Journal of Applied Physics* **1978,** *49* (8), 4604-4606.

12. Ducharme, S.; Reece, T. J.; Othon, C. M.; Rannow, R. K., Ferroelectric polymer Langmuir-Blodgett films for nonvolatile memory applications. *IEEE Transactions on Device and Materials Reliability* **2005,** *5* (4), 720-735.

13. Naber, R. C.; Asadi, K.; Blom, P. W.; de Leeuw, D. M.; de Boer, B., Organic nonvolatile memory devices based on ferroelectricity. *Advanced materials* **2010,** *22* (9), 933-945.

14. Miller, S.; McWhorter, P., Physics of the ferroelectric nonvolatile memory field effect transistor. *Journal of applied physics* **1992,** *72* (12), 5999-6010.

15. Muralt, P., Ferroelectric thin films for micro-sensors and actuators: a review. *Journal of micromechanics and microengineering* **2000,** *10* (2), 136.

16. Mahdi, R. I.; Gan, W.; Majid, W., Hot plate annealing at a low temperature of a thin ferroelectric P (VDF-TrFE) film with an improved crystalline structure for sensors and actuators. *Sensors* **2014,** *14* (10), 19115-19127.

17. Zirkl, M.; Sawatdee, A.; Helbig, U.; Krause, M.; Scheipl, G.; Kraker, E.; Ersman, P. A.; Nilsson, D.; Platt, D.; Bodö, P., An all-printed ferroelectric active matrix sensor network based on only five functional materials forming a touchless control interface. *Advanced Materials* **2011,** *23* (18), 2069-2074.

18. Bowen, C.; Kim, H.; Weaver, P.; Dunn, S., Piezoelectric and ferroelectric materials and structures for energy harvesting applications. *Energy & Environmental Science* **2014,** *7* (1), 25-44.

19. Roscow, J.; Zhang, Y.; Taylor, J.; Bowen, C., Porous ferroelectrics for energy harvesting applications. *The European Physical Journal Special Topics* **2015,** *224* (14-15), 2949-2966.

20. Morozovska, A.; Eliseev, E.; Svechnikov, G.; Kalinin, S. V., Pyroelectric response of ferroelectric nanowires: Size effect and electric energy harvesting. *Journal of Applied Physics* **2010,** *108* (4), 042009.

21. Piskunov, S.; Heifets, E.; Eglitis, R.; Borstel, G., Bulk properties and electronic structure of SrTiO3, BaTiO3, PbTiO3 perovskites: an ab initio HF/DFT study. *Computational Materials Science* **2004,** *29* (2), 165-178.

22. Iijima, K.; Tomita, Y.; Takayama, R.; Ueda, I., Preparation of c-axis oriented PbTiO3 thin films and their crystallographic, dielectric, and pyroelectric properties. *Journal of applied physics* **1986,** *60* (1), 361-367.

23. Chen, W.; Zheng, Y.; Xiong, W.; Feng, X.; Wang, B.; Wang, Y., Effect of mechanical loads on stability of nanodomains in ferroelectric ultrathin films: Towards flexible erasing of the non-volatile memories. *Scientific reports* **2014,** *4*, 5339.

24. Umeno, Y.; Albina, J. M.; Meyer, B.; Elsässer, C., Ab initio calculations of ferroelectric instability in PbTiO 3 capacitors with symmetric and asymmetric electrode layers. *Physical Review B* **2009,** *80* (20), 205122.

25. Chaudhari, V. A.; Bichile, G. K., Synthesis, structural, and electrical properties of pure PbTiO3 ferroelectric ceramics. *Smart Materials Research* **2013,** *2013*.

26. Okuyama, M.; Matsui, Y.; Nakano, H.; Hamakawa, Y., PbTiO3 ferroelectric thin film gate fet for infrared detection. *Ferroelectrics* **1981,** *33* (1), 235-241.

27. Luan, W.; Gao, L.; Guo, J., Size effect on dielectric properties of fine-grained BaTiO3 ceramics. *Ceramics international* **1999,** *25* (8), 727-729.

28. MacChesney, J.; Gallagher, P.; DiMarcello, F., Stabilized barium titanate ceramics for capacitor dielectrics. *Journal of the American Ceramic Society* **1963,** *46* (5), 197-202.

29. Abel, S.; Stöferle, T.; Marchiori, C.; Caimi, D.; Czornomaz, L.; Stuckelberger, M.; Sousa, M.; Offrein, B. J.; Fompeyrine, J., A hybrid barium titanate–silicon photonics platform for ultraefficient electro-optic tuning. *Journal of Lightwave Technology* **2016,** *34* (8), 1688-1693.

30. Heywang, W., Semiconducting barium titanate. *Journal of Materials Science* **1971,** *6* (9), 1214-1224.

31. Saifi, M. A.; Cross, L., Dielectric properties of strontium titanate at low temperature. *Physical Review B* **1970,** *2* (3), 677.

32. Müller, K. A.; Burkard, H., SrTi O 3: An intrinsic quantum paraelectric below 4 K. *Physical Review B* **1979,** *19* (7), 3593.

33. Gogotsi, Y., *Nanomaterials handbook*. CRC press: 2017.

34. Zhao, L.; Steinhart, M.; Yu, J.; Gösele, U., Lead titanate nano-and microtubes. *Journal of materials research* **2006,** *21* (3), 685-690.

35. Shi, Liang, Yeming Xu, and Quan Li. "Controlled growth of lead oxide nanosheets, scrolled nanotubes, and nanorods." *Crystal Growth and Design* 8.10 (2008): 3521-3525

36. Kolen'ko, Y. V.; Kovnir, K. A.; Gavrilov, A. I.; Garshev, A. V.; Frantti, J.; Lebedev, O. I.; Churagulov, B. R.; Van Tendeloo, G.; Yoshimura, M., Hydrothermal synthesis and characterization of nanorods of various titanates and titanium dioxide. *The Journal of Physical Chemistry B* **2006,** *110* (9), 4030-4038.

37. Sagadevan, S.; Das, I.; Podder, J., Synthesis of lead titanate nanoparticles via sol–gel technique and its characterization. *Journal of Materials Science: Materials in Electronics* **2016,** *27* (12), 13016-13021.

38. Peng, Z.; Chen, Y., Preparation of BaTiO3 nanoparticles in aqueous solutions. *Microelectronic engineering* **2003,** *66* (1-4), 102-106.

39. Wang, J.; Pang, X.; Akinc, M.; Lin, Z., Synthesis and characterization of perovskite PbTiO 3 nanoparticles with solution processability. *Journal of Materials Chemistry* **2010,** *20* (28), 5945-5949.

40. Comyn, T. P.; Kanguwe, D. F.; He, J.; Brown, A. P., Synthesis of bismuth ferrite lead titanate nano-powders and ceramics using chemical co-precipitation. *Journal of the European Ceramic Society* **2008,** *28* (11), 2233-2238.

41. Nafari, A.; Bowland, C. C.; Sodano, H. A., Ultra-long vertically aligned lead titanate nanowire arrays for energy harvesting in extreme environments. *Nano Energy* **2017,** *31*, 168-173.

42. Xu, G.; Huang, X.; Krstic, V.; Chen, S.; Yang, X.; Chao, C.; Shen, G.; Han, G., Hydrothermal synthesis of single-crystalline tetragonal perovskite PbTiO 3 nanosheets with dominant (001) or (111) facets. *CrystEngComm* **2014,** *16* (21), 4373-4376.

43. Ahn, C.; Rabe, K.; Triscone, J.-M., Ferroelectricity at the nanoscale: local polarization in oxide thin films and heterostructures. *Science* **2004,** *303* (5657), 488-491.

44. Shaw, T.; Trolier-McKinstry, S.; McIntyre, P., The properties of ferroelectric films at small dimensions. *Annual Review of Materials Science* **2000,** *30* (1), 263-298.

45. Fong, D. D.; Stephenson, G. B.; Streiffer, S. K.; Eastman, J. A.; Auciello, O.; Fuoss, P. H.; Thompson, C., Ferroelectricity in ultrathin perovskite films. *Science* **2004,** *304* (5677), 1650-1653.

46. Nalwa, H. S., *Handbook of low and high dielectric constant materials and their applications, two-volume set*. Elsevier: 1999.

47. Zhao, Z.; Buscaglia, V.; Viviani, M.; Buscaglia, M. T.; Mitoseriu, L.; Testino, A.; Nygren, M.; Johnsson, M.; Nanni, P., Grain-size effects on the ferroelectric behavior of dense nanocrystalline BaTiO 3 ceramics. *Physical Review B* **2004,** *70* (2), 024107.

48. Tsumura, T.; Matsuoka, K.; Toyoda, M., Formation and annealing of BaTiO3 and SrTiO3 nanoparticles in KOH solution. *Journal of Materials Science & Technology* **2010,** *26* (1), 33-38.

49. Manh, D. H.; Thanh, T. D.; Phuc, N. X.; Hong, L. V.; Phong, P.; Hung, L., Perovskite nanoparticles synthesised by reactive milling combined with thermal processing: preparation, morphology and structure characterisation. *International journal of nanotechnology* **2011,** *8* (3-5), 241-254.

50. Liu, Y.; Goebl, J.; Yin, Y., Templated synthesis of nanostructured materials. *Chemical Society Reviews* **2013,** *42* (7), 2610-2653.

51. Tanaka, T.; Ebina, Y.; Takada, K.; Kurashima, K.; Sasaki, T., Oversized titania nanosheet crystallites derived from flux-grown layered titanate single crystals. *Chemistry of materials* **2003,** *15* (18), 3564-3568.

52. Feng, S.; Xu, R., New materials in hydrothermal synthesis. *Accounts of chemical research* **2001,** *34* (3), 239-247.

53. Mao, Y.; Banerjee, S.; Wong, S. S., Hydrothermal synthesis of perovskite nanotubes. *Chemical communications* **2003,** (3), 408-409.

54. Cho, W.-S., Structural evolution and characterization of BaTiO3 nanoparticles synthesized from polymeric precursor. *Journal of Physics and Chemistry of Solids* **1998,** *59* (5), 659-666.

55. Manzoor, U.; Kim, D. K., Synthesis of nano-sized barium titanate powder by solid-state reaction between barium carbonate and titania. *Journal of Materials Science and Technology* **2007,** *23* (5), 655-658.

CHAPTER II
SYNTHESIS OF LEAD TITANATE NANOSHEETS FROM A LAYERED TITANATE PRECURSOR

Introduction

Lead titanate ($PbTiO_3$) is a classic piezoelectric and ferroelectric material with strong polarization and a high Curie temperature compared to other perovskite oxides. The nano structuring of $PbTiO_3$ is directly related to applications ranging from capacitors to non-volatile random-access memory. Here we describe freestanding nanosheets of tetragonal $PbTiO_3$ synthesized by a templated hydrothermal approach. The template is $(TBA)_{1.07}Ti_{1.73}O_4$, a well-known 2D-nanostructured analog of TiO_2(B), which is converted to a more reactive lead-substituted form, Pb_x-TiO_2, prior to hydrothermal reactions with PbO. Tetragonal $PbTiO_3$ nanosheets were obtained through different reactions with varying atmosphere and pH. This chapter discusses the formation of the $PbTiO_3$ nanosheet product, the optimized conditions for the formation of $PbTiO_3$ nanosheets, and their characterization.

Lead titanate is considered one of the most important perovskite materials. This material possesses a high curie temperature (490 °C)[1], high pyroelectric coefficient, low dielectric constant (ε_r ~100), and high spontaneous polarization (75 $\mu C/cm^2$).[2] Because of these properties, it is one of the most used materials for non-volatile memories,[3] capacitors,[4] thermistors,[5] and infrared detector applications.[6]

In this chapter we will discuss the synthesis of $PbTiO_3$ nanosheets via a templated growth method by utilizing a nanosheet precursor [$(TBA)_{1.07}Ti_{1.73}O_4$]. We will be synthesizing the nanosheets via a hydrothermal approach by utilizing α-PbO as the source of lead. When preliminary reactions were carried, it was observed that the nanosheets capped with the TBA^+ ion were unreactive to lead sources under hydrothermal conditions ≤ 250 °C. This led to the exchange of TBA^+ with other cations, the results of this experiments will be fully examined.

Reactions were conducted under standard atmosphere and N_2 atmosphere environments demonstrating the formation of a basic lead carbonate (plumbonacrite) was favorable when the reaction contained excess α-PbO and dissolved CO_2(g). By controlling the amount of lead in the system, we were able to successfully synthesize nanosheets of tetragonal $PbTiO_3$. Likewise, when the pH of the solution was controlled to prevent the formation of the basic lead carbonate, the reactions yielded nanosheets of tetragonal $PbTiO_3$. All these results are discussed in detail throughout the chapter.

Experimental section

Materials:

$Pb(NO_3)_2$ (Sigma-Aldrich Corp., 99%), α-PbO (Sigma-Aldrich Corp., 99%), Li_2CO_3 (Sigma-Aldrich Corp.), MoO_3 (Sigma-Aldrich Corp., 99.5%), K_2CO_3 (Sigma-Aldrich Corp.), Anatase (Sigma-Aldrich Corp., 99.8%), TBAOH (Sigma-Aldrich Corp., 1M HPLC), HCl (Sigma-Aldrich Corp., 37% w/v).

Preparation of $(TBA)_{1.07}Ti_{1.73}O_4$:

5.000 g (62.6 mmol) of TiO_2 anatase is ground together with 8.3522 g (60.4 mmol) of K_2CO_3, 0.347 6 g (4.70 mmol) of Li_2CO_3, and 6.6152g (45.9 mmol) of MoO_3 in a mortar and pestle for 15 minutes. The powder is placed into a Pt crucible and ramped up to 1200 °C at 10 °C/min and held there for 10 h. It is cooled slowly at 4 °C/h down to 900 °C and then it is cool down to room temperature. The large $K_{0.8}Ti_{1.73}Li_{0.27}O_4$ crystals are separated from the K_2MoO_4 flux using excess hot water. The $K_{0.8}Ti_{1.73}Li_{0.27}O_4$ crystals are shaken in 500 mL of 1M HCl for 5 days in a linear shaker at 78 RPM. A fresh 500 mL of 1M HCl is added each day by decanting the acid after centrifuging for 30 min at 10,000 RPM. After the fifth day the crystals are fully protonated ($H_{1.07}Ti_{1.73}O_4$) and the acid is exchanged for 500 mL of 0.5 M tetrabutylammonium hydroxide (TBAOH) solution and shaken again at 78 RPM for 7 days. Finally, the excess TBAOH solution is decanted by centrifuging at 10,000 RPM for 1 hour and the nanosheets are re-dispersed in 1L DI water.

Preparation of "Pb_x–TiO_2" precursor:

3.00 mL of $(TBA)_{1.07}Ti_{1.73}O_4$ (5.7 mg mL^{-1} dispersion in aqueous DI H_2O) were placed in a centrifuge tube. Upon addition of a suspension of 0.10 g $Pb(NO_3)_2$ in 1 mL H_2O, a white flocculate formed. This material was isolated by centrifuging for 15 min at 10,000 rpm and then washing with 35 mL H_2O 2× to remove excess Pb^{2+} and TBA^+. The flocculate was used as-is ("wet") in some cases, or it was dried by lyophilization to give 0.0157 g of white powder with a yield of 92.4% (with product composition of $PbTi_{3.46}O_2$). Note: an off-white or yellow-colored product indicates the presence of impurities (chloride cations).

Standard hydrothermal reactions:

0.0171 g of wet (washed but not dried) Pb_x–TiO_2 flocculate was re-suspended in 25 mL H_2O. 0.11947 g PbO (0.53 mmol) was added and vortex mixed (VWR Mini Vortex Mixer 14005-824) for 1 min at 3000 rpm. 1 M HCl(aq) was added for low pH reactions and adjusted as necessary after mixing. The resulting mixture was transferred to a 42 mL Teflon sleeve, placed in a stainless-steel acid digestion vessel, sealed, and placed in a 120 °C gravity convection oven. Products were isolated by freeze drying the solution.

Air-free hydrothermal reactions:

These reactions were set up in a glovebox containing a water-saturated N_2(g) atmosphere ("wetbox"). In the wetbox, 0.0800 g PbO (0.535 mmol) and ~0.0171g freeze-dried Pb_x–TiO_2 (0.214 mmol) were suspended in 25 mL degassed DI H_2O. This mixture was transferred to a 42 mL Teflon sleeve, placed in a stainless-steel acid digestion vessel, sealed, removed from the wetbox, and placed in a 120 °C gravity convection oven for 4 d. Then the reaction vessel was taken back into the wetbox and opened. With all sample handling still occurring within the wetbox, the

product mixture was bath sonicated for 1 h and centrifuged at 3250 rpm for 1 h. Once most of the water was decanted, the material was taken out of the wetbox in the centrifuge tube and dried in a vacuum oven at 635 torr at room temperature (22 °C).

Synthesis of $PbTiO_3$ nanosheets:

0.0157 g of wet Pb_x–TiO_2 was resuspended in 25 mL H_2O. 0.0800 g of PbO (0.358 mmol) was added and vortex mixed (VWR Mini Vortex Mixer 14005-824) for 1 min at 3000 rpm. The dispersion was transferred to a 42 mL Teflon sleeve, placed in a stainless-steel acid digestion vessel, sealed, and heated to 120 °C for 5 d. Then the reaction mixture was transferred to a 50 mL centrifuge tube and probe sonicated (Misonix S-4000) for 1 min at 10 amp. The resulting pearlescent dispersion was centrifuged for 15 min at 10,000 rpm, and the isolated solid was dried by lyophilization to provide 0.03391 g of yellow powder (57% isolated yield).

Characterization details

Powder X-ray diffraction (PXRD) data was collected on a Bruker D8 instrument utilizing a Co−Kα X-ray source (λ = 1.78890 Å) operated at 40 kV and 35 mA. Data was collected from 10 to 80° 2θ with a scan rate of 0.1 s/step. Samples were prepared as powder mounts or drop cast from solution. Pattern matching was performed using the PDF4+ database.

Transmission electron microscopy (TEM) imaging and selected area electron diffraction (SAED) analyses were performed using a FEI Tecnai 20 transmission electron microscope with an accelerating voltage of 200 kV. High resolution transmission electron microscopy (HRTEM) was performed with a FEI Tecnai G2 F30 S-TWIN operating at 300 kV. Samples were drop cast onto Formvar, holey carbon, or lacey carbon grids and air dried.

Scanning electron microscopy (SEM) and scanning transmission electron microscopy (STEM) analyses were performed using a FEI Teneo FE-SEM at 10-30 kV with a spot size of 10. Samples were drop cast onto silicon wafer or Formvar grids.

Results and Discussion:

Preparation and characterization of the "Pb_x–TiO_2" nanosheet precursor

The pathway to $PbTiO_3$ nanosheets in this work follows a bottom-up hydrothermal approach. Although this approach typically employs mineralizers to influence nanostructure formation and help dissolve precursors,[7-8] here we use hydrothermal conditions to effect the templated growth of two-dimensional $PbTiO_3$ starting from the nanosheet form of TiO_2(B) (bronze polymorph of TiO_2) first reported by Sasaki and coworkers.[9] The layered structure of TiO_2(B) enables exfoliation into monolayers with the assistance of the bulky tetrabutylammonium (TBA) cation and mechanical shear force (i.e., shaking), providing $(TBA)_{1.07}Ti_{1.73}O_4$ nanosheets. From the data presented in **Figure 2.1**, it is clear that these nanosheets are large in lateral dimensions, thin, and not aggregated. TEM (**Figure 2.1a**) shows extremely thin material containing folds, with lateral dimensions of individual nanosheets ranging from ~500 nm to ~2 μm. Atomic force microscopy (AFM) measurements (**Figure 2.1b-d**) provide a nanosheet thickness of 1.5 nm, which correlates to 2 monolayers in thickness [single monolayer of TiO_2(B) is 0.623 nm thick]. PXRD (**Figure 2.1c**) shows a pattern of peaks corresponding to a layered series, here the restacked $(TBA)_{1.07}Ti_{1.73}O_4$ nanosheets. The 2θ values (17.80°, 7.79°, and 5.83°) provide an interlayer spacing of 1.78 nm.

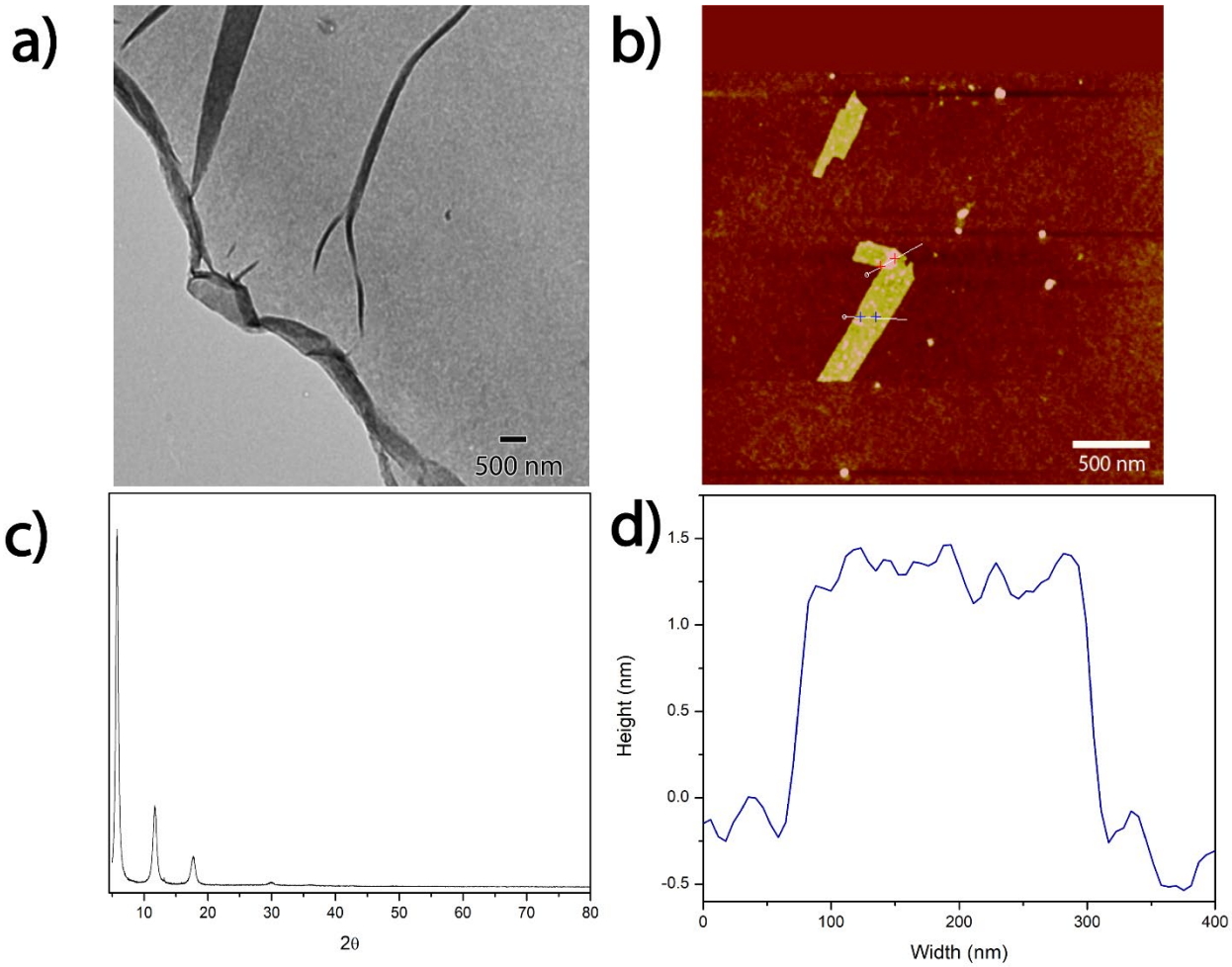

Figure 2.1. Characterization of $(TBA)_{1.07}Ti_{1.73}O_4$: a) TEM, b) AFM, c) AFM height profile, and d) PXRD pattern.

However, initial experiments showed that $(TBA)_{1.07}Ti_{1.73}O_4$ does not react with lead sources like lead oxide under hydrothermal conditions ≤ 250 °C. To enhance the reactivity of $(TBA)_{1.07}Ti_{1.73}O_4$, we exchanged TBA^+ (494 pm ionic radius)[10] for smaller cations like H^+, yielding "H_x–TiO_2", and Pb^{2+} (119 pm radius), yielding "Pb_x–TiO_2". Once the TBA^+ was exchanged, the change in cation size and charge caused the nanosheets to crumple and aggregate, creating a flocculate.

Nanosheet flocculation has been reported in the literature. Ozawa et al. showed how nanosheets are essentially gigantic polyatomic ions, and when the material is a metal oxide, they are most likely negatively .[11] Because $(TBA)_{1.07}Ti_{1.73}O_4$ nanosheets are prepared in suspension form, once the solution is changed with a counterionic species, they spontaneously restack due to the electrostatic interactions between them.[11] Additionally, $(TBA)_{1.07}Ti_{1.73}O_4$ nanosheets are extremely thin and flexible, resulting in crumpling rather than stacking behavior. Such crumpling has been observed for materials that have similar thickness and lateral dimensions, such as the nanosheets of MnO_2 previously synthesized by Pal et al.[12] The inter- and intra-aggregation of nanosheets also has been used in other studies, including the layer-by-layer assembly of nanosheets,[13-14] the preparation of intercalated layered hydroxides,[15-16] and for the conversion of nanosheets into nanotubes.[17-18]

Characterization of "Pb_x–TiO_2" is summarized in **Figures 2.2 –4**. Panel 2a shows s STEM image of Pb_x–TiO_2 that was resuspended in water and drop cast onto a formvar grid. In this image, we can observe the crumpling of the nanosheets, while at the same time, we can see that the general nanosheet morphology is maintained. Energy dispersive spectroscopy (EDX) mapping shows good overlap of Pb, O and Ti. Moreover, in **Figure 2.2d** we see that the averaged EDX spectrum over this area contains no N signal, usually observed as a peak at 0.392 eV, further confirming the

loss of TBA^+. These EDX data provide a Pb:Ti ratio of 0.22:1 for Pb_x–TiO_2 nanosheets, confirming that the TBA^+ was exchanged with Pb^{2+}. **Figure 2.2b** shows PXRD data (material was pressed into a palette) for Pb_x–TiO_2, which is consistent with a non-crystalline material. The amorphous nature of Pb_x–TiO_2 was observed by SAED as well (**Figure 2.2c**) when the sample was drop casted unto a formvar grid.

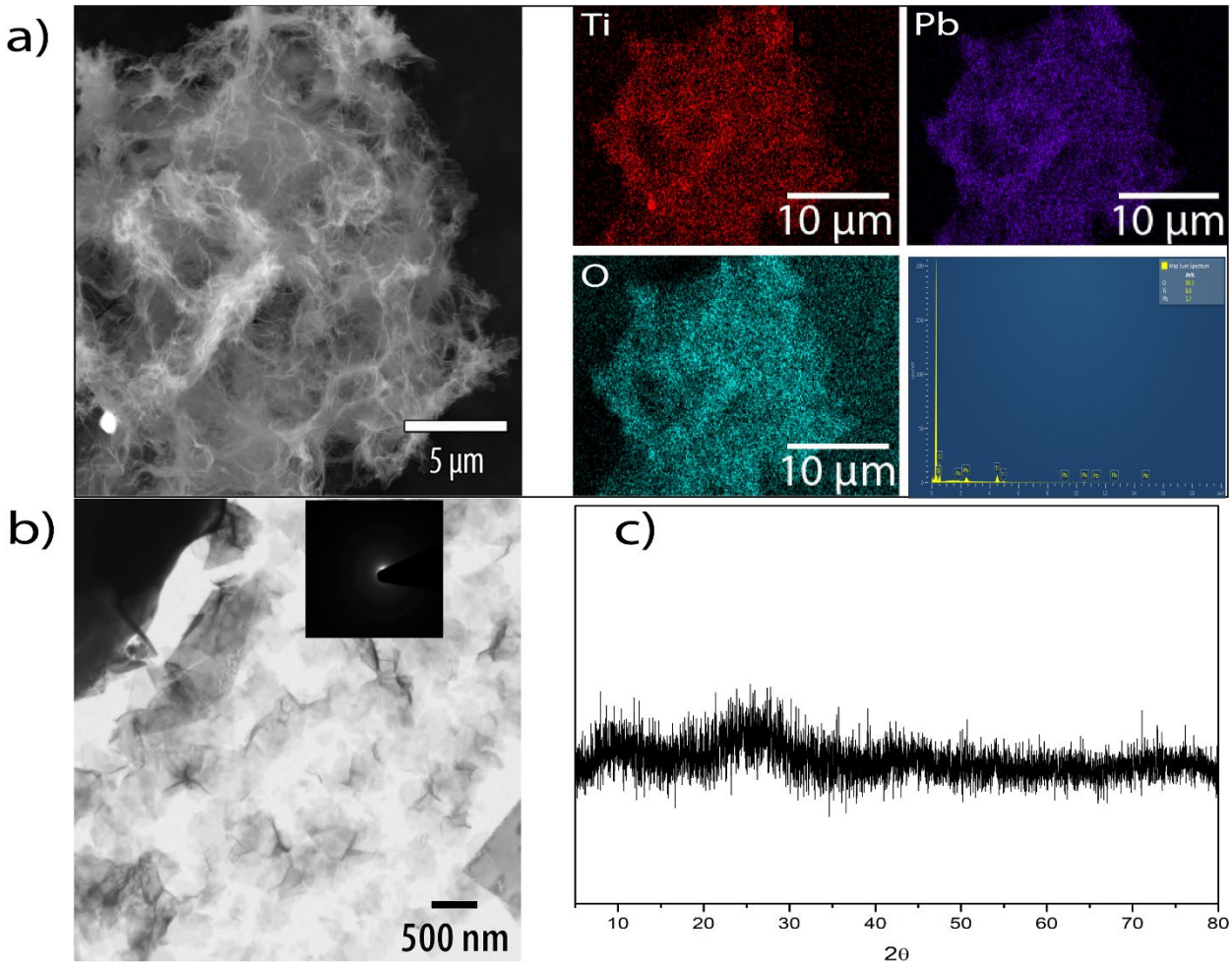

Figure 2.2. Characterization of Pb_x–TiO_2 nanosheets: a) STEM and EDX mapping, b) PXRD pattern, c) TEM and SAED, and d) EDX spectrum .

In addition to these techniques, we performed thermogravimetric analysis on the Pb_x–TiO_2 and $(TBA)_{1.07}Ti_{1.73}O_4$ nanosheets to observe the different mass losses upon heating. These measurements were conducted under N_2 atmosphere to prevent any atmospheric CO_2 from being trapped on the water layers of the material to minimize the reaction between Pb and CO_2. **Figure 2.3** shows the resulting plots of mass loss: the black curve corresponds to the $(TBA)_{1.07}Ti_{1.73}O_4$ nanosheets and the gold curve corresponds to the Pb_x–TiO_2 nanosheets. For both, we observe significant mass loss from ~100 to ~300 °C, which can be attributed to the loss of water between the layers of the nanosheets, with Pb_x–TiO_2 losing 38% mass and $(TBA)_{1.07}Ti_{1.73}O_4$ losing 34% mass. However, the $(TBA)_{1.07}Ti_{1.73}O_4$ nanosheets exhibit a second mass loss starting at 451 °C for an additional 6% reduction. This extra drop in mass can be attributed to the decomposition of the TBA^+. This decomposition has been previously noted at a similar temperature (434.2 °C) in the literature and identified as corresponding to the formation of CO_2(g). [19-20]

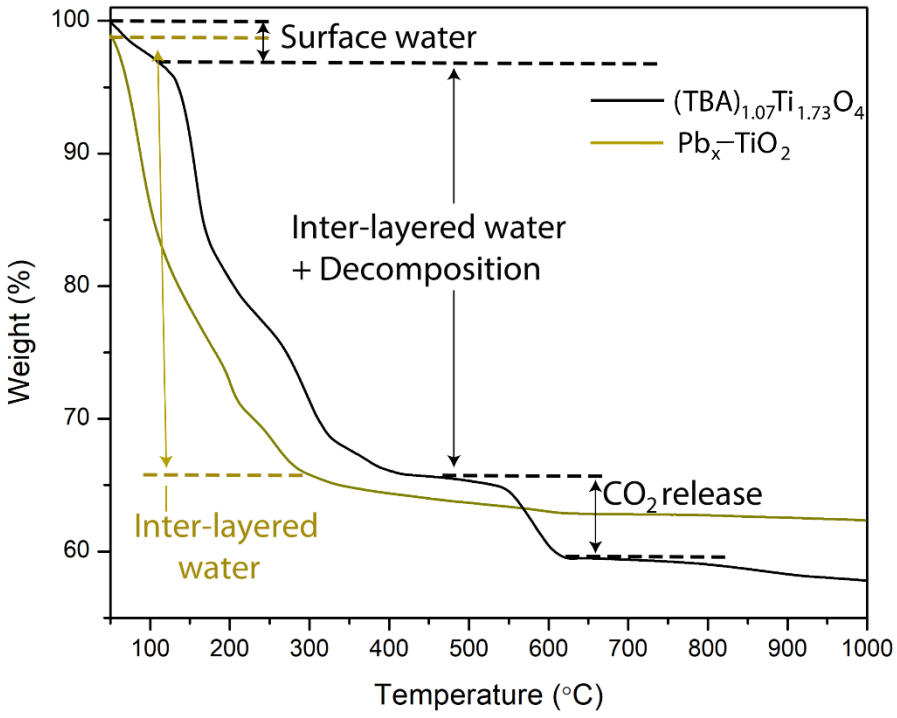

Figure 2.3. TGA analysis of $(TBA)_{1.07}Ti_{1.73}O_4$ and Pb_x–TiO_2 nanosheets

To obtain a more precise Pb:Ti value for Pb_x–TiO_2 nanosheets, we employed inductively coupled plasma-optical emission spectroscopy (ICP-OES). The results showed the presence of Ti at 948.1 ppb and Pb at 1184 ppb in the digested solution; thus, the calculated Pb:Ti value of 0.29:1 is somewhat more Pb-rich than the ratio determined by EDX (0.022:1). In general, however, ICP-OES provides more reliable elemental analysis results than EDX. Nevertheless, both measurements indicate that a significant amount of TBA^+ was exchanged for Pb^{2+} when the $(TBA)_{1.07}Ti_{1.73}O_4$ nanosheets were treated with $Pb(NO_3)_2$.

The exchange of H^+ for TBA^+ in $(TBA)_{1.07}Ti_{1.73}O_4$ was studied by Sasaki, et al., who characterized the amount of ions that intercalate into $(TBA)_{1.07}Ti_{1.73}O_4$ and their impact on nanosheet morphology.[21] Furthermore, extensive studies on the exchange of TBA^+ with smaller cations, including zinc, copper,[22] and lithium, but not lead, have been reported in the literature. These projects focused on using $(TBA)_{1.07}Ti_{1.73}O_4$ nanosheets to create new titanate materials by exchange of intercalated cations.[22-26]

Our subsequent experiments with Pb_x–TiO_2 nanosheets required dried, solid samples. Oven-dried material (635 Torr, 25 °C) changed to an off-white color, and SEM imaging showed extensive restacking into multi-micron thick, cracked films (**Figure 2.4a**); note the visible oriented layers in the cross-sectional view. The phenomenon of nanosheet restacking has been studied extensively, as described in the comprehensive review published by Sasaki.[27] This phenomenon has been used by others to fabricate superlattices and heterostructures by layer-by-layer deposition.[11, 13]

Once Pb_x–TiO_2 nanosheets restack, they cannot be re-dispersed in water, thus restacking must be avoided for the nanosheets to be useful for templated growth reactions. To accomplish this, the Pb_x–TiO_2 nanosheets were lyophilized (freeze-dried) or used "wet" (as-isolated but not dried). In cases where the material was used for subsequent reactions in water, the nanosheets were not dried; instead, they were used "wet" immediately after washing. **Figure 2.4b** shows an optical microscopy image of the wet Pb_x–TiO_2 used in these reactions, and **Figure 2.4c** shows a TEM image of these nanosheets after being drop cast from solution. From these images, we can see that the nanosheets do not re-stack but remain well dispersed in solution.

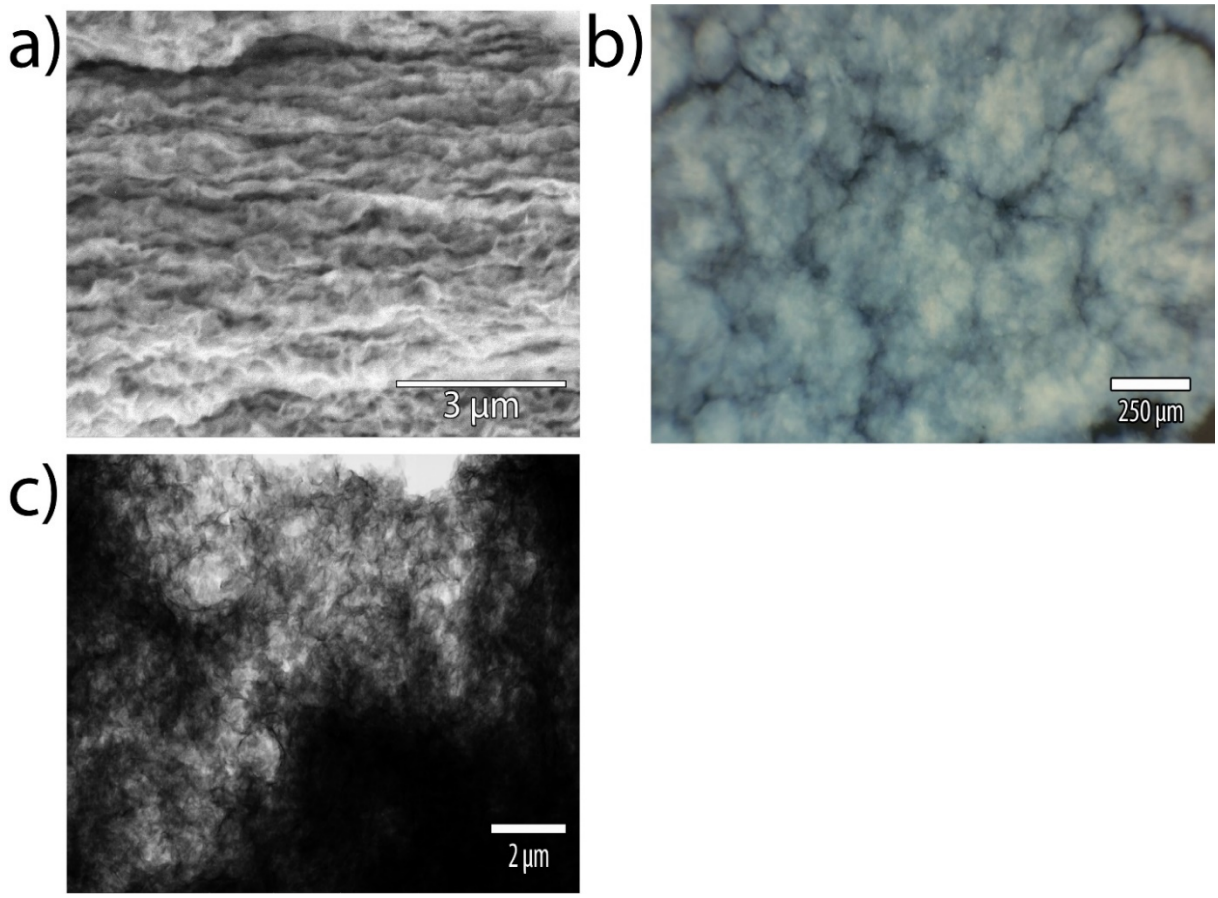

Figure 2.4. Characterization of Pb_x–TiO_2 nanosheets: a) STEM image of oven dried material taken from the edge of a cluster of nanosheets b) optical microscopy image of wet material, and c) TEM of freeze-dried material

Hydrothermal reactions of Pb_x–TiO_2 and H_x–TiO_2 precursors with lead sources

The initial experiments involved the acid-treated nanosheets, H_x–TiO_2. The reactions of the wet H_x–TiO_2 nanosheets with α-PbO (litharge, the tetragonal polymorph) were performed under hydrothermal conditions at 120°C utilizing a Teflon lined stainless steel autoclave. These initial reactions yielded three phases **(Figure 2.5a)**: (1) nanosheets of $PbTiO_3$ highlighted in the blue rectangle, (2) 10 to 500 nm (in length) thin rods highlighted in the green rectangle, and (3) the basic lead carbonate plumbonacrite [$(Pb_{10}(CO_3)_6O(OH)_6$] highlighted in the red rectangle. Moreover, as seen in **Figure 2.5b**, PXRD confirmed the product mixture to be composed of $PbTiO_3$ (blue), Pb_3O_7 (green), and plumbonacrite (red).

The rods were examined in more detail by EDX (**Figure 2.5c**), which showed overlapping lead and oxygen but no titanium, further confirming Pb_3O_7 as the phase identified by PXRD. Nanorods of various lead oxides have been reported in the literature. For example, Shi et al. showed the formation of PbO_2 nanorods from the scrolling of nanosheets under hydrothermal conditions.[28] The scrolling was attributed to the relief of surface tension stress. Aside from this study, PbO and Pb_3O_4 have been prepared in nanorod morphologies.[29,30]

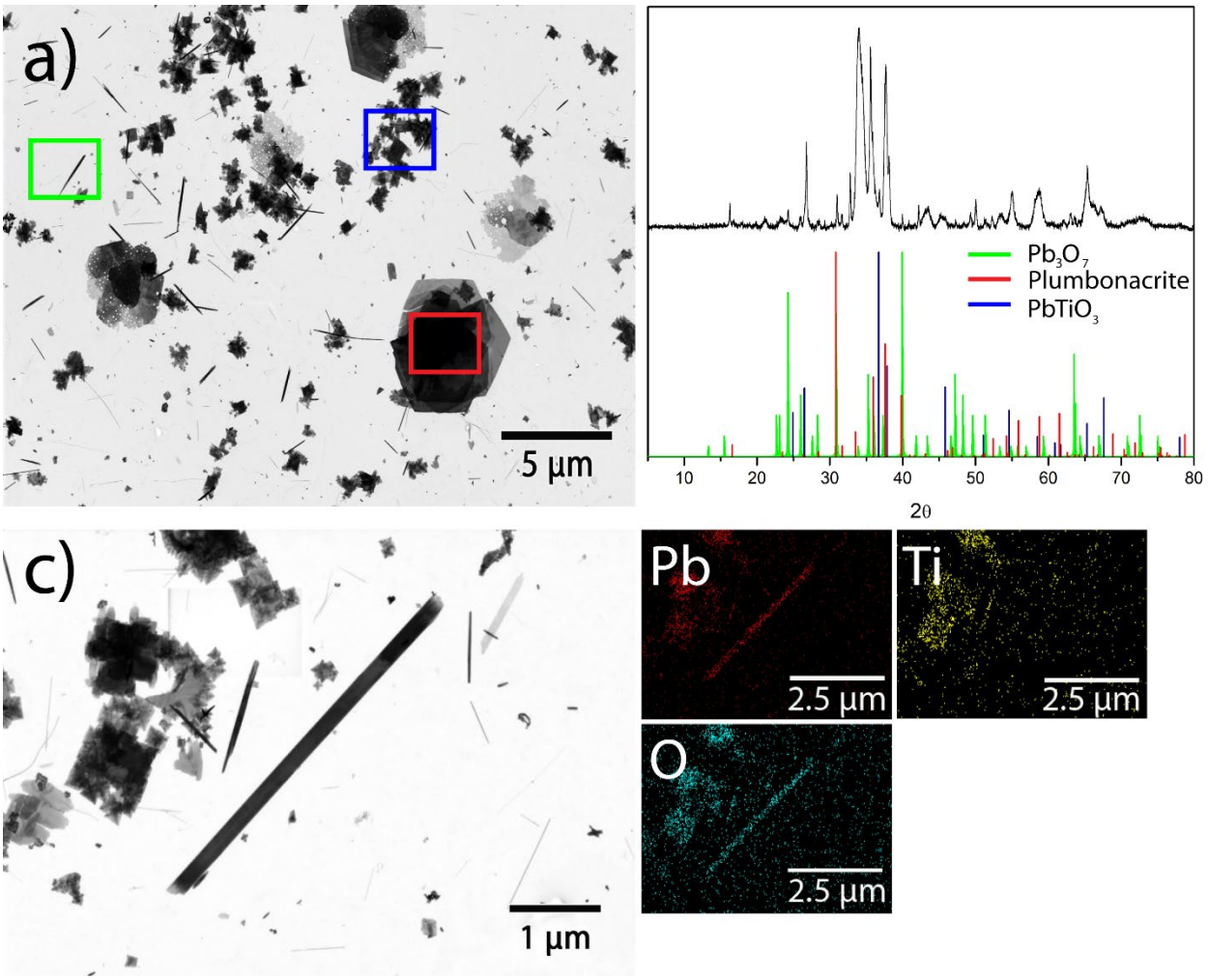

Figure 2.5. a) STEM image of product mixture from the reaction of H_x–TiO_2 with α-PbO, b) PXRD of this product mixture, and c) STEM image and corresponding EDX mapping of the nanorods.

The formation of plumbonacrite from reactions with atmospheric CO_2(g) was a common occurrence throughout this study. The presence of this phase can be identified readily by electron microscopy because of its distinct hexagonal structure and morphology (**Figure 2.6**), which was fully characterized by TEM paired with SAED. To better understand the formation and role of plumbonacrite, a pure sample was prepared by flowing CO_2(g) through an aqueous dispersion of lead oxide and lead acetate (**Figure 2.6**). These details and the full characterization of plumbonacrite are detailed in chapter VI.

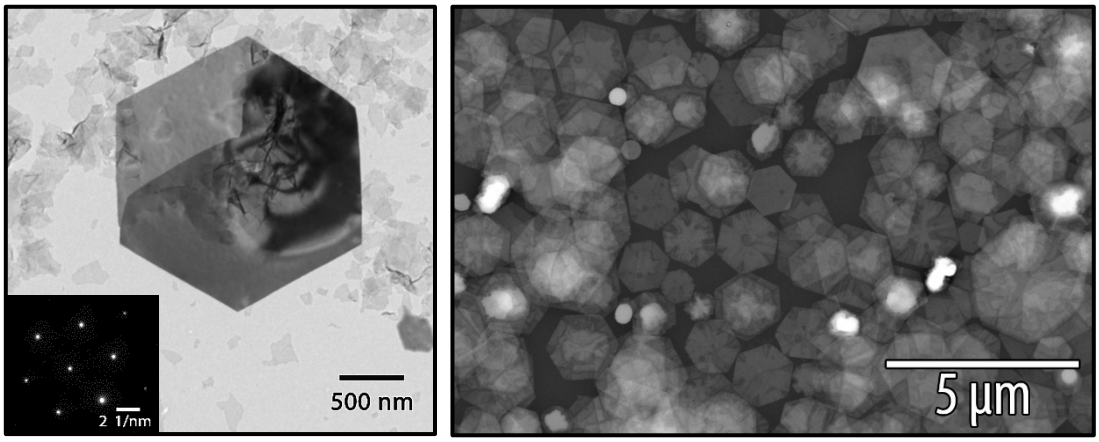

Figure 2.6. a) TEM and b) SEM of as-synthesized plumbonacrite.

Reactions starting with plumbonacrite as a source of lead resulted in only more plumbonacrite formation and the isolation of unreacted $(H,Pb)_xTiO_2$ nanosheets. These results suggest that plumbonacrite is not an intermediate in the formation of $PbTiO_3$, but rather is a side product. Given the difficulties related to isolating $PbTiO_3$ mixed with plumbonacrite, we focused on preventing the formation of plumbonacrite in the first place.

Hydrothermal reactions of Pb_x–TiO_2 with PbO ultimately led to the successful isolation of $PbTiO_3$ nanosheets, thus this precursor was used for most of the work described here. **Scheme 1** shows the routes we examined to optimize the formation of $PbTiO_3$ nanosheets.

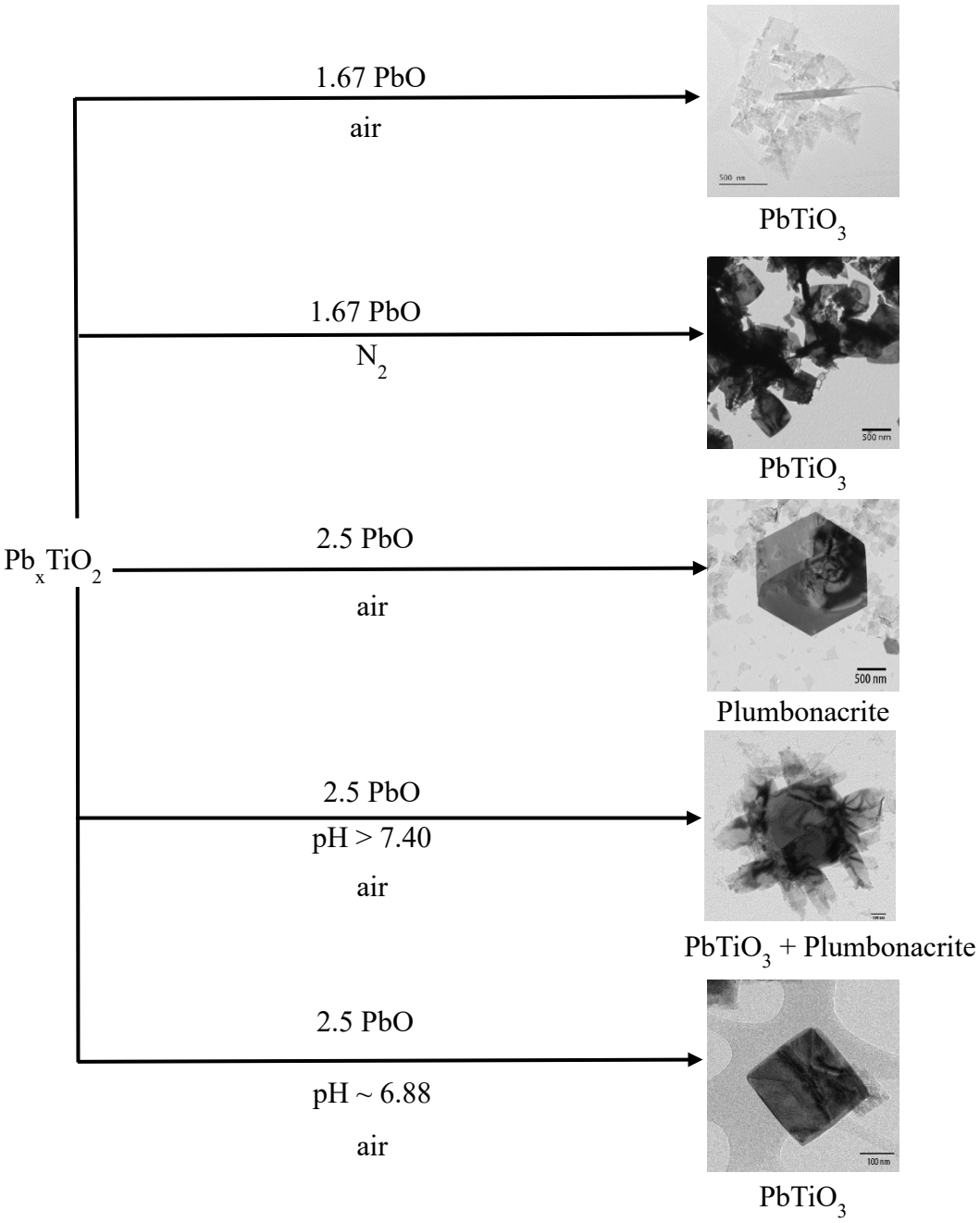

Scheme 1. Pathways leading to $PbTiO_3$ nanosheets

Temperature studies

Reaction temperatures helped optimize the formation of $PbTiO_3$ nanosheets. Examined temperatures ranged from 105 to 250 °C, and products were evaluated by TEM (**Figure 2.7**). For the 105 °C reaction, the product mixture contained unreacted precursor (PbO and Pb_x–TiO_2) and plumbonacrite; no formation of $PbTiO_3$ nanosheets was observed. At 120 °C, the reaction appeared to go to completion, with no unreacted precursors remaining; products included $PbTiO_3$ nanosheets and plumbonacrite. At 180 °C reaction also yielded $PbTiO_3$ nanosheets and plumbonacrite, but the previously mentioned nanorods of lead oxide also started to form.

At the highest temperature of 250 °C, the reaction produced $PbTiO_3$ nanosheets and plumbonacrite, as well as some hollowed structures. Although hollowed structures have been reported in literature, including hollowed nanospheres[31-33] nanoprisms,[34-35], and nanodonuts[36] this was not our main interest. For subsequent reactions, we maintained a temperature of 120 °C to minimize side reactions and product fragmentation.

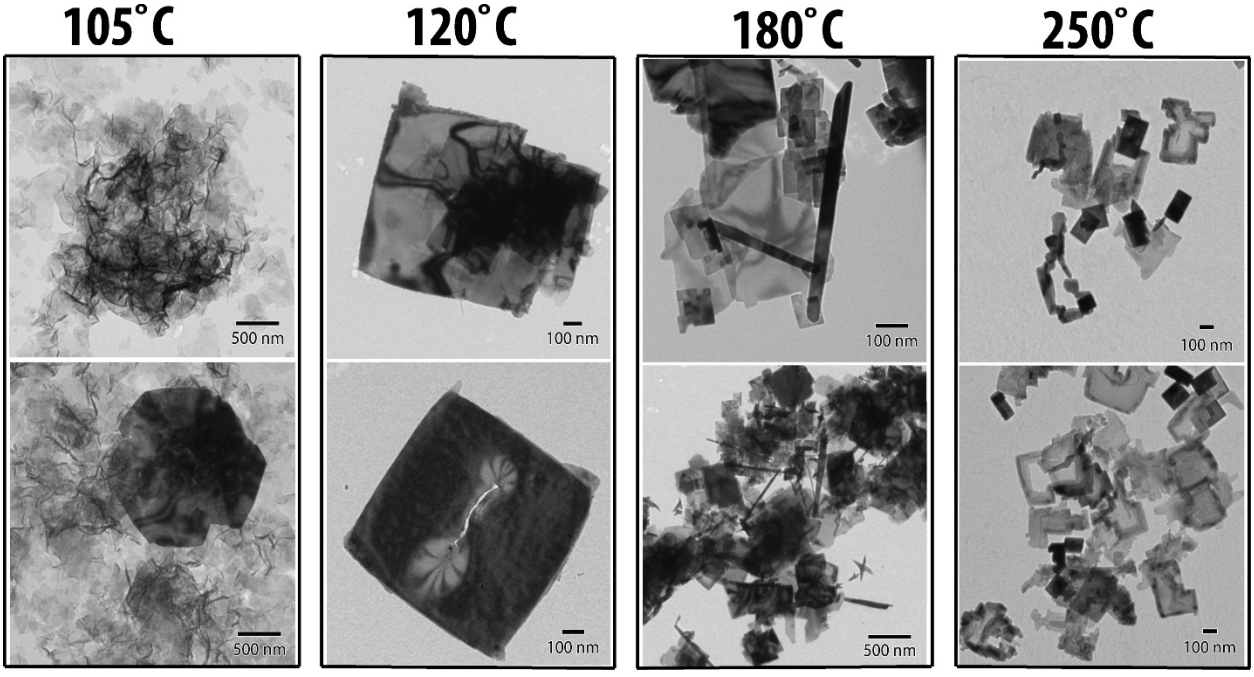

Figure 2.7. Temperature study of $PbTiO_3$ nanosheet formation; imaging by TEM.

pH studies

In addition, pH could be used to control plumbonacrite formation. Plumbonacrite starts to form at a pH of 7.4, and the starting pH of a typical α-PbO + Pb_x–TiO_2 reaction is 8.4 because PbO is basic. To drop the reaction pH, 1 M HCl(aq) was added in controlled quantities. With a pH of less than 6.0, the PbO dissolves in the presence of HCl(aq), generating $PbCl_2$. As more $PbCl_2$ forms, the dispersion turns colorless (in contrast to the orange color of a-PbO). Under these conditions, no reaction occurs between the $PbCl_2$ and Pb_x–TiO_2. These results can be seen in **Figure 2.8** (first column) under pH of 3.8, the point at which all a-PbO converts into $PbCl_2$. The pH that led to the best result was ~6.8; at this pH, $PbTiO_3$ nanosheets formed cleanly without plumbonacrite (**Figure 2.8**, second column). When the pH was increased to 10.5, $PbTiO_3$ nanosheets and plumbonacrite occur together, which can be observed in the third column of **Figure 2.8**.

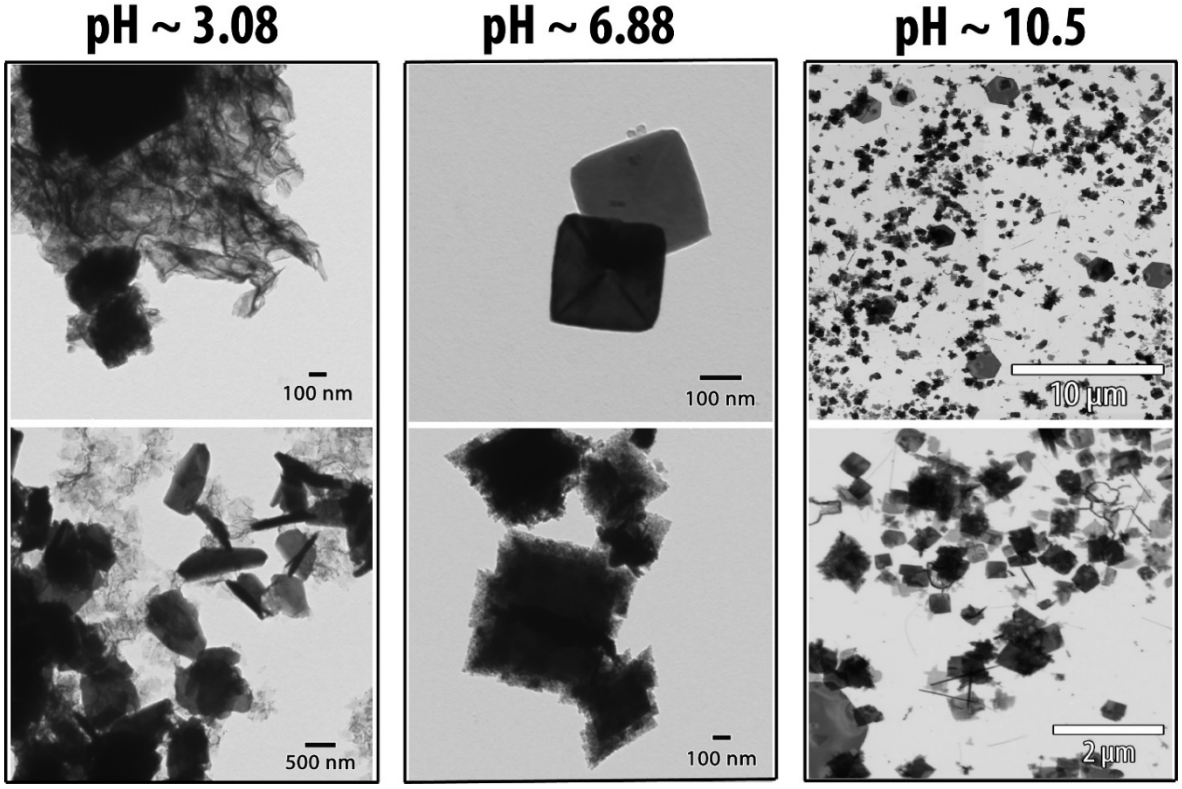

Figure 2.8. TEM images of reactions at pH 3.08, 6.88, and 10.5.

Once we established that a pH of 6.88 provided optimum results, the reaction of α-PbO with Pb_x–TiO_2 was reproduced and analyzed. PXRD (**Figure 2.9**) showed the formation of nanostructured $PbTiO_3$ (nanostructuring indicated by the peak broadening); the reference pattern in blue corresponds to single crystal data for tetragonal $PbTiO_3$ (ICDD #01-081-9527). The pattern also reveals the presence of Ti_4O_7 (ICDD #04-005-4533), a likely side product from unreacted Pb_x–TiO_2. Rietveld refinement of the PXRD pattern provided a ratio of 94:6 for $PbTiO_3$:Ti_4O_7 (**Figure S2.1**). Even when the PbO appears present given the PXRD, when the phase was added to the program the fitting for PbO was negative as can be seen in the supporting information (**Figure S2.2**).

Interestingly, Ti_4O_7, which is one of the so-called Magnéli titanium oxides Ti_nO_{2n-1} ($4 \leq n \leq 10$), has a structure based on edge-sharing TiO_6 octahedra similar to the ones found in the rutile polymorph of TiO_2.[37] This material has been investigated for its electronic and phononic properties.[38] Magnéli titanium oxides have been synthesized by various routes ranging from microwave rapid heating[39-41] to solid state reactions.[37, 42-43] This material is formed by the reduction of (usually) anatase TiO_2. The reducing agent creates the structural vacancies that give Magnéli titanium oxides their unique electronic properties. In our system, the nanosheets of Pb_x–TiO_2 could be converting to Ti_4O_7 by a mechanism in which Pb^{2+} strips oxygen from the TiO_2 framework to create vacancies.

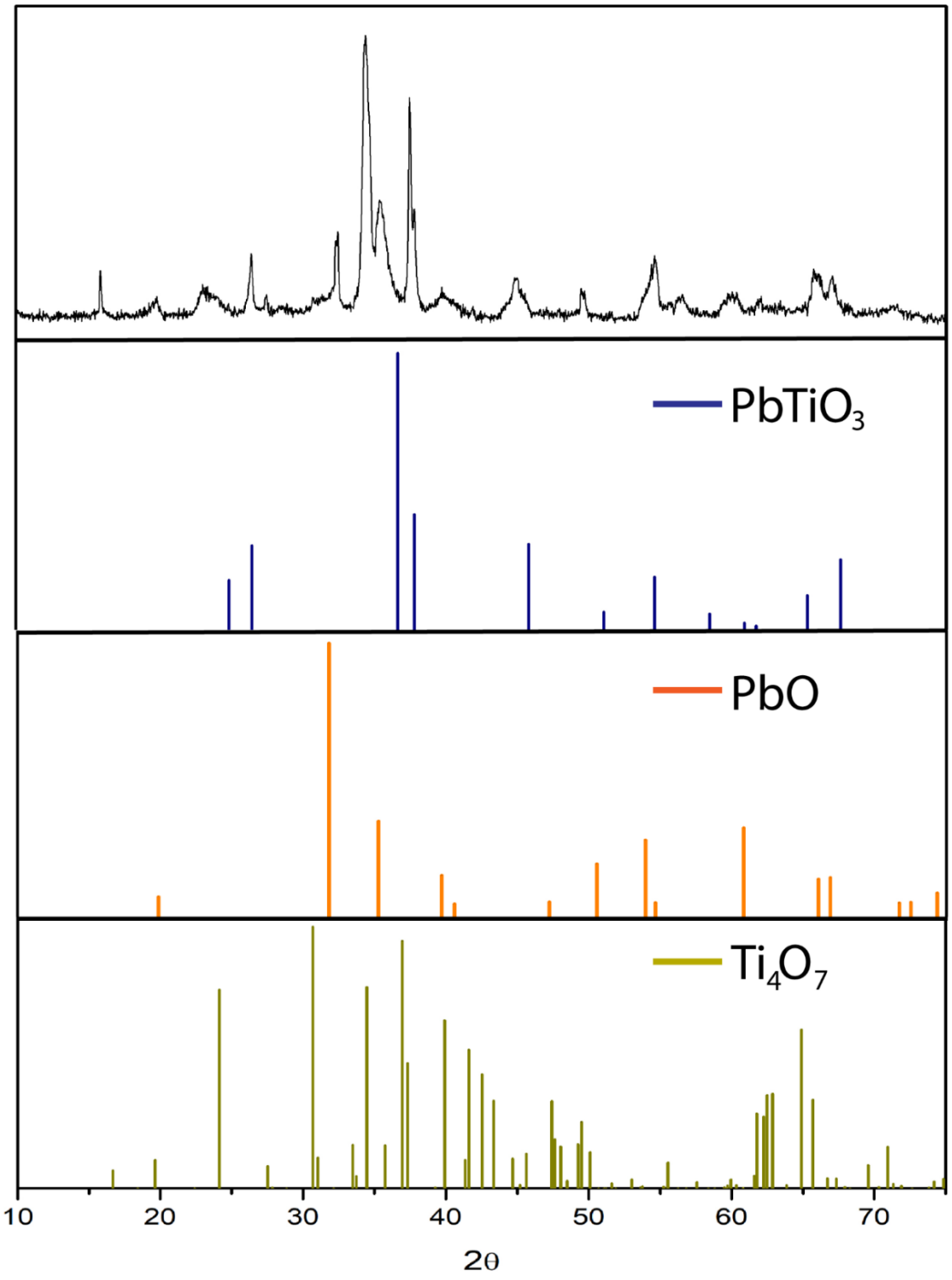

Figure 2.9. PXRD of the isolated product from the hydrothermal reaction of Pb_x–TiO_2 and α-PbO at pH 6.88.

As mentioned in Chapter I, the crystal structure of $PbTiO_3$ must be in the tetragonal phase to support ferroelectric properties. Once the structure changes to the cubic form, the dipole moment is lost. However, it proved difficult to distinguish the tetragonal and cubic phase based on PXRD data for several reasons: the diffraction patterns of the tetragonal and cubic structures nearly overlap, the nanomorphology increases peak broadening, the 2D morphology causes orientation effects, and the product mixture is not phase pure, containing Ti_4O_7 in addition to $PbTiO_3$. For example, **Figure 2.10** shows calculated PXRD patterns (simulated with a particle size of 0.025 μm) that illustrate the overlap between cubic and tetragonal $PbTiO_3$ patterns. For these reasons, further characterization methods were used to clarify the structure of $PbTiO_3$ nanosheets, specifically high resolution TEM (HRTEM) with FFT measurements.

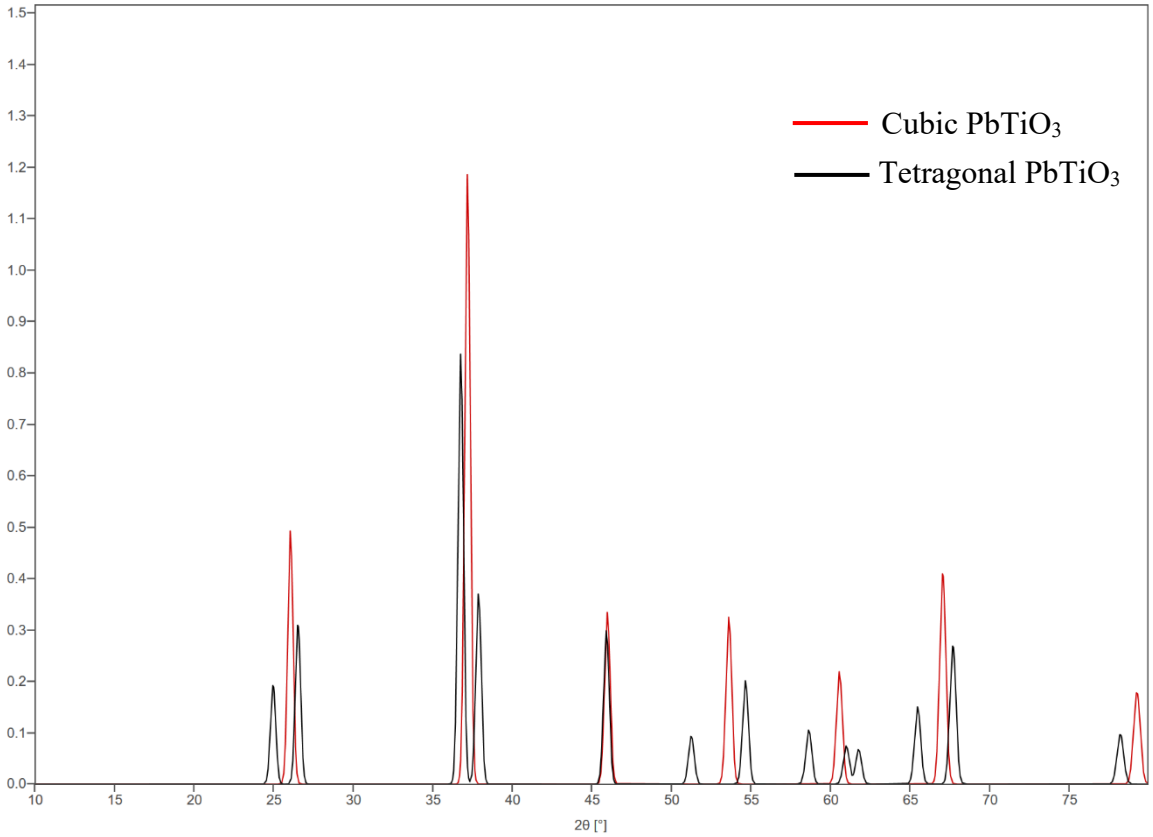

Figure 2.10. Simulated PXRD patterns of cubic (ICDD# 01-080-7941) and tetragonal (ICDD# 01-081-9527) $PbTiO_3$.

For reactions conducted at a pH of 6.88, two product morphologies were observed by HRTEM. The first, identified as $PbTiO_3$ nanosheets with a granular texture, is distinguished by clearly visible 25-150 nm-sized domains (**Figure 2.11a**); the blue square shows a representative area used for fast Fourier transform (FFT) measurements and atomic resolution studies. The FFT pattern (**Figure 2.11b**) is consistent with the (101) plane of tetragonal $PbTiO_3$ and matches well with the calculated electron diffraction pattern (**Figure 2.11c**). The *c/a* ratio was calculated to be 1.051, confirming that the nanosheets exhibit the tetragonal crystal structure, which typically possesses a *c/a* ratio of 1.045–1.055.[44] In addition, the *d*-spacing from HRTEM (measurements from several areas were averaged) of 2.83 Å (**Figure 2.11e**) compares closely with the known value of 2.838 Å for tetragonal $PbTiO_3$ and is distinct from the expected value of 2.803 Å for cubic $PbTiO_3$. These crystallographic values were obtained from a single crystal x-ray diffraction study of tetragonal $PbTiO_3$ (ICDD #01-070-7729). The crystallographic orientation of the sample [(101) plane] is shown in **Figure 2.11f** with Pb being grey, Ti being blue, and O being red. Blue arrow is pointing towards a titanium atom behind the oxygen atom.

Based on the atomic resolution studies that show a granular texture composed of different domains oriented in the same direction(edge of the domains can be seen in yellow on **Figure 2.11d**), we can propose that these $PbTiO_3$ nanosheets via an oriented attachment mechanism. Such oriented attachment mechanisms have been proposed and observed for a wide range of nanomaterials, including nanofibers,[45-46] nanocrystals,[47-48] and nanosheets.[49-51]

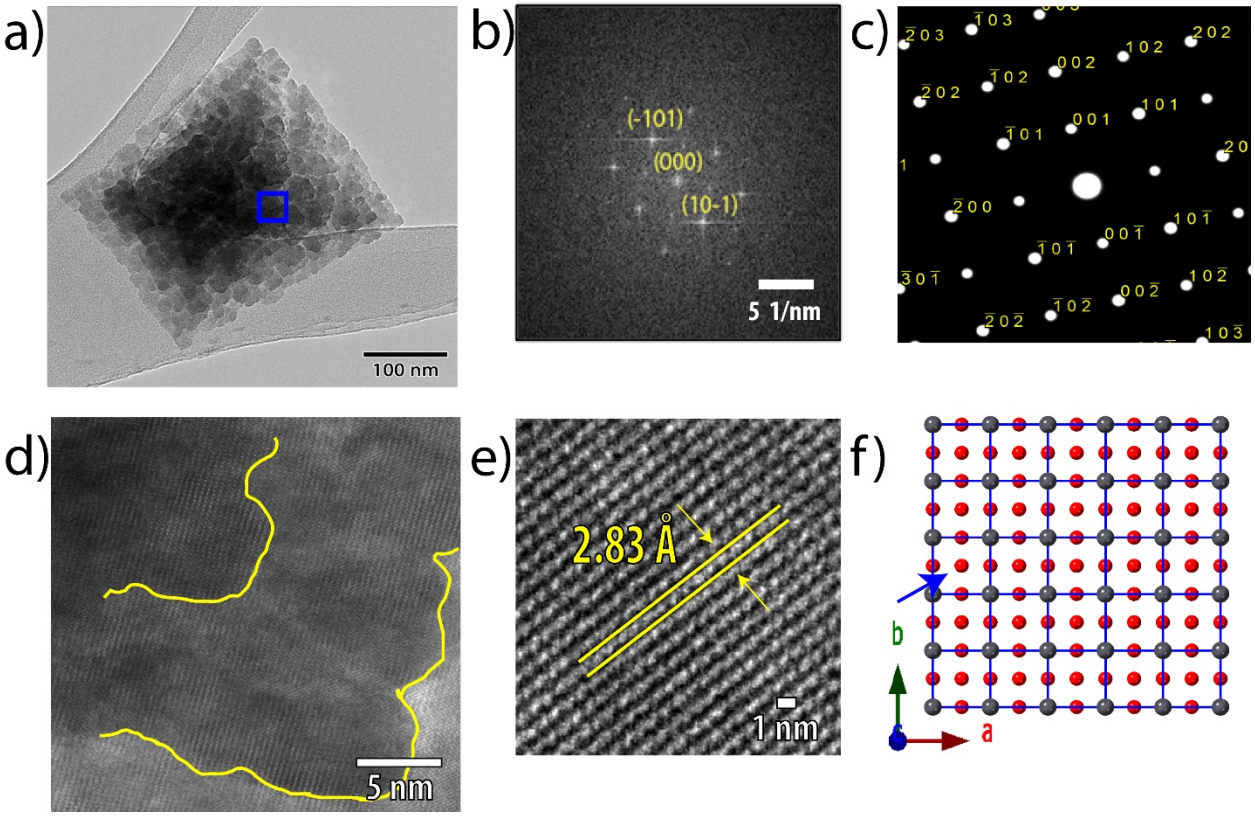

Figure 2.11. a) HRTEM of a single, granular $PbTiO_3$ nanosheet, b) FFT of the boxed area in panel a, and c) corresponding calculated electron diffraction pattern, d) HRTEM image with defined domains e) *d*-spacing analysis (from same boxed area in panel a), and f) crystallographic view of the (101) plane for tetragonal $PbTiO_3$ (ICDD# 01-070-7729).

The second morphology observed for products of a-PbO + Pb_x–TiO_2 reactions conducted at a pH of 6.88 was identified as well-formed, continuous $PbTiO_3$ nanosheets (**Figure 2.12a**). The FFT and atomic resolution studies were performed on different areas of the same nanosheet for the purpose of averaging; **Figure 2.12a,** in blue, shows a representative area for these measurements. Again, the FFT (**Figure 2.12b**) is consistent with the (101) plane of $PbTiO_3$ (calculated electron diffraction shown in **Figure 2.12c**), as is the *d*-spacing (**Figure 2.12d**) of 2.82 Å. The *c/a* ratio of 1.047 confirmed that these nanosheets also exhibit the tetragonal crystal structure of $PbTiO_3$. **Figure 2.12e** shows the structure view of the (101) plane for the tetragonal $PbTiO_3$ (ICDD# 01-070-7729) with Pb being grey, Ti being blue, and O being red. Blue arrow is pointing towards a titanium atom behind the oxygen atom.

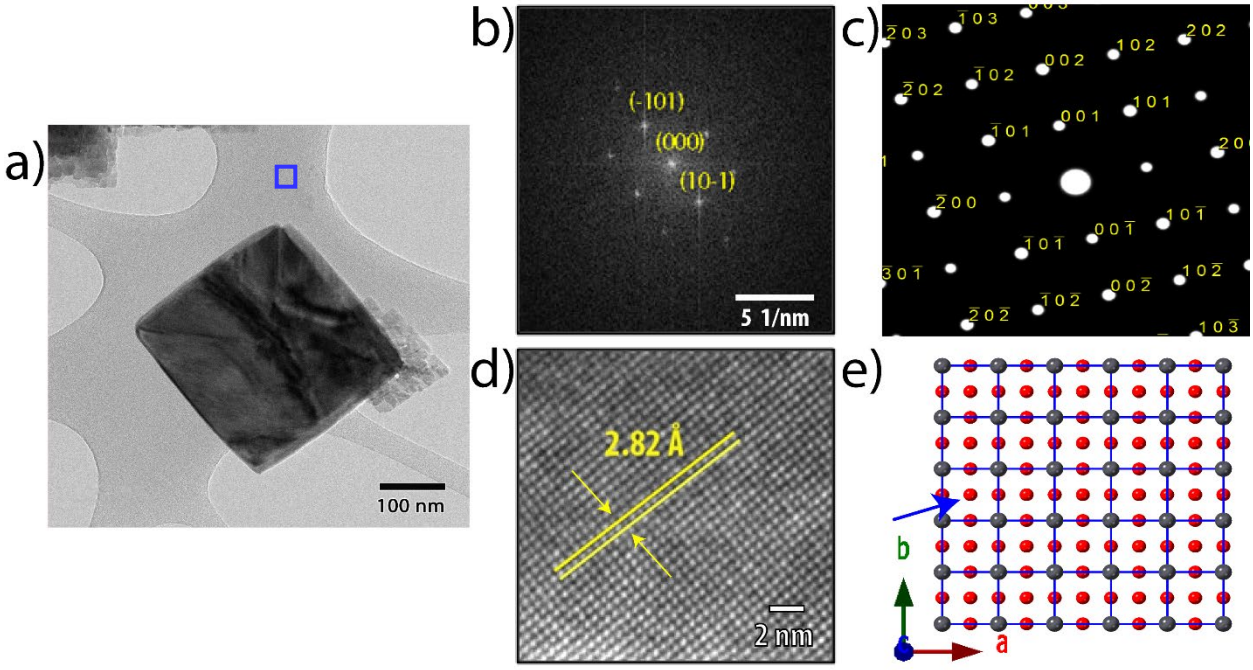

Figure 2.12. a) HRTEM of a single, $PbTiO_3$ nanosheet, b) FFT of the boxed area in panel a, and c) corresponding calculated electron diffraction pattern, d) HRTEM image with defined domains e) crystallographic view of the (101) plane for tetragonal $PbTiO_3$ (ICDD# 01-070-7729).

In the case of perovskite materials, the axis of polarization is the c axis.[52] For our measurements, the error on the measuring of the *d*-spacing is so small that it tis hard to match it to the correct plane (the difference being 0.01 Å). However, the preliminary piezoelectric data of our nanosheets of tetragonal $PbTiO_3$ exhibit a good ferroelectric response. This would help determine the orientation of the nanosheets. In **Figure 2.13a**, we can see the structure of tetragonal $PbTiO_3$ (ICDD# 01-070-7729) with the preferred orientation of the axis of polarization. **Figure 2.13b**, shows the same structure, but with the first layer of atoms removed to help visualize the Ti atoms behind the O atoms.

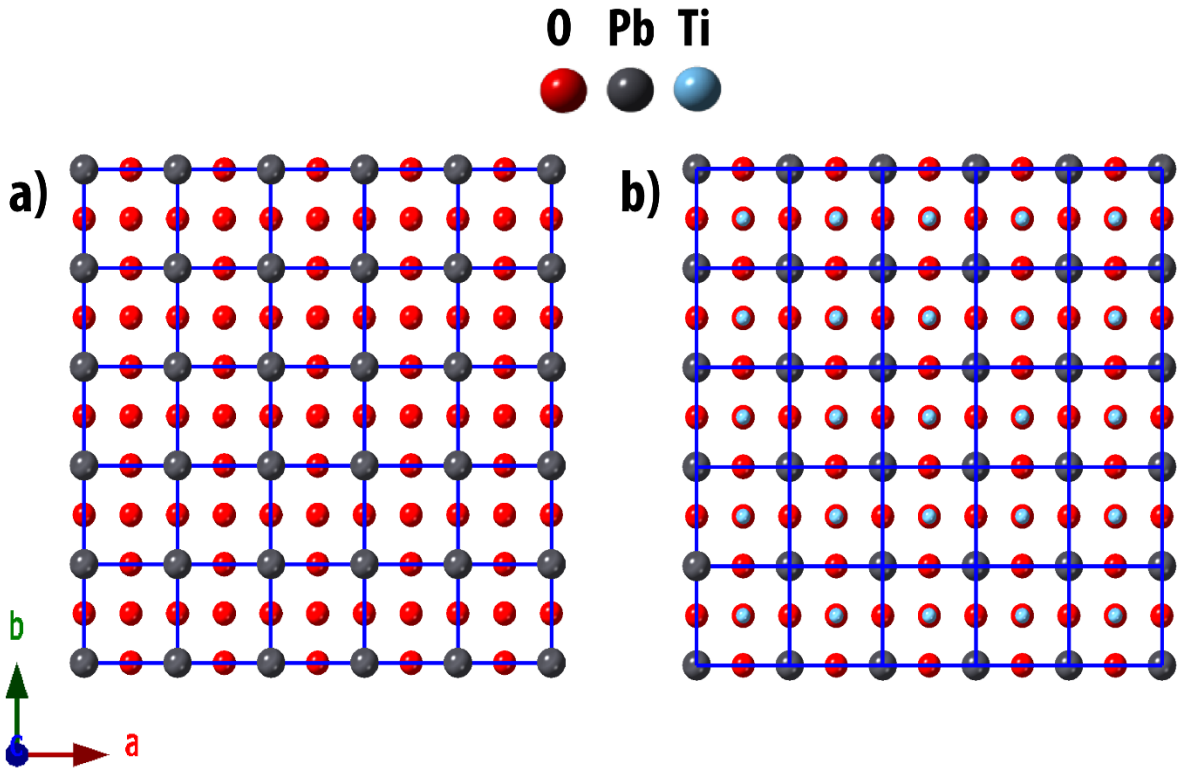

Figure 2.13. a) structure and b) first layer of atoms removed of tetragonal $PbTiO_3$ (ICDD# 01-070-7729).

Air-free reactions of $PbTiO_3$

To better study the reaction between Pb_x–TiO_2 and α-PbO, we next aimed to create a reaction environment in which plumbonacrite could not form, i.e. a CO_2-free atmosphere. However, this is not as simple as using a conventional inert gas-filled glovebox because the reaction involves water. Therefore, we converted an old glove box into what we called a "wet box" to provide a CO_2-free environment while preparing hydrothermal reactions under N_2 atmosphere. To ensure that CO_2 was not present, all water was degassed prior to being introduced to the wet box, and the Pb_x–TiO_2 was used in freeze-dried solid form. In a representative procedure in the wetbox, a reaction mixture of Pb_x–TiO_2 and α-PbO in water was prepared and sealed in a Teflon-lined stainless steel autoclave before being transferred to the 120 °C oven. Once the reaction was done, the autoclave was returned to the wetbox for workup: with all sample handling occurring within the wetbox, the product mixture was bath-sonicated for 1 h and centrifuged at 3250 rpm for 1 h. Then the product was transferred to a Schlenk flask, sealed, and removed from the wetbox. The product was dried under vacuum using a Schlenk line.

The product from the initial wetbox trials contained two phases. Unlike previous reaction products that consisted of $PbTiO_3$ nanosheets (yellow) and plumbonacrite (white), the product made by the wetbox route had an orange tint that suggested the presence of α-PbO. TEM images showed unreacted sheets of Pb_x–TiO_2 and nanoparticles thought to be unreacted PbO (**Figure 2.14a**), as well as large plumbonacrite sheets (**Figure 2.14b**), and small quantities of $PbTiO_3$ nanosheets. Because reaction setup and workup were conducted inside the wetbox, the presence of plumbonacrite suggested that it formed directly on the TEM grid upon exposure to air.

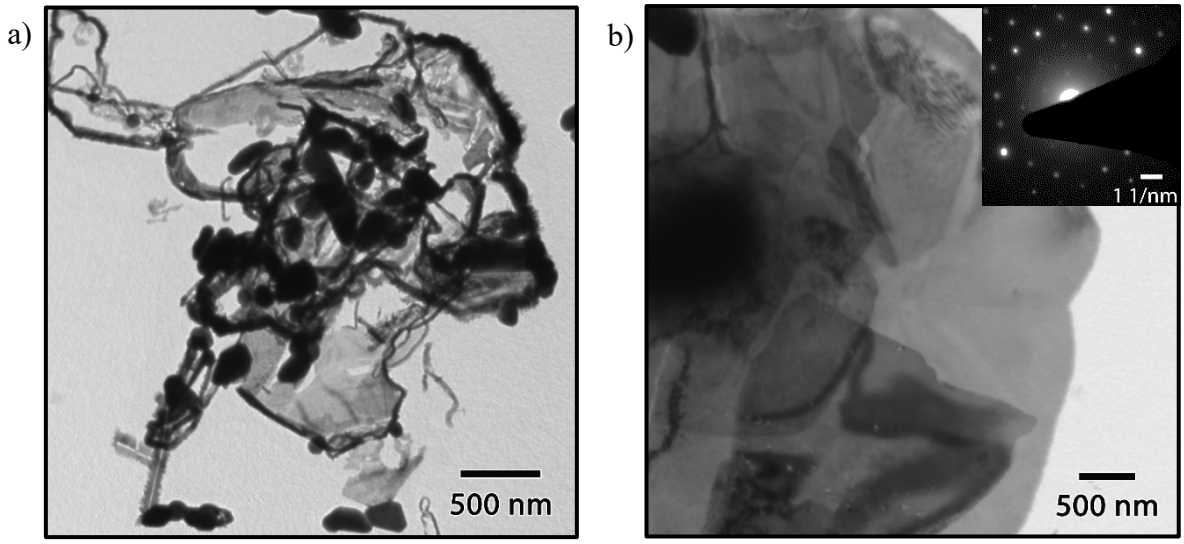

Figure 2.14. Products from the hydrothermal reaction of Pb_x–TiO_2 and α-PbO (wetbox setup under N_2): a) PbO oxide aggregates with unreacted Pb_x–TiO_2, and b) few-layered plumbonacrite, with corresponding SAED (inset).

These results also suggested that the amount of α-PbO added to this reaction was in excess. Therefore, the ratio between Pb_x–TiO_2 and α-PbO was varied under CO_2-free conditions to establish the minimum amount of α-PbO needed to produce $PbTiO_3$, with no excess left to react with atmospheric CO_2 and create plumbonacrite. This set of experiments surveyed α-PbO:Pb_x–TiO_2 from 1:1 to 2.5:1. We observed that ratios greater than 1.8:1 led to excess PbO present at the end of the reactions; however, at lower ratios, especially 1.67:1, $PbTiO_3$ nanosheets formed without plumbonacrite contamination. **Figure 2.15** shows the nanosheets synthesized from this optimized reaction.

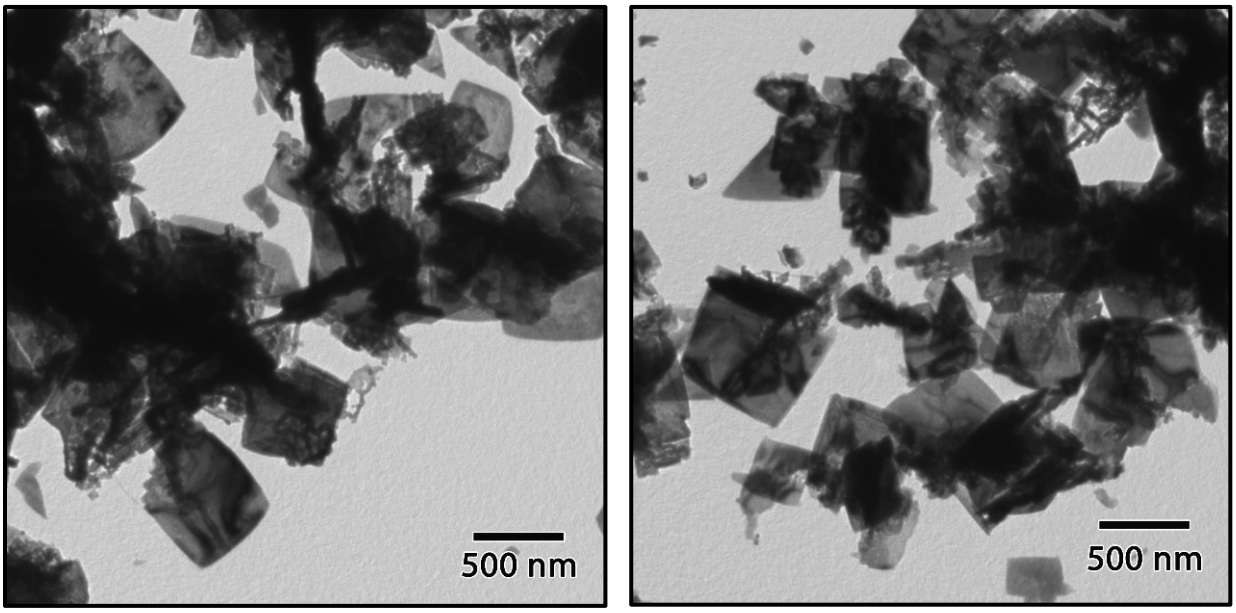

Figure 2.15. TEM images of $PbTiO_3$ nanosheets formed using the optimized α-PbO:Pb_x–TiO_2 of 1.67:1 (wetbox setup under N_2).

Synthesis of $PbTiO_3$ nanosheets

The insights revealed by all these studies were combined into an optimized synthesis of $PbTiO_3$ nanosheets. Importantly, the results from reactions conducted under N_2 were used to improve reactions conducted under atmospheric reactions; by using the optimized PbO:Pb_x–TiO_2 ratio of 1.67:1, plumbonacrite formation was avoided, even in the presence of atmospheric CO_2. The success of this approach provided additional proof that plumbonacrite is not an intermediate in $PbTiO_3$ formation, but rather a side product generated when excess α-PbO reacts with atmospheric CO_2.

A time study, shown in **Figure 2.16**, showed the formation of $PbTiO_3$ nanosheets over periods of hours to weeks. Nanosheets are visible at 1 day, but unreacted Pb_x–TiO_2 (blue squares) is also present. After 5 days, the $PbTiO_3$ nanosheets appear fully formed. However, additional reaction time has a negative effect: after 2 weeks at 120 °C, the nanosheets started to break into nanoparticles.

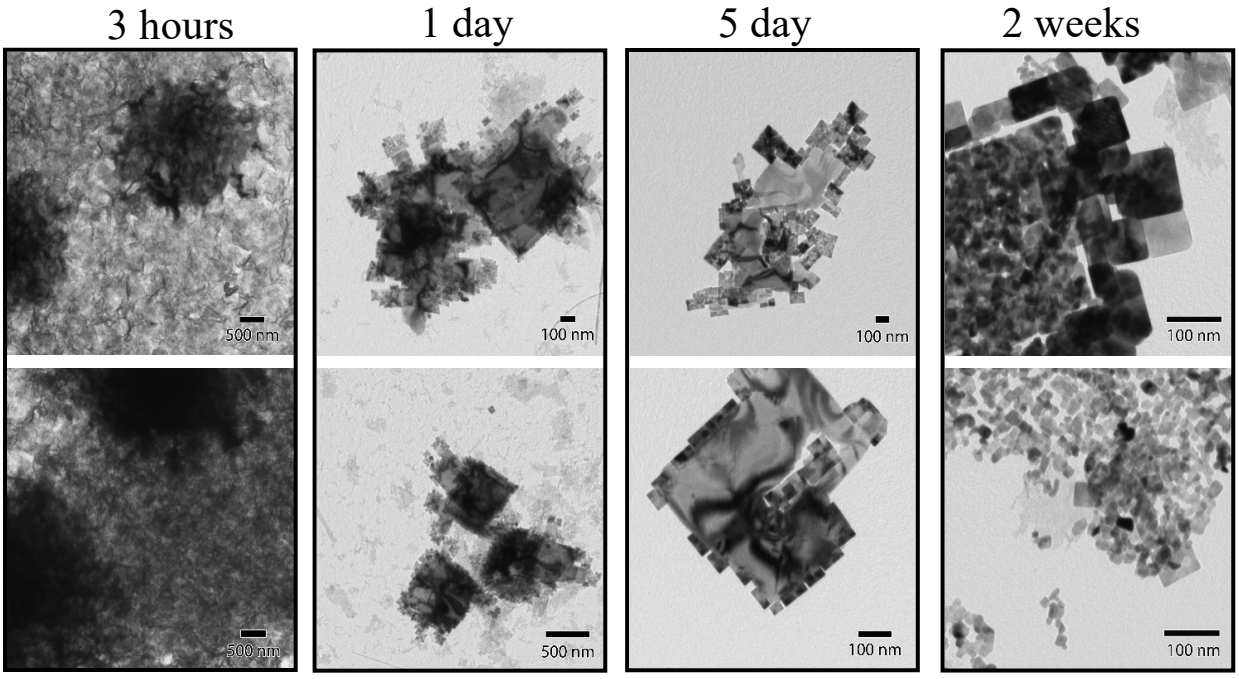

Figure 2.16. TEM images of the time study for the formation of $PbTiO_3$ using optimized stoichiometry and setup.

After a reaction time of 5 days and workup, the solid product was immediately freeze dried, providing a yellow powder. Quick freeze drying was important here to prevent restacking and also to minimize thermal decomposition of the $PbTiO_3$ nanosheets. Drying the $PbTiO_3$ nanosheets at 25 °C resulted in the formation of plumbonacrite, likely due to regenerated PbO reacting readily with atmospheric CO_2. PXRD (**Figure 2.17**) showed the presence of both $PbTiO_3$ (ICDD #00-066-0336) and Ti_4O_7 (ICDD #04-005-4533). Reitveld refinement provide a 90:10 ratio of $PbTiO_3$:Ti_4O_7, meaning that the proportion of $PbTiO_3$ here is significantly lower than that found from earlier reactions at pH 6.88 (**Figure 2.9**).

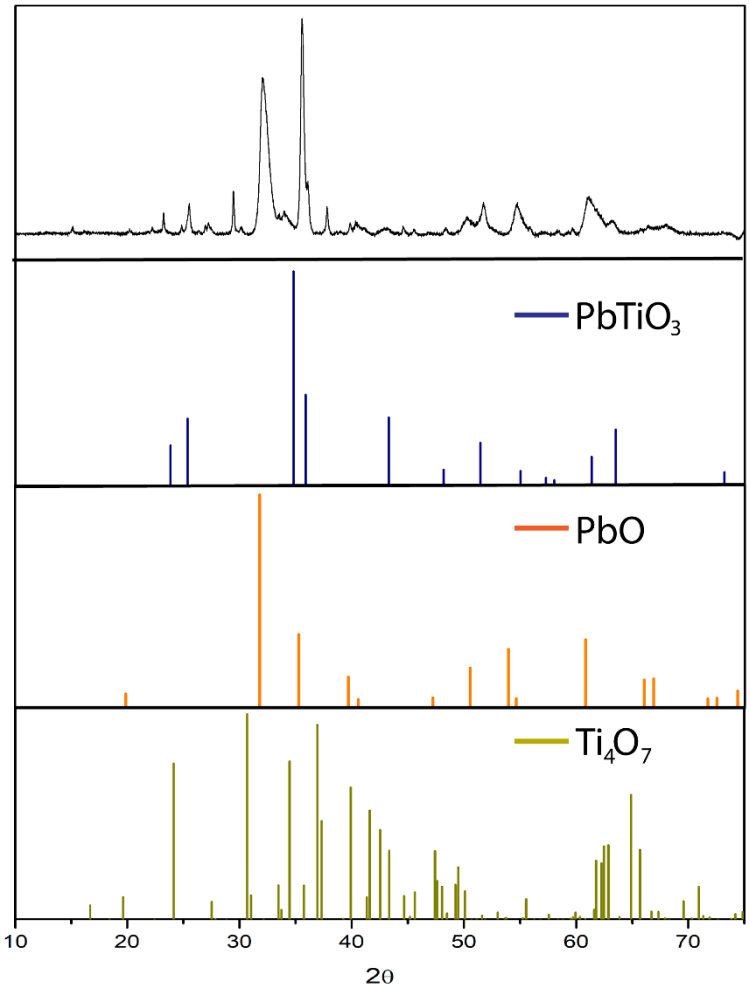

Figure 2.17. PXRD on the isolated product from the Pb_x–TiO_2 + α-PbO reaction

We analyzed two products (from two different reactions) by HRTEM to evaluate nanosheet morphology and structure. The first was the product of a 5-day reaction, chosen because the $PbTiO_3$ nanosheets appeared fully formed and not mixed with plumbonacrite. As can be seen in **Figure 2.18a-d**, the nanosheets are continuous, with no granular morphology or obvious domains. FFT measurements (**Figure 2.18b**) were consistent with the (101) plane of $PbTiO_3$ (calculated electron diffraction shown in **Figure 2.18c**), the same orientation of tetragonal $PbTiO_3$ shown in **Figure 2.18f** with Pb being grey, Ti being blue, and O being red. Blue arrow is pointing towards a titanium atom behind the oxygen atom. . The *c/a* ratio for this nanosheet was 1.021, confirming the tetragonal $PbTiO_3$ structure. Additionally, atomic resolution studies (**Figure 2.18e**) showed the *d*-spacing to be 2.81 Å, which can be matched to the tetragonal $PbTiO_3$ *d*-spacing of 2.838Å, further confirming the identity of the nanosheets.

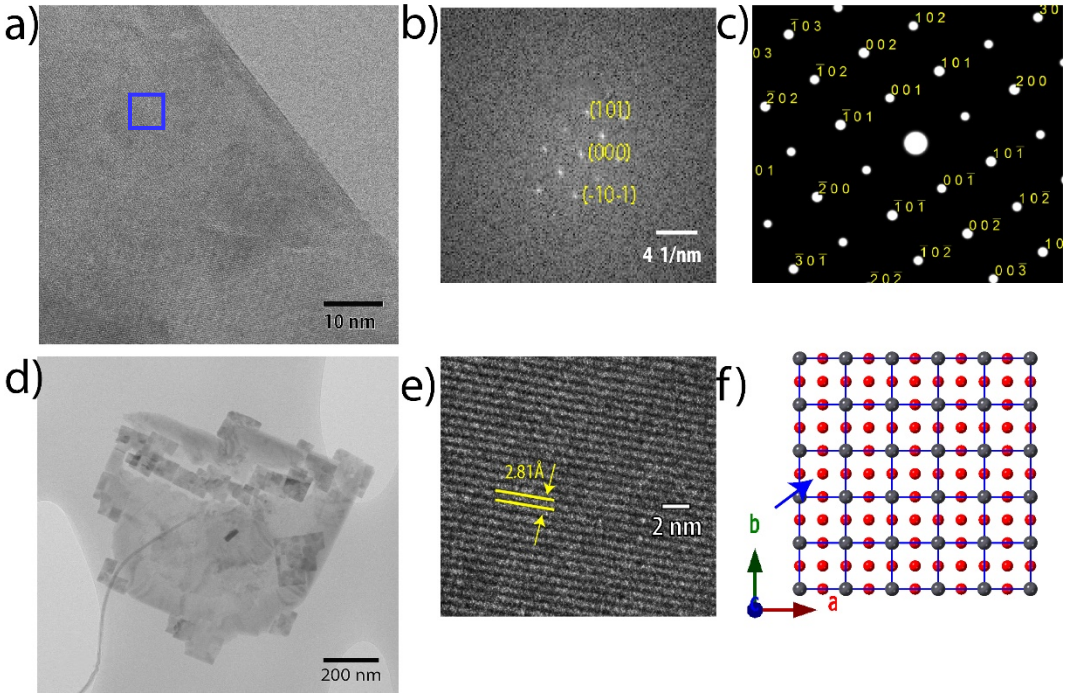

Figure 2.18. a) HRTEM of a single $PbTiO_3$ nanosheet, b) FFT of the boxed area in panel a, and c) corresponding calculated electron diffraction pattern, d) HRTEM image of full nanosheet e)*d*-spacing analysis (from same boxed area in panel a), and f) crystallographic view of the (101) plane for tetragonal $PbTiO_3$ (ICDD# 01-070-7729).

Interestingly, the nanosheets started to break upon irradiation with the 300kV electron beam of the TEM instrument, and we observed the formation of new nanoparticles at the edges of the nanosheets (**Figure 2.19a**). After some time, these nanoparticles also were observed on the surfaces of the nanosheets, and they began to migrate and combine with each other under the beam, creating bigger nanoparticles. This beam sensitivity was not completely surprising because this is a common characteristic of lead-containing materials; examples in the literature include $CsPbBr_3$,[53] $MaPbI_3$,[54] and $CsPbX_3$ nanocrystals.[55] However, the $PbTiO_3$ nanosheets maintained their morphology long enough for us to collect high quality images.

In one of the more in-depth studies performed on $PbTiO_3$ stability under an electron beam, Ma and coworkers describe the formation of Pb nanoparticles from $PbTiO_3$ nanocrystals .[56] In this study, the nanocrystals started to break under a 300 kV electron beam and generate Pb nanoparticles in just 20 seconds. This work shows that oxygen initially volatilizes from the $PbTiO_3$, aided by the reduced pressure in the microscope column. This creates a non-stoichiometric $PbTiO_3$ with general formula $Pb_{1-x}TiO_{3-y}$, which further degrades into nanoparticles of Pb at the edges of the material, leaving the nanocrystals with an $xPb–Pb_{1-x}TiO_{3-y}$ composition.[56] We confirmed by *d*-spacing analysis that the nanoparticles formed from our $PbTiO_3$ nanosheets matched hexagonal Pb (ICDD #00-023-0345), which is the expected allotrope. Furthermore, we observed smaller Pb nanoparticles aggregating into larger Pb nanoparticles (**Figure 2.19b)** in real time. The time it took for this process to occur under the beam was approximately 1 minute.

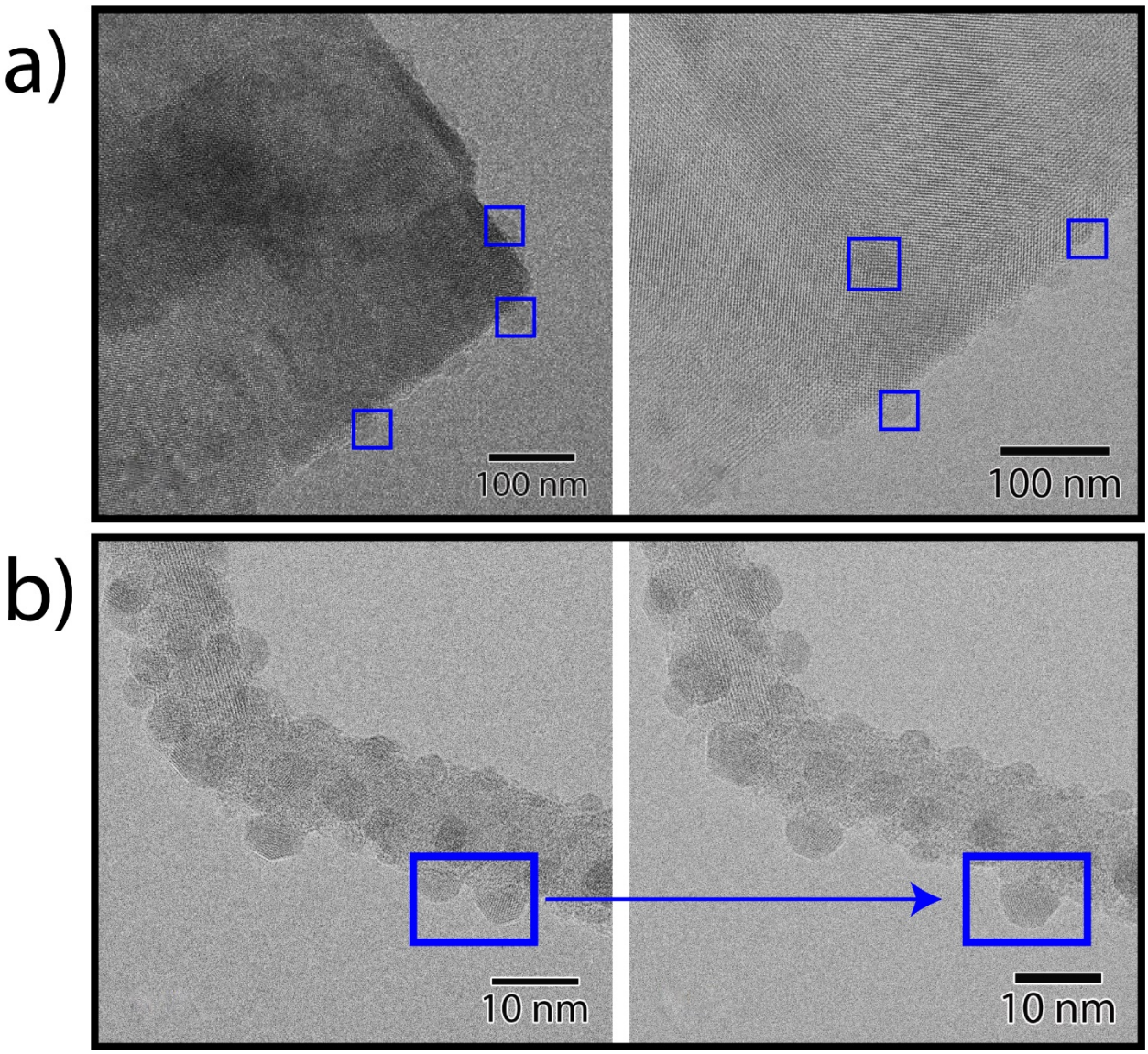

Figure 2.19. a) $PbTiO_3$ nanosheets exhibiting electron beam-induced degradation, followed by b) nanoparticles of Pb aggregating under the electron beam

The other product studied by HRTEM was the material formed after a 2-week-long reaction, conducted to determine the identity of these nanoparticles. Once they were exposed to the 300kV beam, they started to break, but this time we observed a rapid change from amorphous to crystalline (**Figure 2.20a**). Even though FFT measurements (**Figure 2.20b**) were consistent with the (010) plane of tetragonal $PbTiO_3$, the *d*-spacing (**Figure 2.20c**) of 3.98 Å was significantly different from the 2.838 Å typical for tetragonal $PbTiO_3$. Based on these results, we were not able to reliably match the nanoparticles to a $PbTiO_3$ structure. In the near future, low kV (30kV) studies will allow the characterization of such beam-sensitive materials while avoiding degradation.

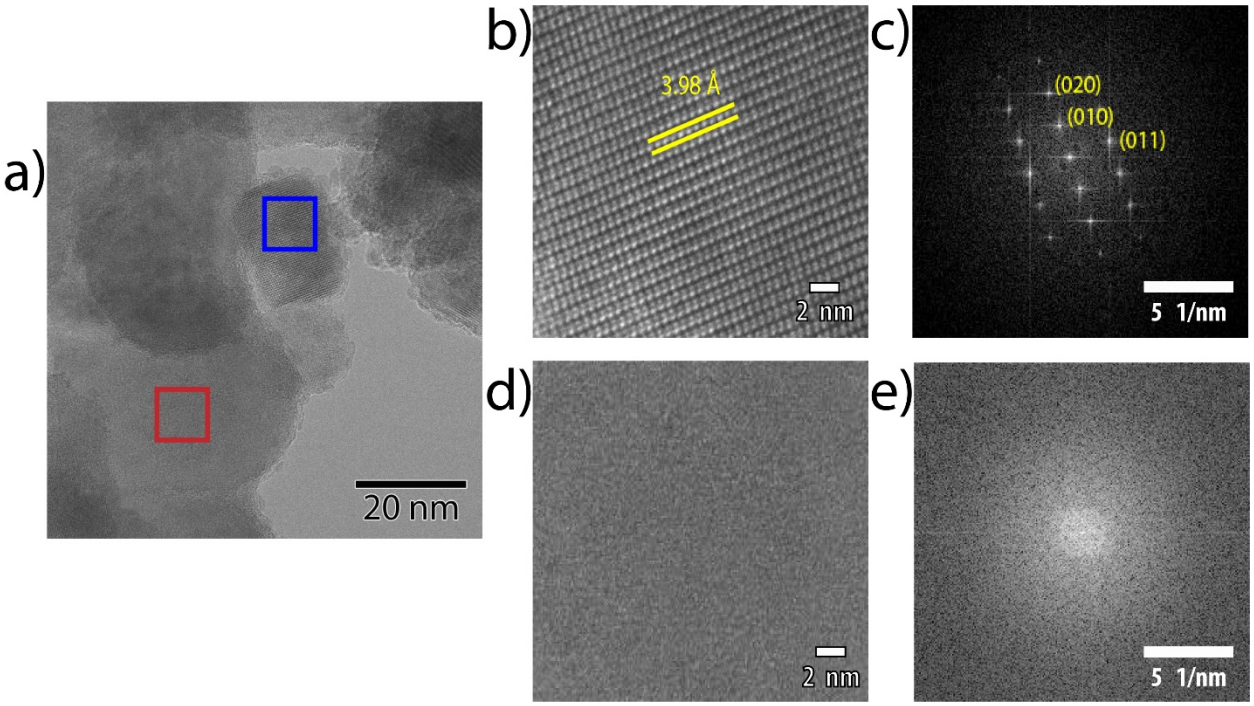

Figure 2.20. a) HRTEM of a single, $PbTiO_3$ nanosheet, b) d-spacing analysis and c) FFT of the boxed blue area in panel a, and d) d-spacing analysis and e) FFT of the boxed red area in panel a.

Reactions using different titania precursors

Further experiments examined the effects of different titania precursors on the formation of $PbTiO_3$ nanosheets. For example, the anatase polymorph of TiO_2 was reacted with α-PbO under the same conditions described in the $PbTiO_3$ synthesis (5 day reaction time). No $PbTiO_3$ nanosheets were observed; instead, TEM and PXRD revealed amorphous aggregates (**Figure 2.21**). However, it is worth mentioning that the anatase used in these reactions was not nanostructured, which is an important factor influencing its reactivity.

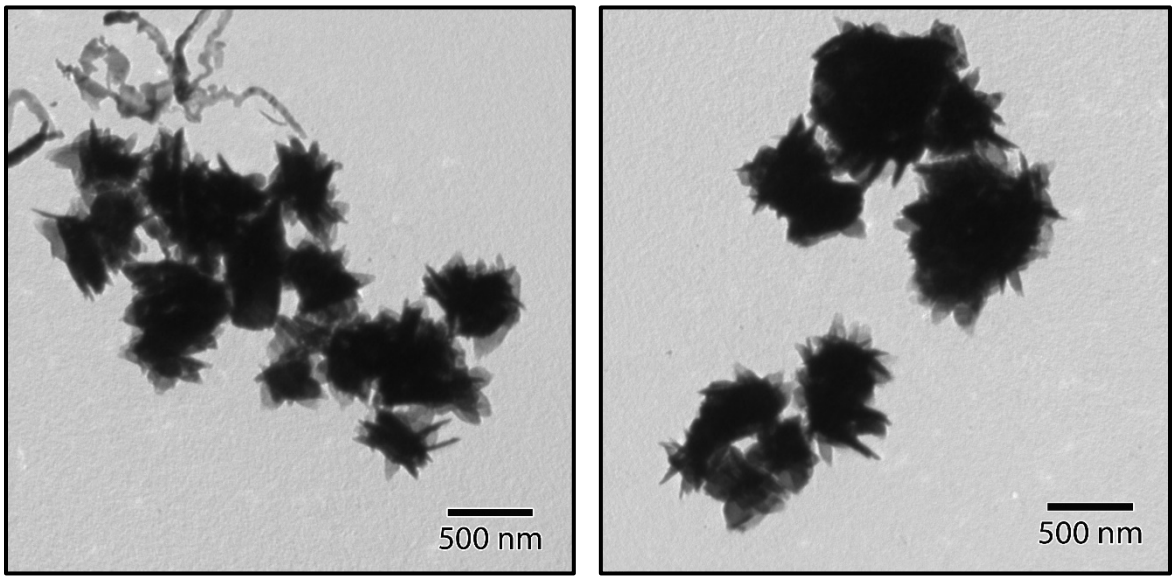

Figure 2.21. TEM images of products formed from reactions of anatase with α-PbO.

Another precursor was $(TBA)_2Ti_4O_9$ nanosheets, which are closely related to the $(TBA)_{1.07}Ti_{1.73}O_4$ nanosheets used in this work.[57] Following the already established principle that TBA^+ capped nanosheets insufficiently reactive, the $(TBA)_2Ti_4O_9$ was treated with aqueous $Pb(NO_3)_2$ to exchange the TBA^+ cation with Pb^{2+}. These Pb_x–Ti_4O_9 nanosheets were used in a reaction with a-PbO in a 1:1.67 ratio, which resulted in irregular and/or broken $PbTiO_3$ nanosheets (**Figure 2.22a**) and plumbonacrite (**Figure 2.22b** inside blue circle). More studies using Pb_x–Ti_4O_9 are needed to optimize conditions that yield better results.

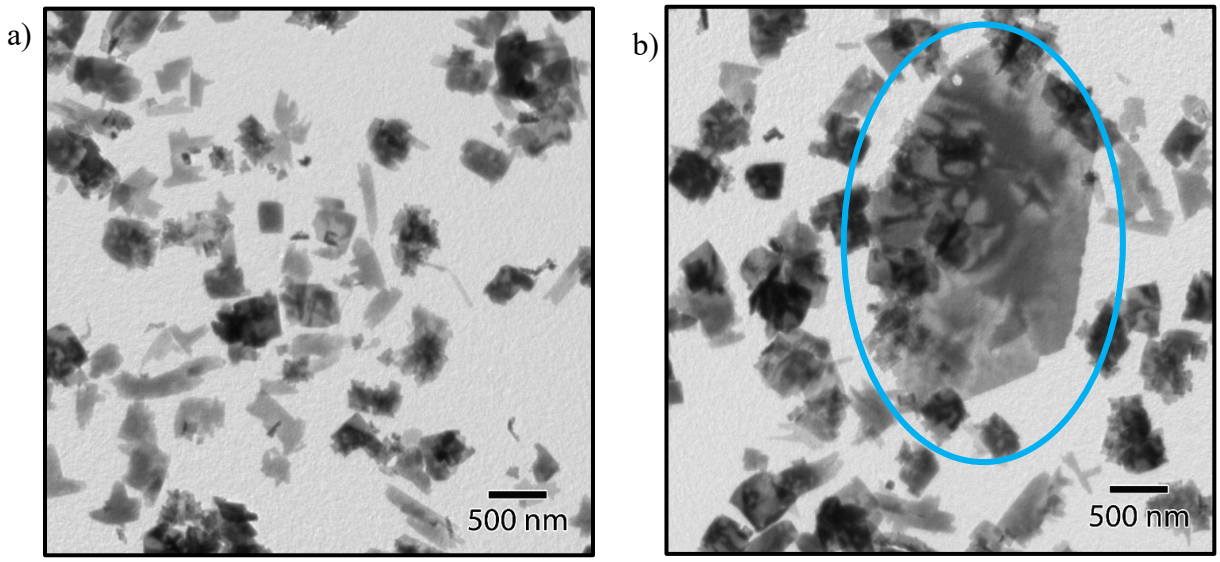

Figure 2.22. STEM images of products formed from reactions of Pb_x–Ti_4O_9 with α-PbO, plumbonacrite highlighted in the blue circle.

The PXRD pattern of the product from this α-PbO and Pb_x–Ti_4O_9 reaction (**Figure 2.23a**) reveals highly-oriented plumbonacrite. The peak that shows the strongest effect occurs at 41.86 2θ which correspond to the (2 2 3) plane (**Figure 2.23a**). This plane exhibits the hexagonal symmetry of plumbonacrite's crystal structure, which can be related to its preferred hexagonal nanosheet/platelet growth morphology. Because of this effect, the intensity of peaks for any other product are too low to detect.

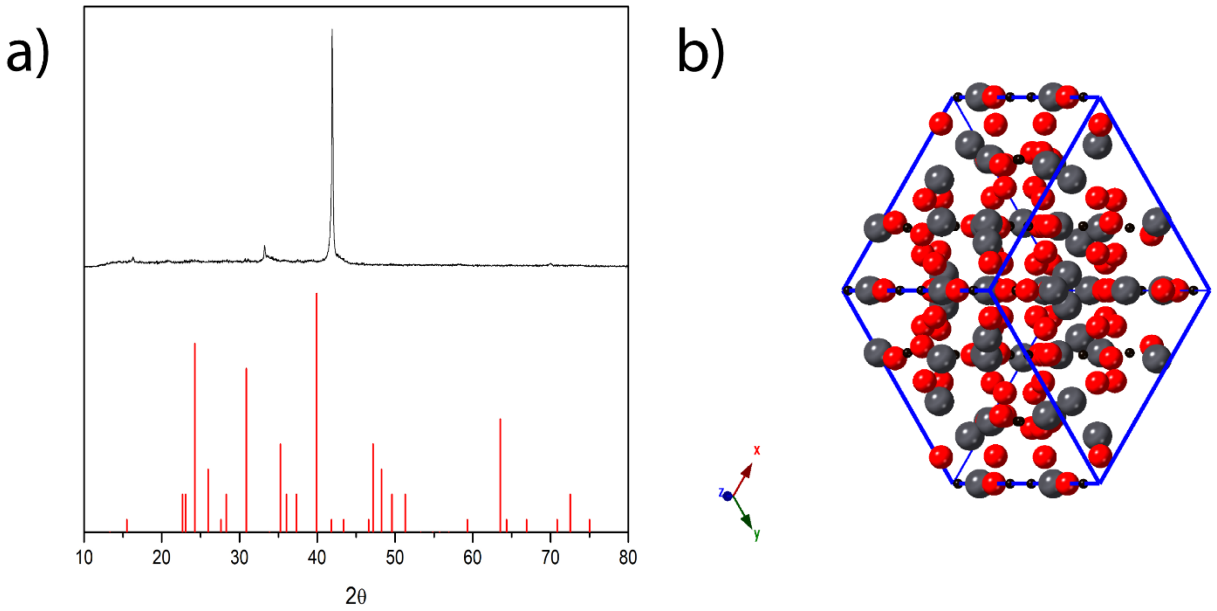

Figure 2.23. a) PXRD of the reaction between Pb_x–Ti_4O_9 and α-PbO and b) structural view of the (2 2 3) plane of plumbonacrite.

Conclusions

For the formation of $PbTiO_3$ nanosheets, the precursors as well as the reaction conditions are extremely important. Because lead preferentially forms basic lead carbonates when in excess, the amount of lead used in the reaction is especially crucial. When in excess, plumbonacrite forms; on the other hand, when not enough lead is present, $PbTiO_3$ nanosheets do not form. The best ratio found during these studies was 1:1.67 Pb_x–TiO_2:PbO. Other sources of lead ($PbCl_2$) showed no reactivity with the nanosheet precursor, leaving α-PbO as the best option.

The precursor used for the templated growth of $PbTiO_3$ nanosheets was another important factor. Anatase did not show any reactivity whereas Pb_x–Ti_4O_9 needs further work to perhaps yield nanosheets of the same size and morphology as Pb_x–TiO_2 while generating no plumbonacrite. The best precursor in this study was $(TBA)_{1.07}Ti_{1.73}O_4$ exchange of TBA^+ for Pb^{2+}.

Once the precursors were selected, the next milestone was preventing plumbonacrite formation, because the reaction of CO_2 with α-PbO to form plumbonacrite readily occurs in aqueous solutions.[58] The first step taken to achieve this was to lower the pH of the solution below the preferred pH for the formation of plumbonacrite (>7.4). Studies indicated that, when the pH was <6.0, the PbO reacted with the acid to form $PbCl_2$ which prevented $PbTiO_3$ formation. Only a pH between 6.0 and 6.8 yielded $PbTiO_3$ nanosheets without plumbonacrite. These nanosheets were characterized by PXRD, HRTEM, and STEM, which proved that their structure is that of tetragonal $PbTiO_3$.

Another set of conditions used in this study N_2 vs. atmospheric reactions. To achieve this, a wetbox allowed us to perform hydrothermal reactions under an inert atmosphere. These results allowed us to determine the correct amount of α-PbO necessary to produce $PbTiO_3$ without plumbonacrite. The reactions yielded nanosheets of $PbTiO_3$, but the hardship of maintaining a wetbox for this chemistry led us to change direction.

Once all the conditions were studied, the correct ratio of PbO to Pb_xTiO_2 was found, and the understanding of the formation and necessity of plumbonacrite was understood, the synthetic method for the creation of $PbTiO_3$ nanosheets was optimized. In short, $PbTiO_3$ nanosheets can be prepared successfully under three sets of conditions (low pH, N_2 atmosphere, and atmospheric conditions). The best products were characterized by PXRD, HRTEM, and STEM, which proved that their structure is that of the ferroelectric tetragonal $PbTiO_3$. The next step of this research was to test the chemistry and properties of $PbTiO_3$ nanosheets as well as the HRTEM of the starting materials to understand the exchange of TBA^+ and Pb^{2+}.

References

1. Piskunov, S.; Heifets, E.; Eglitis, R.; Borstel, G., Bulk properties and electronic structure of $SrTiO_3$, $BaTiO_3$, $PbTiO_3$ perovskites: an ab initio HF/DFT study. *Computational Materials Science* **2004,** *29* (2), 165-178.

2. Iijima, K.; Tomita, Y.; Takayama, R.; Ueda, I., Preparation of c-axis oriented $PbTiO_3$ thin films and their crystallographic, dielectric, and pyroelectric properties. *Journal of applied physics* **1986,** *60* (1), 361-367.

3. Chen, W.; Zheng, Y.; Xiong, W.; Feng, X.; Wang, B.; Wang, Y., Effect of mechanical loads on stability of nanodomains in ferroelectric ultrathin films: Towards flexible erasing of the non-volatile memories. *Scientific reports* **2014,** *4*, 5339.

4. Umeno, Y.; Albina, J. M.; Meyer, B.; Elsässer, C., Ab initio calculations of ferroelectric instability in $PbTiO_3$ capacitors with symmetric and asymmetric electrode layers. *Physical Review B* **2009,** *80* (20), 205122.

5. Chaudhari, V. A.; Bichile, G. K., Synthesis, structural, and electrical properties of pure PbTiO3 ferroelectric ceramics. *Smart Materials Research* **2013,** *2013*.

6. Okuyama, M.; Matsui, Y.; Nakano, H.; Hamakawa, Y., PbTiO3 ferroelectric thin film gate fet for infrared detection. *Ferroelectrics* **1981,** *33* (1), 235-241.

7. Bhatti, H. S.; Hussain, S. T.; Khan, F. A.; Hussain, S., Synthesis and induced multiferroicity of perovskite $PbTiO_3$; a review. *Applied Surface Science* **2016,** *367*, 291-306.

8. Buscaglia, V.; Buscaglia, M. T., Synthesis and properties of ferroelectric nanotubes and nanowires: a review. *Nanoscale Ferroelectrics and Multiferroics: Key Processing and Characterization Issues, and Nanoscale Effects, ed. M. Alguerό, JM Gregg and L. Mitoseriu, John Wiley & Sons* **2016**.

9. Tanaka, T.; Ebina, Y.; Takada, K.; Kurashima, K.; Sasaki, T., Oversized titania nanosheet crystallites derived from flux-grown layered titanate single crystals. *Chemistry of materials* **2003,** *15* (18), 3564-3568.

10. Banait, J.; Sidhu, K.; Walia, J., Transference numbers and solvation studies in n-butanol. *Canadian journal of chemistry* **1984,** *62* (2), 303-305.

11. Ozawa, T. C.; Onoda, M.; Iyi, N.; Ebina, Y.; Sasaki, T., Bulk Functional Materials Design Using Oxide Nanosheets as Building Blocks: A New Upconversion Material Fabricated by Flocculation of $Ca_2Nb_3O_{10}$–Nanosheets with Rare-Earth Ions. *The Journal of Physical Chemistry C* **2014,** *118* (3), 1729-1738.

12. Sinha, A. K.; Pradhan, M.; Pal, T., Morphological evolution of two-dimensional MnO_2 nanosheets and their shape transformation to one-dimensional ultralong MnO_2 nanowires for robust catalytic activity. *The Journal of Physical Chemistry C* **2013,** *117* (45), 23976-23986.

13. Li, L.; Ma, R.; Ebina, Y.; Fukuda, K.; Takada, K.; Sasaki, T., Layer-by-layer assembly and spontaneous flocculation of oppositely charged oxide and hydroxide nanosheets into inorganic sandwich layered materials. *Journal of the American Chemical Society* **2007,** *129* (25), 8000-8007.

14. Ma, R.; Sasaki, T., Synthesis of LDH nanosheets and their layer-by-layer assembly. *Recent patents on nanotechnology* **2012,** *6* (3), 159-168.

15. Jia, Y.; Zhao, S.; Song, Y.-F., The application of spontaneous flocculation for the preparation of lanthanide-containing polyoxometalates intercalated layered double hydroxides: highly efficient heterogeneous catalysts for cyanosilylation. *Applied Catalysis A: General* **2014,** *487*, 172-180.

16. Ma, J.; Liu, L.; Li, S.; Chen, Y.; Zhuo, M.; Shao, F.; Gong, J.; Tong, Z., Facile assembly for fast construction of intercalation hybrids of layered double hydroxides with anionic metalloporphyrin. *Dalton transactions* **2014,** *43* (26), 9909-9915.

17. Ma, R.; Sasaki, T., Conversion of metal oxide nanosheets into nanotubes. In *Inorganic and Metallic Nanotubular Materials*, Springer: 2010; pp 135-146.

18. Ma, R.; Bando, Y.; Sasaki, T., Directly rolling nanosheets into nanotubes. *The Journal of Physical Chemistry B* **2004,** *108* (7), 2115-2119.

19. Akçay, M., Characterization and adsorption properties of tetrabutylammonium montmorillonite (TBAM) clay: thermodynamic and kinetic calculations. *Journal of colloid and interface science* **2006,** *296* (1), 16-21.

20. Sirisaksoontorn, W.; Adenuga, A. A.; Remcho, V. T.; Lerner, M. M., Preparation and characterization of a tetrabutylammonium graphite intercalation compound. *Journal of the American Chemical Society* **2011,** *133* (32), 12436-12438.

21. Sasaki, T.; Watanabe, M.; Michiue, Y.; Komatsu, Y.; Izumi, F.; Takenouchi, S., Preparation and acid-base properties of a protonated titanate with the lepidocrocite-like layer structure. *Chemistry of materials* **1995,** *7* (5), 1001-1007.

22. Kim, T. W.; Ha, H.-W.; Paek, M.-J.; Hyun, S.-H.; Choy, J.-H.; Hwang, S.-J., Unique phase transformation behavior and visible light photocatalytic activity of titanium oxide hybridized with copper oxide. *Journal of Materials Chemistry* **2010,** *20* (16), 3238-3245.

23. Paek, M.-J.; Ha, H.-W.; Kim, T. W.; Moon, S.-J.; Baeg, J.-O.; Choy, J.-H.; Hwang, S.-J., Formation efficiency of one-dimensional nanostructured titanium oxide affected by the structure and composition of titanate precursor: a mechanism study. *The Journal of Physical Chemistry C* **2008,** *112* (41), 15966-15972.

24. Kim, T. W.; Hur, S. G.; Hwang, S.-J.; Choy, J.-H., Layered titanate–zinc oxide nanohybrids with mesoporosity. *Chemical communications* **2006,** (2), 220-222.

25. Kim, T. W.; Hwang, S.-J.; Park, Y.; Choi, W.; Choy, J.-H., Chemical bonding character and physicochemical properties of mesoporous zinc oxide-layered titanate nanocomposites. *The Journal of Physical Chemistry C* **2007,** *111* (4), 1658-1664.

26. Suzuki, S.; Miyayama, M., Lithium intercalation properties of octatitanate synthesized through exfoliation/reassembly. *The Journal of Physical Chemistry B* **2006,** *110* (10), 4731-4734.

27. Wang, L.; Sasaki, T., Titanium oxide nanosheets: graphene analogues with versatile functionalities. *Chemical reviews* **2014,** *114* (19), 9455-9486.

28. Shi, L.; Xu, Y.; Li, Q., Controlled growth of lead oxide nanosheets, scrolled nanotubes, and nanorods. *Crystal Growth and Design* **2008,** *8* (10), 3521-3525.

29. Yousefi, R.; Sheini, F. J.; SA, A.; Cheraghizade, M., Growth and characterization of PbO nanorods grown using facile oxidation of lead sheet. *Sains Malaysiana* **2015,** *44* (2), 291-294.

30. Cao, M.; Hu, C.; Peng, G.; Qi, Y.; Wang, E., Selected-control synthesis of PbO_2 and Pb_3O_4 single-crystalline nanorods. *Journal of the American Chemical Society* **2003,** *125* (17), 4982-4983.

31. Xia, Y.; Yang, Z.; Mokaya, R., Mesostructured hollow spheres of graphitic N-doped carbon nanocast from spherical mesoporous silica. *The Journal of Physical Chemistry B* **2004,** *108* (50), 19293-19298.

32. Wu, M.; Wang, G.; Xu, H.; Long, J.; Shek, F. L.; Lo, S. M.-F.; Williams, I. D.; Feng, S.; Xu, R., Hollow spheres based on mesostructured lead titanate with amorphous framework. *Langmuir* **2003,** *19* (4), 1362-1367.

33. Wang, G.; Sæterli, R.; Rørvik, P. M.; van Helvoort, A. T.; Holmestad, R.; Grande, T.; Einarsrud, M.-A., Self-assembled growth of $PbTiO_3$ nanoparticles into microspheres and bur-like structures. *Chemistry of materials* **2007,** *19* (9), 2213-2221.

34. Ji, Q.; Miyahara, M.; Hill, J. P.; Acharya, S.; Vinu, A.; Yoon, S. B.; Yu, J.-S.; Sakamoto, K.; Ariga, K., Stimuli-free auto-modulated material release from mesoporous nanocompartment films. *Journal of the American Chemical Society* **2008,** *130* (8), 2376-2377.

35. Yang, Z.; Xia, Y.; Mokaya, R., Hollow shells of high surface area graphitic N-doped carbon composites nanocast using zeolite templates. *Microporous and mesoporous materials* **2005,** *86* (1-3), 69-80.

36. Liu, Y.-f.; Lu, Y.-n.; Dai, S.-h.; Shi, S.-z., Synthesis and growth mechanism of donut-like lead titanate particles by hydrothermal method. *Powder technology* **2010,** *198* (1), 1-5.

37. Wang, G.; Liu, Y.; Ye, J.; Qiu, W., Synthesis, microstructural characterization, and electrochemical performance of novel rod-like Ti_4O_7 powders. *Journal of Alloys and Compounds* **2017,** *704*, 18-25.

38. Portehault, D.; Maneeratana, V.; Candolfi, C.; Oeschler, N.; Veremchuk, I.; Grin, Y.; Sanchez, C.; Antonietti, M., Facile general route toward tunable magnéli nanostructures and their use as thermoelectric metal oxide/carbon nanocomposites. *ACS nano* **2011,** *5* (11), 9052-9061.

39. Fukushima, J.; Takizawa, H., Size Control of Ti_4O_7 Nanoparticles by Carbothermal Reduction Using a Multimode Microwave Furnace. *Crystals* **2018,** *8* (12), 444.

40. Takeuchi, T.; Fukushima, J.; Hayashi, Y.; Takizawa, H., Synthesis of Ti_4O_7 nanoparticles by carbothermal reduction using microwave rapid heating. *Catalysts* **2017,** *7* (2), 65.

41. Maragatha, J.; Rani, C.; Rajendran, S.; Karuppuchamy, S., Microwave synthesis of nitrogen doped Ti_4O_7 for photocatalytic applications. *Physica E: Low-dimensional Systems and Nanostructures* **2017,** *93*, 78-82.

42. Conze, S.; Veremchuk, I.; Reibold, M.; Matthey, B.; Michaelis, A.; Grin, Y.; Kinski, I., Magnéli phases Ti_4O_7 and Ti_8O_{15} and their carbon nanocomposites via the thermal decomposition-precursor route. *Journal of Solid State Chemistry* **2015,** *229*, 235-242.

43. Gusev, A.; Avvakumov, E.; Vinokurova, O., Synthesis of Ti_4O_7 magneli phase using mechanical activation. *Science of Sintering* **2003,** *35* (3), 141-145.

44. Nalwa, H. S., *Handbook of low and high dielectric constant materials and their applications, two-volume set*. Elsevier: 1999.

45. Zhao, R.; Li, M.; Ren, Z.; Zhu, Y.; Han, G., Three-dimensional oriented attachment growth of single-crystal pre-perovskite $PbTiO_3$ hollowed fibers. *CrystEngComm* **2018,** *20* (4), 448-453.

46. Li, M.; Kong, F.; Wang, H.; Li, G., Synthesis of vanadium pentoxide (V_2O_5) ultralong nanobelts via an oriented attachment growth mechanism. *CrystEngComm* **2011,** *13* (17), 5317-5320.

47. Yasui, K.; Kato, K., Dipole–dipole interaction model for oriented attachment of $BaTiO_3$ nanocrystals: a route to mesocrystal formation. *The Journal of Physical Chemistry C* **2012,** *116* (1), 319-324.

48. Yasui, K.; Kato, K., Oriented attachment of cubic or spherical $BaTiO_3$ nanocrystals by van der Waals torque. *The Journal of Physical Chemistry C* **2015,** *119* (43), 24597-24605.

49. Wang, Z.; Schliehe, C.; Wang, T.; Nagaoka, Y.; Cao, Y. C.; Bassett, W. A.; Wu, H.; Fan, H.; Weller, H., Deviatoric stress driven formation of large single-crystal PbS nanosheet from

nanoparticles and in situ monitoring of oriented attachment. *Journal of the American Chemical Society* **2011,** *133* (37), 14484-14487.

50. Chen, X.; Zhou, Y.; Liu, Q.; Li, Z.; Liu, J.; Zou, Z., Ultrathin, single-crystal WO_3 nanosheets by two-dimensional oriented attachment toward enhanced photocatalystic reduction of CO_2 into hydrocarbon fuels under visible light. *ACS applied materials & interfaces* **2012,** *4* (7), 3372-3377.

51. Wang, C.; Du, G.; Ståhl, K.; Huang, H.; Zhong, Y.; Jiang, J., Ultrathin SnO_2 nanosheets: oriented attachment mechanism, nonstoichiometric defects, and enhanced lithium-ion battery performances. *The Journal of Physical Chemistry C* **2012,** *116* (6), 4000-4011.

52. Zhang, L.; Chen, J.; Fan, L.; Diéguez, O.; Cao, J.; Pan, Z.; Wang, Y.; Wang, J.; Kim, M.; Deng, S., Giant polarization in super-tetragonal thin films through interphase strain. *Science* **2018,** *361* (6401), 494-497.

53. Dang, Z.; Shamsi, J.; Akkerman, Q. A.; Imran, M.; Bertoni, G.; Brescia, R.; Manna, L., Low-temperature electron beam-induced transformations of cesium lead halide perovskite nanocrystals. *ACS omega* **2017,** *2* (9), 5660-5665.

54. Xiao, C.; Li, Z.; Guthrey, H.; Moseley, J.; Yang, Y.; Wozny, S.; Moutinho, H.; To, B.; Berry, J. J.; Gorman, B., Mechanisms of electron-beam-induced damage in perovskite thin films revealed by cathodoluminescence spectroscopy. *The Journal of Physical Chemistry C* **2015,** *119* (48), 26904-26911.

55. Dang, Z.; Shamsi, J.; Palazon, F.; Imran, M.; Akkerman, Q. A.; Park, S.; Bertoni, G.; Prato, M.; Brescia, R.; Manna, L., In situ transmission electron microscopy study of electron beam-induced transformations in colloidal cesium lead halide perovskite nanocrystals. *Acs Nano* **2017,** *11* (2), 2124-2132.

56. Suriyaprakash, J.; Xu, Y.; Zhu, Y.; Yang, L.; Tang, Y.; Wang, Y.; Li, S.; Ma, X., Designing of metallic nanocrystals embedded in non-stoichiometric perovskite nanomaterial and its surface-electronic characteristics. *Scientific reports* **2017,** *7* (1), 8343.

57. Allen, M. R.; Thibert, A.; Sabio, E. M.; Browning, N. D.; Larsen, D. S.; Osterloh, F. E., Evolution of physical and photocatalytic properties in the layered titanates $A_2Ti_4O_9$ (A= K, H) and in nanosheets derived by chemical exfoliation. *Chemistry of Materials* **2010,** *22* (3), 1220-1228.

58. Vanmeert, F.; Van der Snickt, G.; Janssens, K., Plumbonacrite identified by X-ray powder diffraction tomography as a missing link during degradation of red lead in a Van Gogh painting. *Angewandte Chemie* **2015,** *127* (12), 3678-3681.

Supporting information

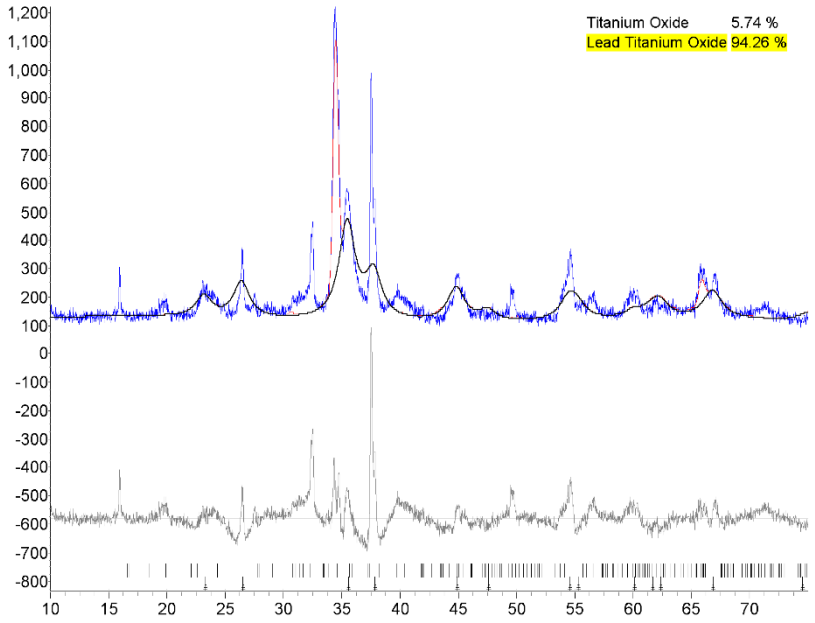

Figure S2.1. Rietveld refinement of the isolated product from the hydrothermal reaction of Pb_x–TiO_2 and α-PbO at pH 6.88.

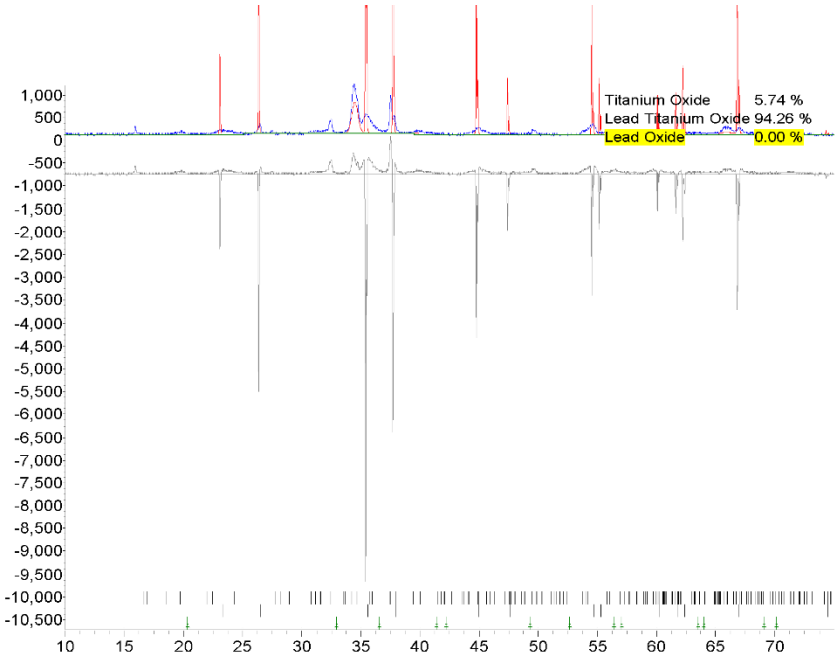

Figure S2.1. Rietveld refinement of the isolated product from the hydrothermal reaction of Pb_x–TiO_2 and α-PbO at pH 6.88.

CHAPTER III

TEMPLATED GROWTH OF BARIUM TITANATE NANOSHEETS

Introduction

Barium titanate ($BaTiO_3$) is a piezoelectric and ferroelectric material that also exhibits the photorefractive effect. The nanostructuring of $BaTiO_3$ is directly related to applications ranging from thermistors to capacitors. Here we describe freestanding nanosheets of $BaTiO_3$ synthesized by a low-temperature, templated-based method. The template is $(TBA)_{1.07}Ti_{1.73}O_4$, a well-known 2D-nanostructured analog of TiO_2(B), which is converted to a more reactive form, H_x-TiO_2, prior to reactions with $Ba(OH)_2 \bullet 8H_2O$. H_x-TiO_2 serve as a titanate precursor and morphology template whereas the barium salt is the barium source and reaction flux. The resulting nanosheets can be identified as tetragonal $BaTiO_3$. The optimization of $BaTiO_3$ nanosheet formation is discussed fully in this chapter.

Barium titanate is another very important member of the inorganic perovskite family. This material has been studied extensively as a less toxic counterpart to $PbTiO_3$. This material also possesses a lower transition temperature from its tetragonal to cubic structure (130 °C compared with $PbTiO_3$ that is 420°C),[1] a spontaneous polarization of 26 $\mu C/cm^2$,[2] and a dielectric constant of 5000.[3] Because of these properties, it has been used for applications including multilayer ceramic capacitors,[4] electro-optical devices,[5] and semiconductors.[6]

Unlike our $PbTiO_3$ nanosheet synthesis, which followed a hydrothermal approach, here to prepare $BaTiO_3$ nanosheets we avoid hydrothermal conditions because of unpredictable side products. Given these reasons, we decided to switch to a solid state reaction with the use of a flux material to aid in the formation of the nanosheets. In general, flux-based syntheses are used to prepare materials at lower temperatures than solid state reactions. The flux acts as a solvent by enhancing the diffusion of reactants.[7] Common flux materials include oxides,[8-9] sulfides,[10-12] chlorides,[13-15] and hydroxides.[16-20]

Therefore, we use melt fluxes based on barium-containing salts [$BaCl_2 \cdot 2H_2O$ and $Ba(OH)_2 \cdot 8H_2O$]. Nanosheets of TiO_2 were used again as templating agents, following our positive results in the $PbTiO_3$ system. $(TBA)_{1.07}Ti_{1.73}O_4$ nanosheets were employed for this purpose by exchanging the TBA^+ with H^+ to ensure reactivity with Ba^{2+}. Furthermore, the reactions were conducted in sealed Schlenk vessels to facilitate the melting of the hydrated salts $BaCl_2 \cdot 2H_2O$ and $Ba(OH)_2 \cdot 8H_2O$. This chapter examines these synthetic approaches to $BaTiO_3$ nanosheets as well as their characterization.

Experimental

Materials: Li_2CO_3 (Sigma-Aldrich Corp.), MoO_3 (Sigma-Aldrich Corp., 99.5%), K_2CO_3 (Sigma-Aldrich Corp.), Anatase (Sigma-Aldrich Corp., 99.8%), TBAOH (Sigma-Aldrich Corp., 1M HPLC), HCl (Sigma-Aldrich Corp., 37% w/v).

Preparation of the nanostructured cesium titanate precursor: This procedure followed the details published by Sasaki et al.,[21] where cesium titanate of composition $Cs_{0.7}Ti_{1.825}\square_{0.175}O_4$ (□ = vacancy) was synthesized by firing a finely ground mixture of 3.2582g Cs_2CO_3 and 4.2329g TiO_2 (1:5.3 in molar ratio) at 1173 K. The sample was calcined twice for a period of 24 h each time, with additional grinding (mortar & pestle) between calcinations. The resulting material was ground down once more before being dispersed in 1 M hydrochloric acid (150 mL g^{-1}) and shaken for 5 d with a linear shaker at 74 RPM. The acid was replaced each day (by centrifugation at 10,000 RPM on an allegra 64-R centrifuge. Following this acid leaching of Cs^+, the remaining solid was washed with copious amounts of deionized water to remove all acid residue and re-dispersed in 500 mL of 0.5M TBA(OH) solution. The resulting nanosheets were washed by centrifugation and re-dispersed in water before being used for the reactions after calculating the grams of material per mL of water.

Preparation of $BaTiO_3$ from the cesium titanate precursor: 0.1000 g of $Cs_{0.7}Ti_{1.825}\square_{0.175}O_4$ nanosheets (of the 1.25 mmol dispersion) were mixed with 3.000 g of $Ba(OH)_2 \bullet 8H_2O$ (0.025M) and transferred to a 18.6g platinum crucible. The mixture was then gently melted at 95 °C inside a furnace over a period of 2 h with periodic stirring with a Teflon™ stirring rod. Once melted, the homogenous mixture was transferred to a Teflon sleeve, sealed in a stainless steel autoclave, and quickly heated to 180 °C, which was maintained for 45 min. After cooling to room temperature, the sample was removed and washed with copious amounts of boiling water, followed by mild sonication for 1 h. The sample was then centrifuged for 10 min at 10,000 rpm on an Allegra 64-R centrifuge, after which the supernatant was discarded and the precipitate re-dispersed in fresh deionized water. The centrifugation step was repeated twice more before re-dispersing the solid in ~5 mL of water.

Preparation of H_x-TiO_2: 20.00 mL of $(TBA)_{1.07}Ti_{1.73}O_4$ (5.7 mg mL^{-1} dispersion in H_2O) were placed in a centrifuge tube. Upon addition of a suspension of 1 mL of 1M HCl, a white flocculate formed. This material was isolated by centrifuging for 15 min at 10,000 rpm on an Allegra 64-R centrifuge and then washing with 35 mL H_2O 2× to remove excess acid and TBA^+. After the material was freeze dried, it was stored, and the needed amounts were taken to use in subsequent reactions.

Reaction of H_x-TiO_2 with $BaCl_2$: 0.6116 g (5.0 mmol) of $BaCl_2 \bullet 2H_2O$ were added to a Schlenk tube containing 0.2000 g of the H_x-TiO_2 (2.5 mmol). The reaction was sealed in air, and the tube was half submerged in an oil bath. The reaction was heated up to 120 °C and left to react for 1 d. After the reaction was done, the solids were washed with 30 mL of water 4× to dissolve any remaining $BaCl_2 \bullet 2H_2O$. The resulting dispersion was centrifuged at 10,000 RPM on an Allegra

64-R centrifuge, after which the supernatant was decanted and the solid product freeze-dried (results in **Figure 3.4**).

Synthesis of $BaTiO_3$ nanosheets: 0.0761g (0.99 mmol) $Ba(OH)_2•8H_2O$ were added to a Schlenk storage tube with a high vacuum valve (Chemglass AF-0096 with Chem-Vac™ Chem-Cap™ valve) containing 0.0761 g of H_x-TiO_2 (0.95 mmol) and hand shaken. The reaction was sealed in air, and the tube was half submerged in an oil bath. The reaction was heated up to 120 °C and left to react for 1 d. After the reaction was done, the solid was washed with 30 mL of boiling water 4× to wash away any remaining $Ba(OH)_2•8H_2O$. The resulting dispersion was centrifuged at 10,000 RPM on an Allegra 64-R centrifuge, after which the supernatant was decanted and the solid product freeze-dried (67% isolated yield).

Characterization details

Powder X-ray diffraction (PXRD) data was collected on a Bruker D8 instrument utilizing a Co−Kα X-ray source (λ = 1.78890 Å) operated at 40 kV and 35 mA. Data was collected from 10° to 80° 2θ with a scan rate of 0.1 s/step. Samples were prepared as powder mounts or drop cast from solution.

Transmission electron microscopy (TEM) imaging and selected area electron diffraction (SAED) analyses were performed using a FEI Tecnai 20 transmission electron microscope with an accelerating voltage of 200 kV. High resolution transmission electron microscopy (HRTEM) was performed with a FEI Tecnai G2 F30 S-TWIN operating at 300 kV. Samples were drop cast onto Formvar, holey carbon, or lacey carbon grids and air-dried.

Scanning electron microscopy (SEM) and scanning transmission electron microscopy (STEM) analyses were performed using a FEI Teneo FE-SEM with an Oxford EDS system operated at 10-30 kV with a spot size of 10. Samples were drop cast onto silicon wafer or Formvar grids.

Results and Discussion

Re-Examination of Prior Experiments

The initial experiments on this project aimed to reproduce a synthesis of $BaTiO_3$ nanosheets by a former member of this lab, Dr. Chris Barrett. He used $Cs_xTi_{2-x/4}\square_{x/4}O_4$ (□ = vacancy) nanosheets reported by Sasaki, et al. as a precursor/template. [21] As seen by TEM imaging in **Figure 3.1**, these nanosheets can have a multilayer structure and lateral dimensions ranging from 1 to 2 μm.

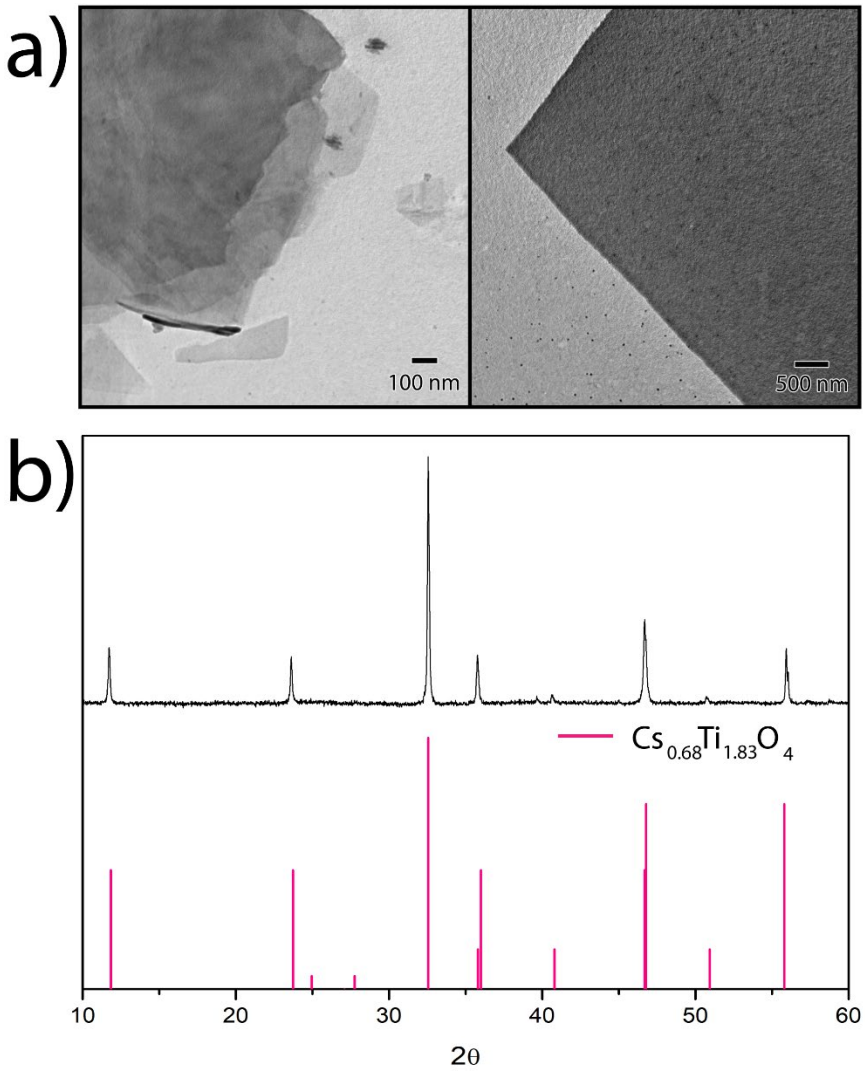

Figure 3.1. TEM of $Cs_{0.7}Ti_{1.825}\square_{0.175}O_4$ (□ = vacancy) nanosheets.

The reaction of $Cs_{0.7}Ti_{1.825}\square_{0.175}O_4$ nanosheets with $Ba(OH)_2 \bullet 8H_2O$, by the procedure detailed in his laboratory notebook entries for the preparation of $BaTiO_3$ nanosheets, yielded $BaTiO_3$ nanoparticles plus unidentified nanoribbons (**Figure 3.2**). PXRD of this product (**Figure 3.3**) shows the nanoparticles of $BaTiO_3$ (blue drop lines) and excess $Ba(OH)_2 \bullet 8H_2O$ (red lines). The broad peaks (highlighted with a star) are consistent with the small size of the nanoparticles. The presence of barium hydroxide can be explained by insufficient sample washing and its limited solubility in room temperature water.

$BaTiO_3$ nanoparticles have been synthesized by many different methods previously,[22-27] but they are not the focus of our research. Therefore, we decided to change the reaction precursors and conditions.

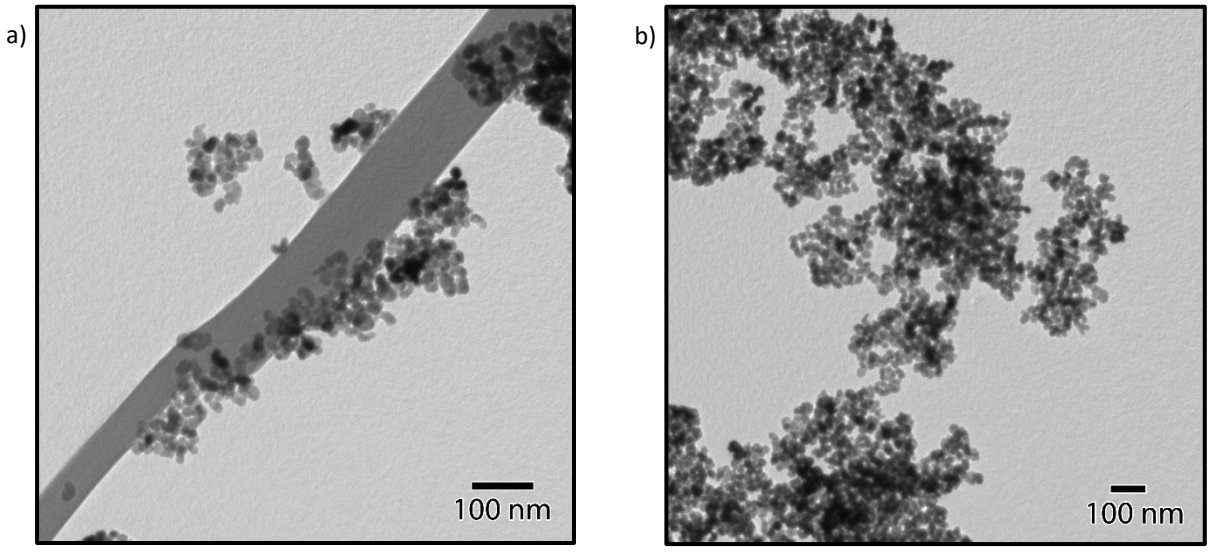

Figure 3.2. TEM of a) first and b) second attempt to reproduce a prior preparation of $BaTiO_3$ nanosheets.

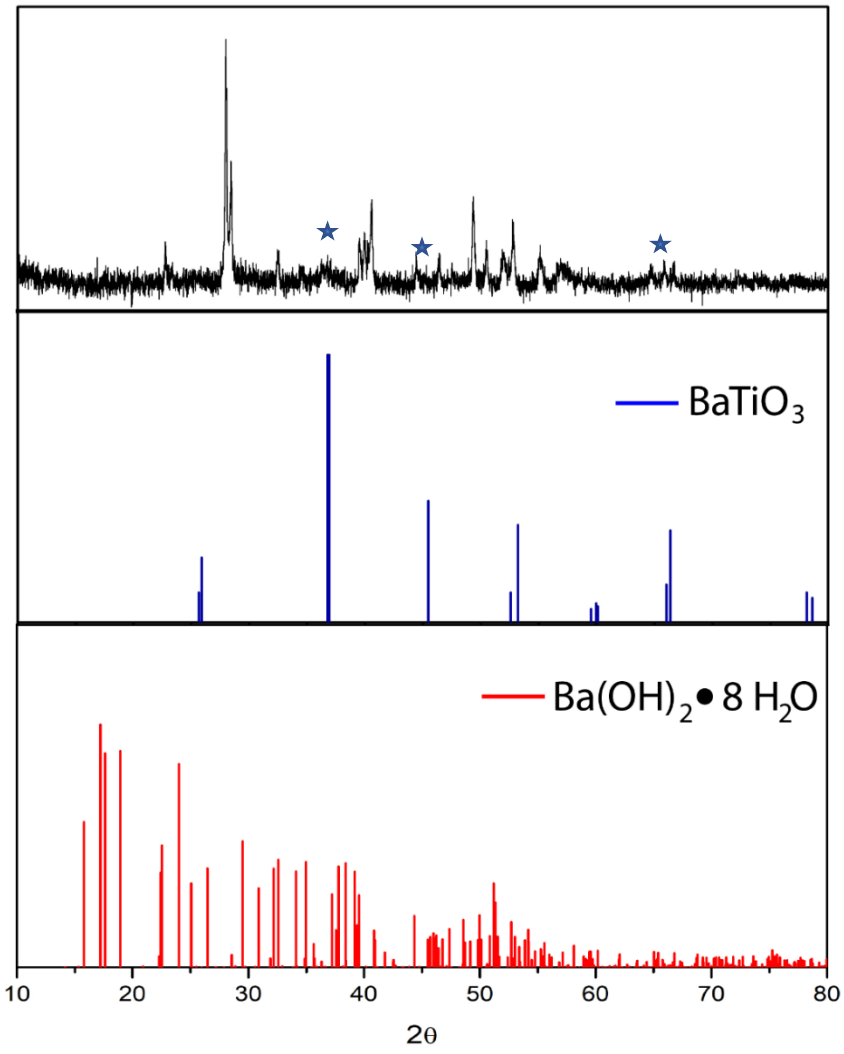

Fig 3.3. PXRD of the product from the reaction of $Cs_{0.7}Ti_{1.825}\square_{0.175}O_4$ and $Ba(OH)_2 \bullet 8H_2O$.

$BaTiO_3$ Nanosheets from $(TBA)_{1.07}Ti_{1.73}O_4$

Improved experiments employed a different titanate nanosheet template, $(TBA)_{1.07}Ti_{1.73}O_4$,[28] which was used successfully for the $PbTiO_3$ nanosheet synthesis described in Chapter II. **Figure 3.4** shows TEM images of these $(TBA)_{1.07}Ti_{1.73}O_4$ nanosheets; they are ~1.5 nm in thickness (Chapter II, **Figure**. 1) and approximately 500 nm to 2 μm in lateral dimensions.

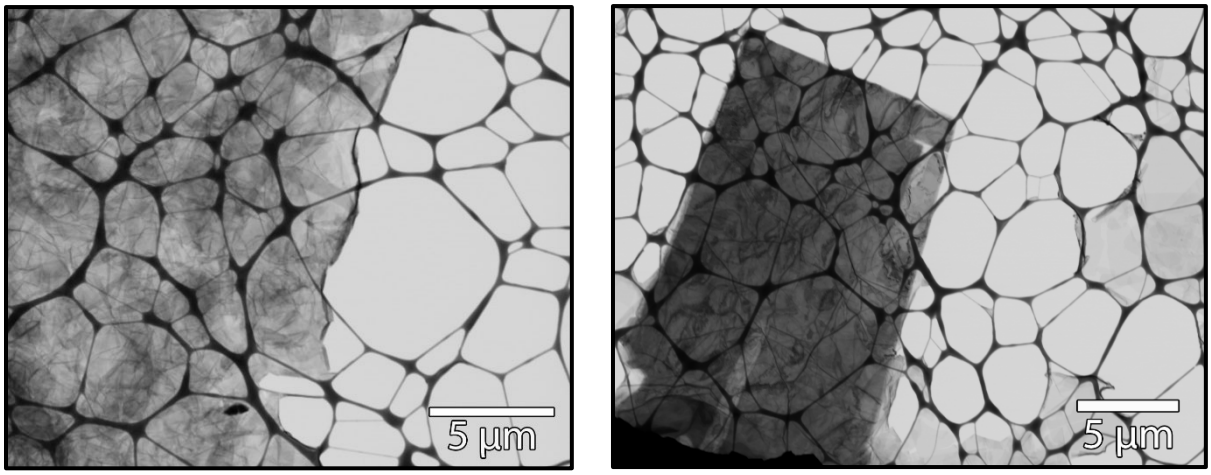

Figure 3.4. TEM of $(TBA)_{1.07}Ti_{1.73}O_4$ nanosheets used for the $BaTiO_3$ reactions.

For the $PbTiO_3$ reactions, the TBA on the $(TBA)_{1.07}Ti_{1.73}O_4$ nanosheets were exchanged for Pb^{2+} to make them sufficiently reactive. For $BaTiO_3$, we included this step, which also is consistent with Dr. Barrett's HCl treatment of $Cs_{0.7}Ti_{1.825}\square_{0.175}O_4$ nanosheets. Notably, the workup of the resulting H_x-TiO_2 nanosheets is especially important to ensure that all acid is removed; if it is not, the H_x-TiO_2 nanosheets turn off-white in color (yellow in extreme cases) due to chloride impurities, and it should not be used.

Once the dispersion of H_x-TiO_2 nanosheets reached a pH of ~7, we could be sure that all the acid was washed away. The nanosheets were then freeze-dried to preserve their morphology;

as noted in Chapter II, drying the nanosheets any other way leads to aggregation. PXRD of the nanosheets showed an amorphous pattern (**Figure 3.5**), similar to its counterpart Pb_x-TiO_2 discused in chapter II.

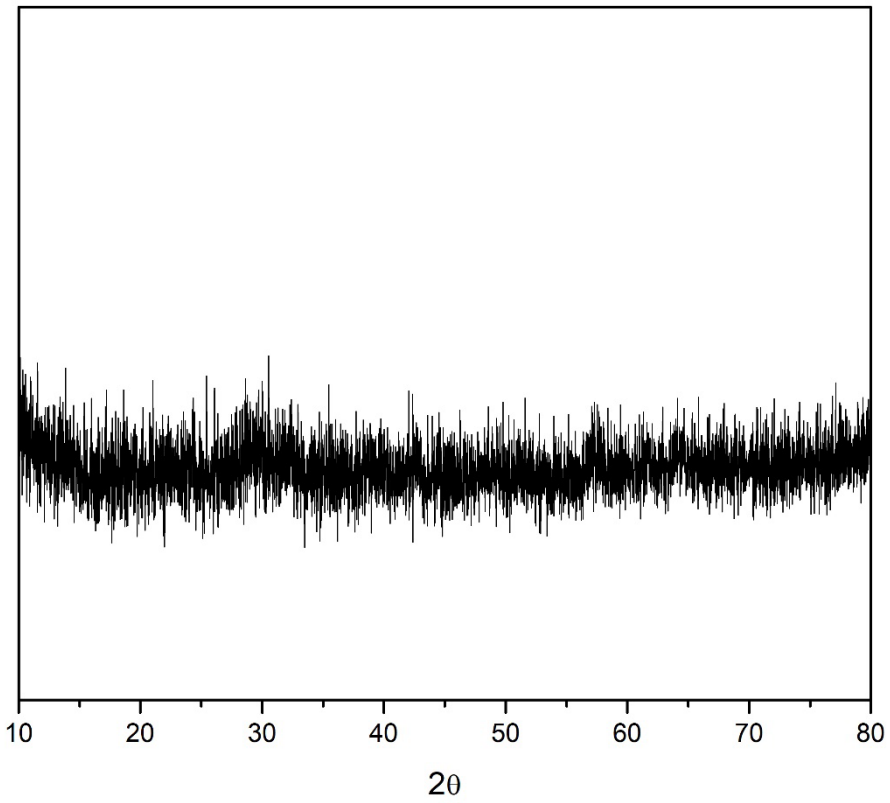

Figure 3.5. PXRD of freeze dried H_x-TiO_2.

In subsequent experiments with H_x-TiO_2, $BaCl_2$•$2H_2O$ served as the barium source and the flux. These solids were added in a 1:1 molar ratio to a Schlenk tube and sealed; this procedure allowed us to heat them in a closed environment to prevent the hydrate water from completely evaporating (to help with the flux formation and the melting of the salt), while also preventing atmospheric CO_2 from leading to undesired $BaCO_3$ formation (some carbon dioxide and atmospheric water is present in the solution).

The reaction was left to react for 1 to 3 d at 120 °C. After 2 h, condensation was observed on the sides of the vessel. After 1 d the nanosheets changed from white to an off-white color, and after 3 d they turned beige. Once this happened, the solid product was isolated and washed with boiling water multiple times to dissolve any remaining $BaCl_2$•$2H_2O$. By STEM imaging and EDS analysis, we observed broken nanosheets (**Figure 3.6a**) with Ba:Ti of 1:15, which suggested that Ba was not well incorporated into the product. We also observed aggregates of $BaCl_2$ (**Figure 3.6b**, blue circle), which could be removed with additional water washing of the solids.

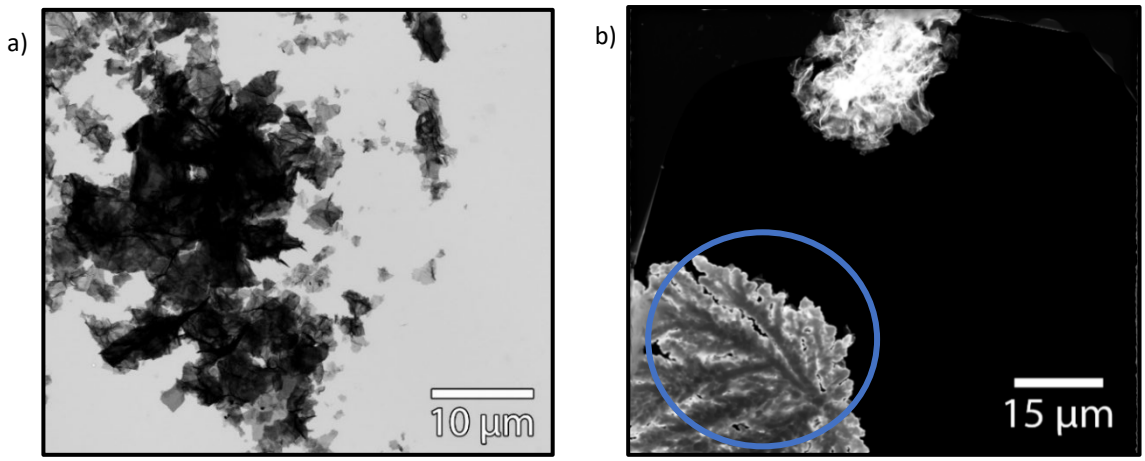

Figure 3.6. STEM analysis of the product from the reaction of H_x-TiO_2 and $BaCl_2$•$2H_2O$: a) nanosheets and b) $BaCl_2$ aggregates (blue circle).

After washing the product with water, PXRD revealed exclusively TiO_2(B) (ICDD# 00-049-1237), as seen in **Figure 3.7**, which confirmed that no $BaTiO_3$ was present.

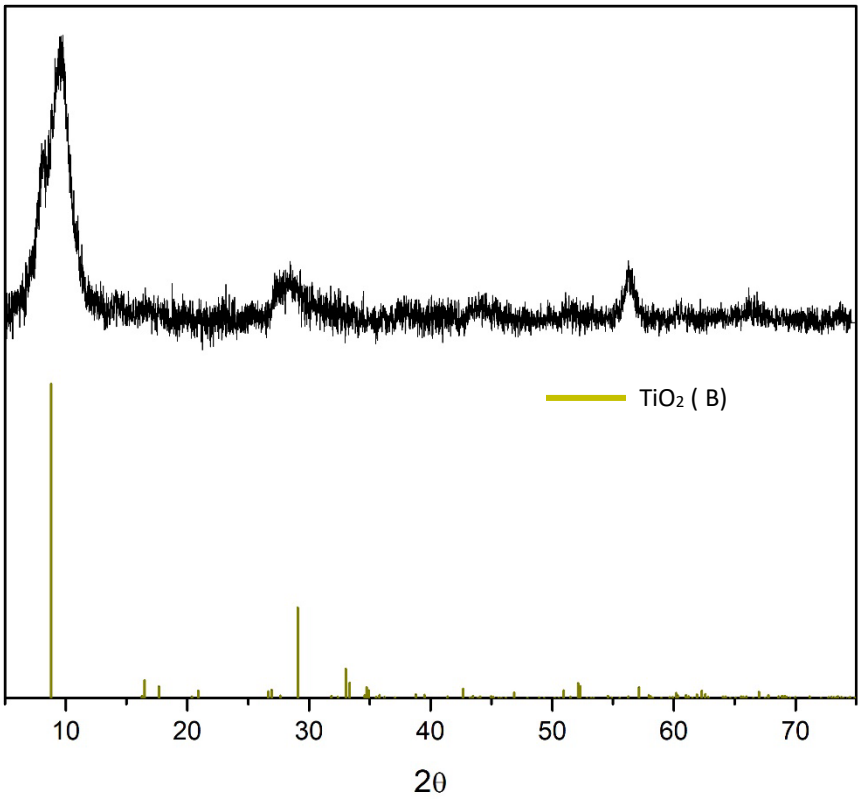

Figure 3.7. PXRD of the isolated product of the reaction of $BaCl_2 \cdot 2H_2O$ with H_x-TiO_2 for 1 day at 120°C.

We concluded that $BaCl_2 \cdot 2H_2O$ is not an effective barium source for this trans formation. Thus, we switched to $Ba(OH)_2 \cdot 8H_2O$ because of its low melting point of 78 °C, which makes it an extremely good flux for reactions in this temperature range (~120 °C). The greater hydration level of $Ba(OH)_2 \cdot 8H_2O$ compared to $BaCl_2 \cdot 2H_2O$ also means that a greater amount of water will be present within the reaction vessel, which can help keep the flux in the liquid state.

By studying at the behavior of $Ba(OH)_2 \cdot 8H_2O$, the first 7 waters of hydration leave the compound starting at 60 °C making it important to maintain in the system.[29] Therefore, Schlenk tubes were also used for this next set of reactions. Furthermore, $Ba(OH)_2 \cdot 8H_2O$ has been used to prepare barium-containing ternary metal oxides.[30-31]

Table 1 summarizes the experiments conducted with barium salt hydrates at various Ba:Ti molar ratios (fixed temperature of 120 °C, reactions in sealed Schlenk tubes). The results demonstrate the dramatic impact of both flux and molar ratio on the outcomes of these reactions. In short, $BaTiO_3$ nanosheets form cleanly under only specific conditions, from the reaction between H_x-TiO_2 nanosheets and $Ba(OH)_2$•$8H_2O$.

Table 1. Summary of synthetic experiments to form $BaTiO_3$ nanosheets (fixed temperature of 120 °C, reactions in sealed Schlenk tubes)

Barium Salt	Titanium source	Ratio of Ti:Ba	Results
$Ba(OH)_2$•$8H_2O$	$Cs_{0.7}Ti_{1.825}\square_{0.175}O_4$	1:8	$BaTiO_3$ nanoparticles
$Ba(OH)_2$•$8H_2O$	$Cs_{0.7}Ti_{1.825}\square_{0.175}O_4$	1:1	TiO_2 nanosheets
$BaCl_2$•$2H_2O$	H_x-TiO_2	1:8	$BaTiO_3$ nanoparticles
$BaCl_2$•$2H_2O$	H_x-TiO_2	1:1	TiO_2(B) nanosheets
$Ba(OH)_2$•$8H_2O$	H_x-TiO_2	1:8	Nanoparticles
$Ba(OH)_2$•$8H_2O$	H_x-TiO_2	1:2	Nanoparticles and nanosheets of TiO_2(B)
$Ba(OH)_2$•$8H_2O$	H_x-TiO_2	1:1	Nanosheets of TiO(OH)
$Ba(OH)_2$•$8H_2O$	H_x-TiO_2	1:1.5	Nanosheets of tetragonal $BaTiO_3$

Initial observations indicated greater condensation within the Schlenk tubes containing $Ba(OH)_2$•$8H_2O$ compared to $BaCl_2$•$2H_2O$, due to greater salt hydration. We also observed the H_x-TiO_2 nanosheets accumulating on the bottom of the reaction vessel (can be visualize in **Figure**

3.7a) as the $Ba(OH)_2•8H_2O$ started to melt, whereas with the $BaCl_2•2H_2O$ flux, the H_x-TiO_2 nanosheets remained unchanged even after 5 d.

The progress of the reaction containing a 1:1 ratio of $Ba(OH)_2•8H_2O$: H_x-TiO_2 was very different. After 1 d at 120 °C, the H_x-TiO_2 nanosheets changed color from white to off-white (seen in **Figure 3.8a**), so the reaction was terminated and processed for characterization. PXRD (**Figure 3.8b**) showed the presence of tetragonal $BaTiO_3$ together with titanium oxide hydroxide, $Ti_3O_5(OH)_2$ or better known as $H_2Ti_3O_7$ (Blue drop lines ICDD # 04-021-8783). These phases also can be distinguished by the sharpness of the $H_2Ti_3O_7$ peaks compared with the broadness of the nanostructured $BaTiO_3$ (red droplines) peaks. This material is one of the known protonated titanates. This material is known for forming in alkaline conditions and as a result of the intercalation of ions into the TiO_2 structures, especially with hydroxide salts.[32-35]

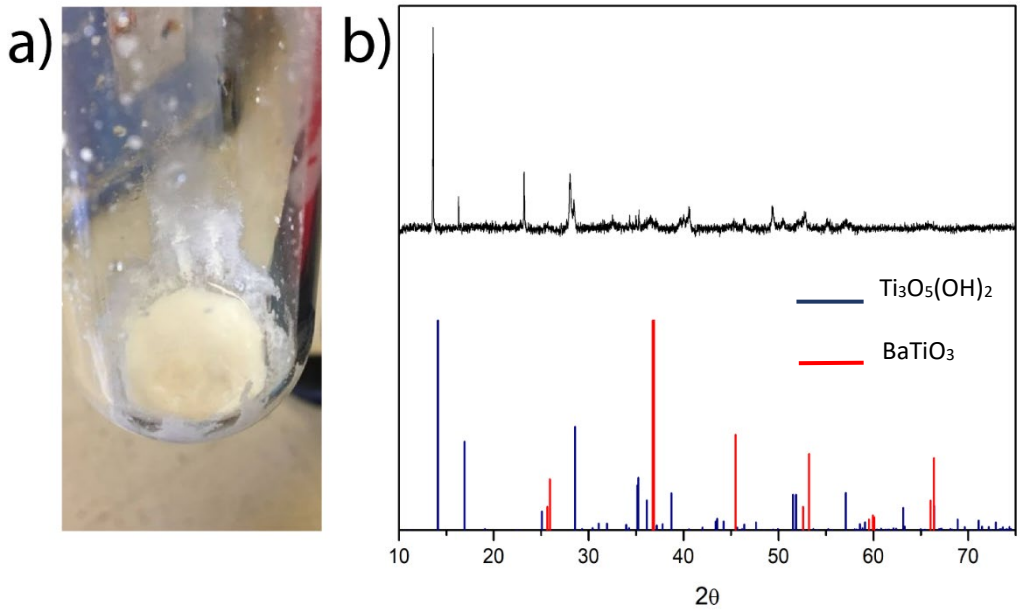

Figure 3.8. Reaction between $Ba(OH)_2•8H_2O$ and H_x-TiO_2 (1:1 ratio): a) photograph of the reaction mixture after 1 day at 120 °C, b) PXRD of the isolated product.

The next set of analyses included scanning electron microscopy with energy dispersive spectra to confirm the amount of barium in the nanostructured product. The data (**Figure 3.9**) showed the presence of nanosheets containing both barium and titanium, with good overlap between them by EDX mapping. However, the elemental analysis of 0.28:1 Ba:Ti spectra demonstrated a deficit of barium in these nanosheets.

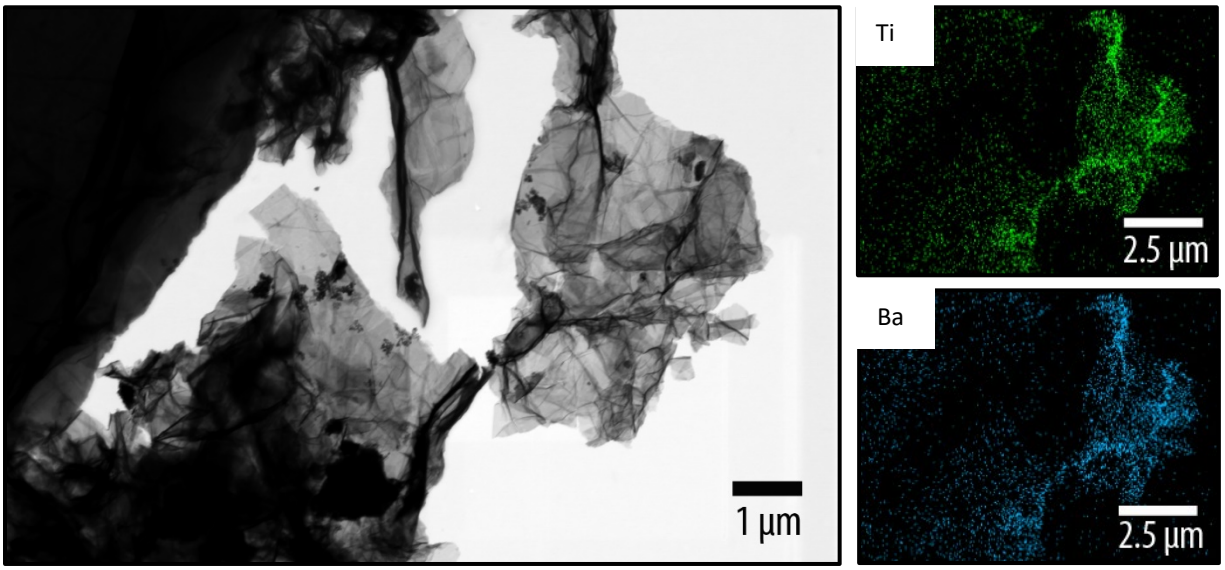

Figure 3.9. STEM and EDS image of Ba-deficient $BaTiO_3$ nanosheets.

Analysis by HRTEM (**Figure 3.10**) to better understand their structure revealed that these nanosheets exhibit a polycrystalline selected area electron diffraction pattern (**Figure 3.10b**). Another important result was the observation of numerous domains on a single nanosheet, some being polycrystalline (**Figure 3.10c**, taken from the red square area) and others being amorphous (**Figure 10d**, taken from the blue square area)

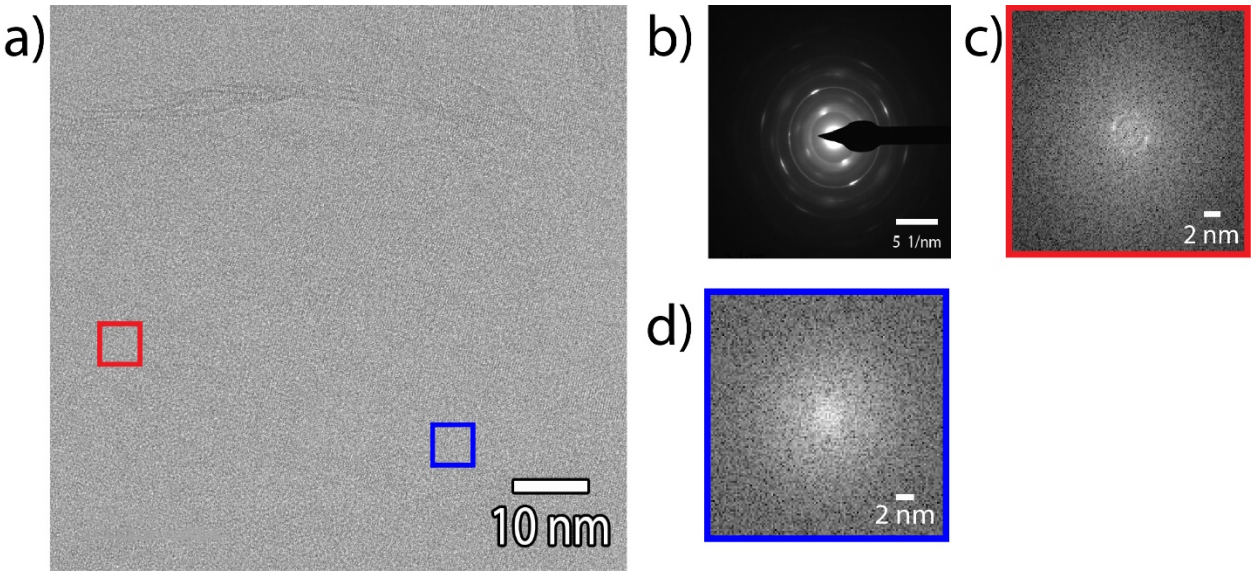

Figure 3.10. a) HRTEM and b) SAED image of Ba-deficient $BaTiO_3$ nanosheets.

We took advantage of an opportunity to collect electron energy loss spectroscopy data from this sample during TEM analysis (**Figure 3.11)**. The results confirm that we have barium and titanium atoms in the nanosheets in a 0.09:1 Ba:Ti ratio. The change in the results between the EDX and EELS studies correlate to the signal being stronger with a 300 kV (EELS) versus a 30kV (EDX). This intensity change can help with the Ba and Ti signals since the elements have very similar K_α, which makes it hard to distinguish the signals and amount of Ba and Ti in the sample.

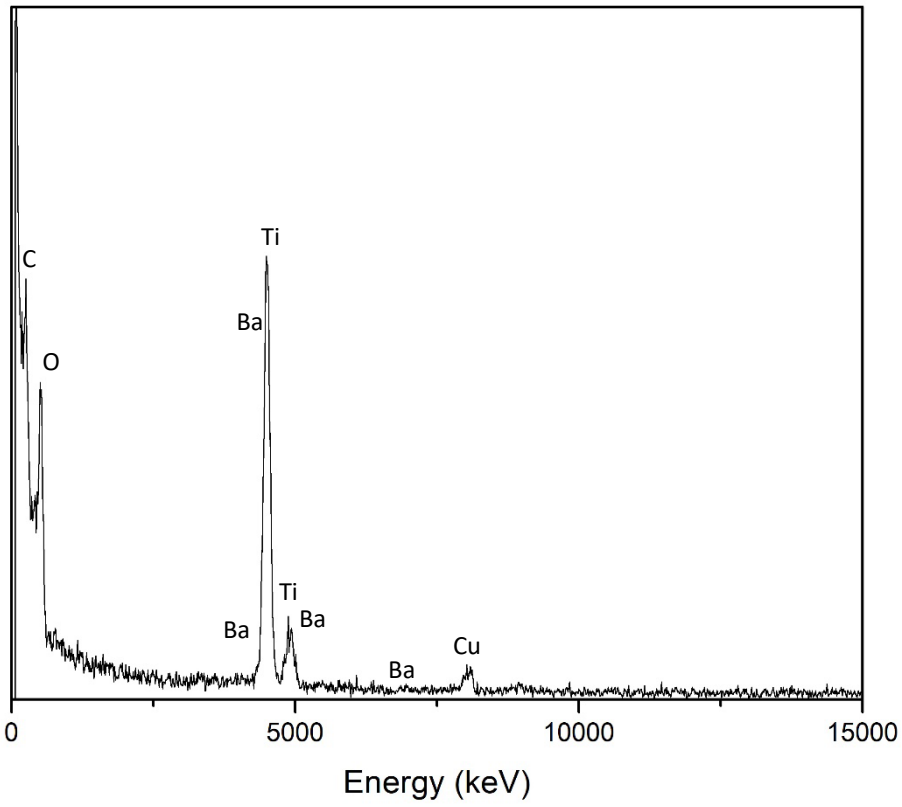

Figure 3.11. EELS spectrum of barium deficient $BaTiO_3$ nanosheets. Cu and C peaks originate from the TEM grid.

From these results, we concluded that an optimum stoichiometry of barium ions would be required; too much resulted in $BaTiO_3$ nanoparticles, not adding enough resulted in Ba-deficient $BaTiO_3$ nanosheets. A stoichiometry study showed that a ratio of 1.6:1 $Ba(OH)_2•8H_2$:H_x-TiO_2 gave ideal results. PXRD of the resulting product (**Figure 3.12**) revealed the presence of tetragonal $BaTiO_3$ and residual $Ba(OH)_2•8$ or 3 H_2O (marked by blue stars), which was the result of not-hot-enough water used to wash the product during workup. This phase was further confirmed by adding

$Ba(OH)_2•8H_2$ into a Schlenk vessel to heat in an oil bath for 1 day at 120°C. PXRD of this reaction showed a combination of $Ba(OH)_2•8H_2$ and $Ba(OH)_2•3H_2$.

Another piece of information available from PXRD data is the full width at half max (FWHM) of the peaks. This calculation has been used to both get the crystallite size of the material and, in the case of $BaTiO_3$ specifically, to distinguish between the tetragonal and cubic phases. This can be done because the (200) reflection in the tetragonal structure corresponds to two peaks, whereas it is a single peak for the cubic phase. By calculating the FWHM of the (111) and the (200) reflections, we can distinguish the difference that the second peak would make because the FWHM would be bigger since it includes two peaks. In other words, if the $FWHM_{(200)}$ value is larger than the $FWHM_{(111)}$ value, the material is considered tetragonal.[36-40] In our PXRD, the $FWHM_{(111)}$ was calculated to be 0.85° and the $FWHM_{(200)}$ was 1.01°, which helps confirm that the $BaTiO_3$ nanosheets have formed with the tetragonal perovskite phase.

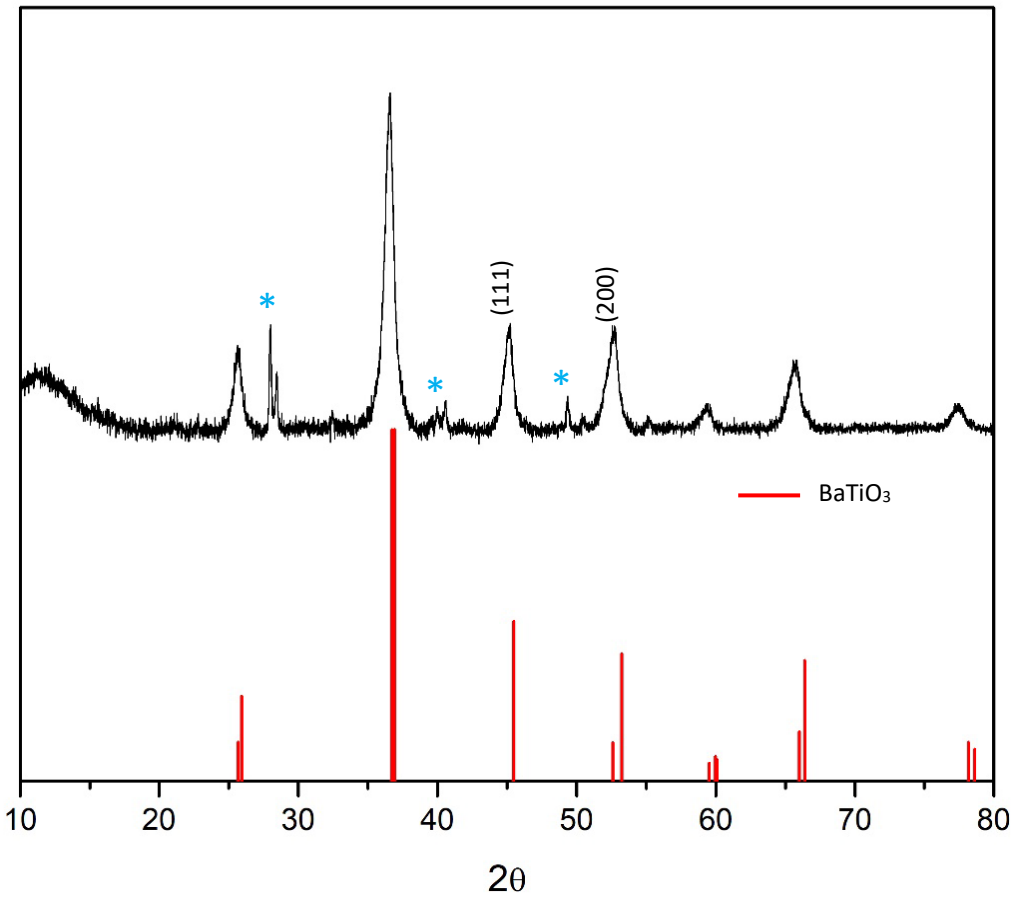

Figure 3.12. PXRD of 1.6:1 $Ba(OH)_2 \bullet 8H_2O$:H_x-TiO_2 reaction (blue stars indicate $Ba(OH)_2 \bullet 8H_2O$ (ICDD#04-009-5696)

After washing this material with hot water to remove excess $Ba(OH)_2 \cdot 8H_2O$, the dilute dispersion was drop-cast onto a Formvar carbon grid for STEM analysis. As shown in **Figure 3.13**, these nanosheets are quite large and have a crumpled nanosheet morphology. EDS provided a 3:1 Ba:Ti atomic ratio. Although this is not the theoretical value of 1:1, it is possible that Ba^{2+} ions associated with the nanosheet surface, along with the error of STEM-EDS on this microscope, can explain the experimental value. HRTEM studies are planned to fully confirm that the nanosheets are in fact $BaTiO_3$.

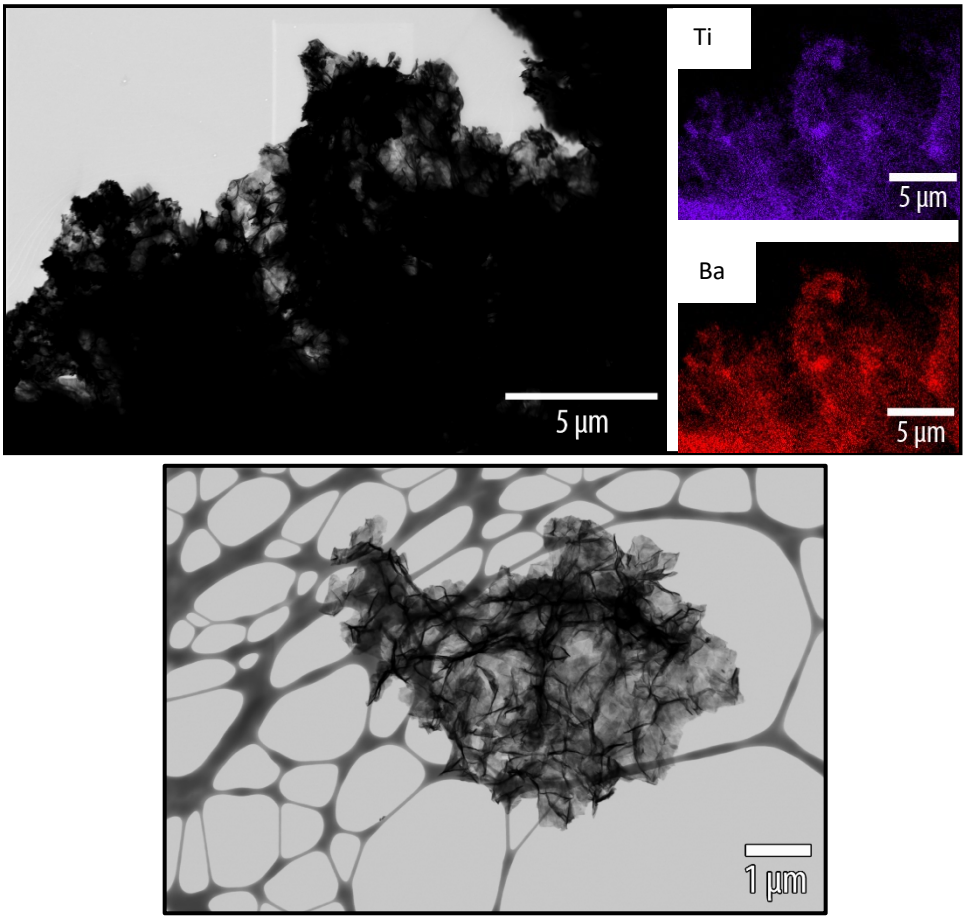

Figure 3.13. STEM of $BaTiO_3$ nanosheets.

Additionally, Raman spectroscopy provided additional evidence distinguishing the tetragonal crystal structure of $BaTiO_3$; the tetragonal, cubic, and hexagonal structures of $BaTiO_3$ have been well-characterized by this technique.[41] Sample preparation involved pressing freeze-dried nanosheets into a solid puck. The Raman measurements (**Figure 3.14**) showed distinct peaks at 250, 307, and 715 cm^{-1}, which correlate to the (A_1(TO)), (B_1, E(TO + LO)), and (A_1(LO), E(LO)) active modes. However, a peak at 515 cm^{-1} corresponding to the active mode (A_1(TO), E(TO)) was not observed, and the peaks around 250-320 cm^{-1} are not well-resolved. Therefore, more Raman studies are needed.

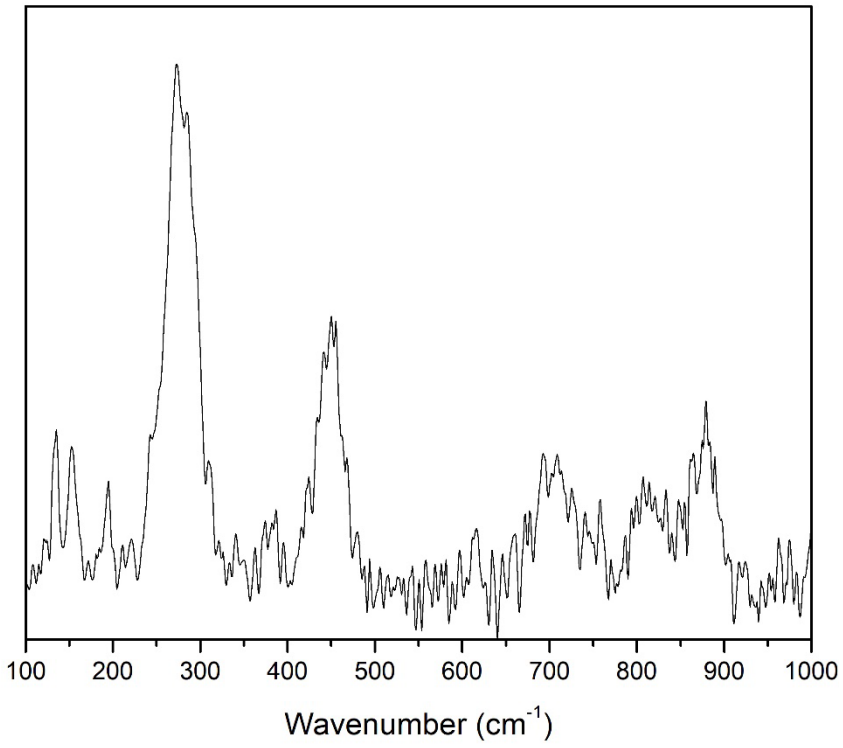

Figure 3.14. Raman spectrum of the $BaTiO_3$ nanosheets.

Another experiment included reaction stirring (with a magnetic stir bar) during $BaTiO_3$ nanosheet formation. The resulting product included many broken H_x-TiO_2 nanosheets, as seen in **Figure 3.15** (blue circles) and large, feathery $BaCl_2$•$2H_2O$ crystals, but no $BaTiO_3$.

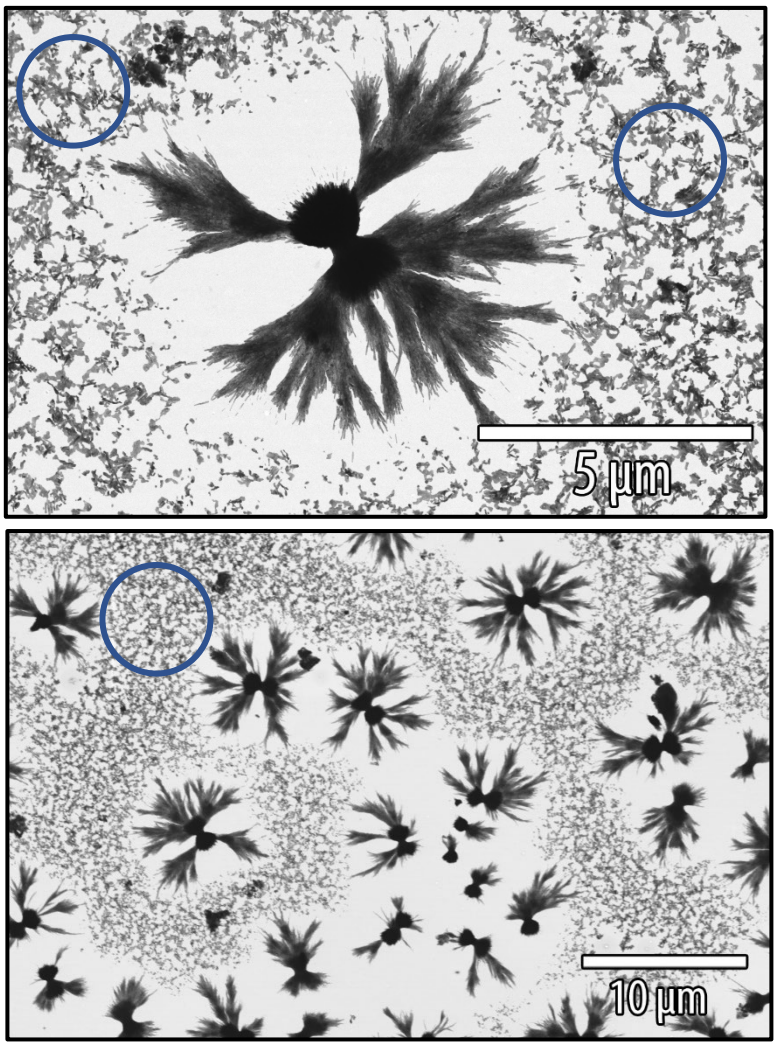

Figure 3.15. STEM images of $BaCl_2$•$2H_2O$ crystals blue circles identify broken H_xTiO_2 nanosheets.

Additional characterization of $BaTiO_3$ nanosheets by FTIR is shown in **Figure 3.16**. Hydrothermally processed $BaTiO_3$ have been previously reported to contain hydroxyl groups on the surface, this would show in the FTIR as a peak around 3500 cm^{-1}.[42-45]On our sample, we observed the peak at 3411 cm^{-1} signifying he presence of hydroxides in the surface of the material.

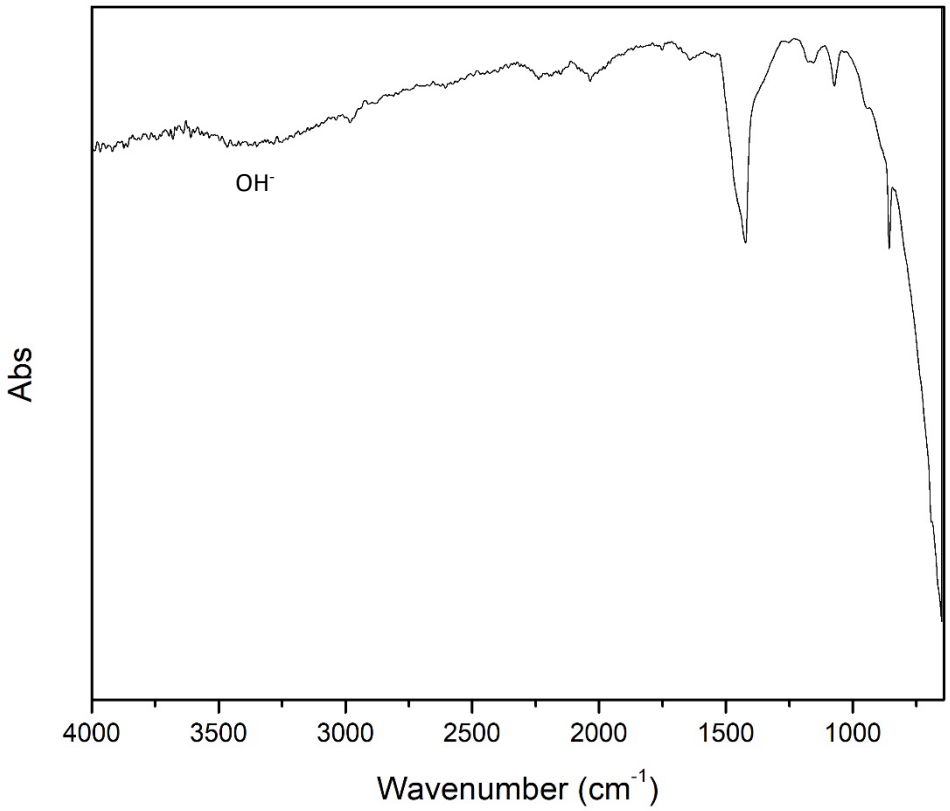

Figure 3.16. FTIR of tetragonal $BaTiO_3$ nanosheets.

Conclusion.

In this work, highly novel nanosheets of tetragonal $BaTiO_3$ were synthesized and characterized. Although these nanosheets previously were prepared in our lab by Dr. Chris Barrett, after many studies, it was discovered that the synthesis was not reproducible. Following my work on the $PbTiO_3$ nanosheet system, we decided to try and apply the information learned about the formation of these nanosheets from layered titanate precursors to this problem.

Hence, we decided to change the precursor used from $Cs_xTi_{2-x/4}\square_{x/4}O_4$ (□ = vacancy) to $(TBA)_{1.07}Ti_{1.73}O_4$. In order to make this new precursor sufficiently reactive, we treated $(TBA)_{1.07}Ti_{1.73}O_4$ with acid to exchange the TBA^+ for H^+, yielding H_x-TiO_2 nanosheets. For the subsequent reactions, it was necessary to freeze dry the nanosheet precursor to preserve their morphology.

Two barium salts were tested as fluxes, $BaCl_2•2H_2O$ and $Ba(OH)_2•8H_2O$; both salts have melting points lower than 120 °C when the waters of hydration are maintained in the system. Given this prerequisite, a Schlenk tube vessel was used to prevent the water from evaporating. The precursors were added to the vessel and placed on an oil bath for 1 day. The results with $BaCl_2•2H_2O$ resulted in unreacted nanosheets of TiO_2 and aggregates of $BaCl_2$, whereas the reactions with $Ba(OH)_2•8H_2O$ resulted in the targeted $BaTiO_3$ nanosheets.

Differences between nanosheet precursor have proven to be extremely important for the successful formation of $BaTiO_3$ nanosheets. The $Cs_xTi_{2-x/4}\square_{x/4}O_4$ (□ = vacancy) nanosheets originally used had no uniformity to their size and thickness, yielding no $BaTiO_3$ nanosheets even when the Cs^{2+} ion was exchanged with H^+. In the other hand H_x-TiO_2 proved to be more uniform in thickness (thinness) and have a higher reactivity towards Ba^{2+}.

Structural characterization showed that the $BaTiO_3$ nanosheets exhibited the desired tetragonal structure. This was confirmed by PXRD and Raman spectroscopy. Although atomic composition was not ideal according to the techniques at our disposal, this will be studied in the future. For example, HRTEM and SAED can further confirm the tetragonality of the nanosheets. In addition, we look forward to applying techniques that reveal the ferroelectric response of this material.

References

1. Piskunov, S.; Heifets, E.; Eglitis, R.; Borstel, G., Bulk properties and electronic structure of $SrTiO_3$, $BaTiO_3$, $PbTiO_3$ perovskites: an ab initio HF/DFT study. *Computational Materials Science* **2004,** *29* (2), 165-178.

2. Jaffe, B., *Piezoelectric ceramics*. Elsevier: 2012; Vol. 3.

3. Luan, W.; Gao, L.; Guo, J., Size effect on dielectric properties of fine-grained $BaTiO_3$ ceramics. *Ceramics international* **1999,** *25* (8), 727-729.

4. MacChesney, J.; Gallagher, P.; DiMarcello, F., Stabilized barium titanate ceramics for capacitor dielectrics. *Journal of the American Ceramic Society* **1963,** *46* (5), 197-202.

5. Abel, S.; Stöferle, T.; Marchiori, C.; Caimi, D.; Czornomaz, L.; Stuckelberger, M.; Sousa, M.; Offrein, B. J.; Fompeyrine, J., A hybrid barium titanate–silicon photonics platform for ultraefficient electro-optic tuning. *Journal of Lightwave Technology* **2016,** *34* (8), 1688-1693.

6. Heywang, W., Semiconducting barium titanate. *Journal of Materials Science* **1971,** *6* (9), 1214-1224.

7. Stein, A.; Keller, S. W.; Mallouk, T. E., Turning down the heat: Design and mechanism in solid-state synthesis. *Science* **1993,** *259* (5101), 1558-1564.

8. Malachevsky, M. T.; Fiscina, J. E.; Esparza, D. A., Preparation of Synthetic Cordierite by Solid-State Reaction via Bismuth Oxide Flux. *Journal of the American Ceramic Society* **2001,** *84* (7), 1575-1577.

9. Bouwmeester, H. J.; Kruidhof, H.; Burggraaf, A., Importance of the surface exchange kinetics as rate limiting step in oxygen permeation through mixed-conducting oxides. *Solid state ionics* **1994,** *72*, 185-194.

10. Afanasiev, P.; Rawas, L.; Vrinat, M., Synthesis of dispersed Mo sulfides in the reactive fluxes containing liquid sulfur and alkali metal carbonates. *Materials chemistry and physics* **2002,** *73* (2-3), 295-300.

11. Wold, A.; Dwight, K., *Solid state chemistry: synthesis, structure, and properties of selected oxides and sulfides*. Springer Science & Business Media: 2012.

12. Kanatzidis, M. G.; Sutorik, A. C., The application of polychalcogenide salts to the exploratory synthesis of solid state multinary chalcogenides at intermediate temperatures. *Progress in Inorganic Chemistry* **1995**, 151-265.

13. Han, P.; Jiang, X., Regulation on the synthesis temperature and optical properties of SmBO3 prepared by chloride fluxes assisted the solid state reaction method. *Advanced Powder Technology* **2015,** *26* (3), 977-982.

14. Kim, Y., Lithium nickel cobalt manganese oxide synthesized using alkali chloride flux: morphology and performance as a cathode material for lithium ion batteries. *ACS applied materials & interfaces* **2012,** *4* (5), 2329-2333.

15. Teshima, Katsuya, et al. "Growth of well-developed Li4Ti5O12 crystals by the cooling of a sodium chloride flux." *Crystal growth & design* 11.10 (2011): 4401-4405.

16. Khan, A. I.; O'Hare, D., Intercalation chemistry of layered double hydroxides: recent developments and applications. *Journal of Materials Chemistry* **2002,** *12* (11), 3191-3198.

17. Mugavero III, S. J.; Gemmill, W. R.; Roof, I. P.; zur Loye, H.-C., Materials discovery by crystal growth: Lanthanide metal containing oxides of the platinum group metals (Ru, Os, Ir, Rh, Pd, Pt) from molten alkali metal hydroxides. *Journal of Solid State Chemistry* **2009,** *182* (7), 1950-1963.

18. Bharathy, M.; Fox, A. H.; Mugavero, S.; zur Loye, H.-C., Crystal growth of inter-lanthanide LaLn′ O_3 (Ln′= Y, Ho–Lu) perovskites from hydroxide fluxes. *Solid state sciences* **2009,** *11* (3), 651-654.

19. Roof, I. P.; Smith, M. D.; zur Loye, H.-C., Crystal growth of K_2UO_4 and Na_4UO_5 using hydroxide fluxes. *Journal of crystal growth* **2010,** *312* (8), 1240-1243.

20. Stitzer, K. E.; Smith, M. D.; zur Loye, H.-C., Crystal growth of Ba_2MOsO_6 (M= Li, Na) from reactive hydroxide fluxes. *Solid State Sciences* **2002,** *4* (3), 311-316.

21. Sasaki, T.; Watanabe, M.; Michiue, Y.; Komatsu, Y.; Izumi, F.; Takenouchi, S., Preparation and acid-base properties of a protonated titanate with the lepidocrocite-like layer structure. *Chemistry of materials* **1995,** *7* (5), 1001-1007.

22. Buscaglia, M. T.; Buscaglia, V.; Alessio, R., Coating of BaCO3 crystals with TiO_2: versatile approach to the synthesis of $BaTiO_3$ tetragonal nanoparticles. *Chemistry of materials* **2007,** *19* (4), 711-718.

23. Nuraje, N.; Su, K.; Haboosheh, A.; Samson, J.; Manning, E. P.; Yang, N. l.; Matsui, H., Room temperature synthesis of ferroelectric barium titanate nanoparticles using peptide nanorings as templates. *Advanced Materials* **2006,** *18* (6), 807-811.

24. Hakuta, Y.; Ura, H.; Hayashi, H.; Arai, K., Continuous production of $BaTiO_3$ nanoparticles by hydrothermal synthesis. *Industrial & engineering chemistry research* **2005,** *44* (4), 840-846.

25. Moreira, M.; Mambrini, G.; Volanti, D.; Leite, E.; Orlandi, M.; Pizani, P.; Mastelaro, V.; Paiva-Santos, C.; Longo, E.; Varela, J. A., Hydrothermal microwave: a new route to obtain photoluminescent crystalline BaTiO3 nanoparticles. *Chemistry of Materials* **2008,** *20* (16), 5381-5387.

26. Zhou, T.; Zha, J.-W.; Cui, R.-Y.; Fan, B.-H.; Yuan, J.-K.; Dang, Z.-M., Improving dielectric properties of $BaTiO_3$/ferroelectric polymer composites by employing surface hydroxylated $BaTiO_3$ nanoparticles. *ACS applied materials & interfaces* **2011,** *3* (7), 2184-2188.

27. Choi, S.-H.; Kim, I.-D.; Hong, J.-M.; Park, K.-H.; Oh, S.-G., Effect of the dispersibility of $BaTiO_3$ nanoparticles in $BaTiO_3$/polyimide composites on the dielectric properties. *Materials Letters* **2007,** *61* (11-12), 2478-2481.

28. Tanaka, T.; Ebina, Y.; Takada, K.; Kurashima, K.; Sasaki, T., Oversized titania nanosheet crystallites derived from flux-grown layered titanate single crystals. *Chemistry of materials* **2003,** *15* (18), 3564-3568.

29. Lutz, H.; Eckers, W.; Christian, H.; Engelen, B., Hydrates of barium hydroxide. Preparation, thermal decomposition and X-ray data. *Thermochimica Acta* **1981,** *44* (3), 337-343.

30. Imai, Y.; Kato, M.; Noji, T.; Koike, Y. In *Electrochemical Synthesis of the Perovskite Ba1 x Cs x BiO3 from Molten Salts*, AIP Conference Proceedings, American Institute of Physics: 2006; pp 669-670.

31. Mugavero III, S. J.; Bharathy, M.; McAlum, J.; zur Loye, H.-C., Crystal growth of alkaline earth vanadates from hydroxide fluxes. *Solid state sciences* **2008,** *10* (4), 370-376.

32. Bavykin, D. V.; Friedrich, J. M.; Walsh, F. C., Protonated titanates and TiO2 nanostructured materials: synthesis, properties, and applications. *Advanced materials* **2006,** *18* (21), 2807-2824.

33. Nalbandyan, V.; Trubnikov, I., The rearrangement of the structures of layer titanates during ion exchange. *Russian Journal of Inorganic Chemistry* **1987,** *32* (5), 639-643.

34. Zhang, S.; Peng, L.-M.; Chen, Q.; Du, G.; Dawson, G.; Zhou, W., Formation Mechanism of H 2 T i 3 O 7 Nanotubes. *Physical Review Letters* **2003,** *91* (25), 256103.

35. Zhang, S.; Chen, Q.; Peng, L.-M., Structure and formation of $H_2Ti_3O_7$ nanotubes in an alkali environment. *Physical Review B* **2005,** *71* (1), 014104.

36. Fujimoto, K.; Kobayashi, Y.; Kubota, K., Growth of $BaTiO_3$□ $SrTiO_3$ thin films by rf magnetron sputtering. *Thin Solid Films* **1989,** *169* (2), 249-256.

37. Hakuta, Y.; Ura, H.; Hayashi, H.; Arai, K., Effect of water density on polymorph of BaTiO3 nanoparticles synthesized under sub and supercritical water conditions. *Materials Letters* **2005,** *59* (11), 1387-1390.

38. Matsui, K.; Noguchi, T.; Islam, N. M.; Hakuta, Y.; Hayashi, H., Rapid synthesis of $BaTiO_3$ nanoparticles in supercritical water by continuous hydrothermal flow reaction system. *Journal of crystal growth* **2008,** *310* (10), 2584-2589.

39. Wada, S.; Yasuno, H.; Hoshina, T.; Nam, S.-M.; Kakemoto, H.; Tsurumi, T., Preparation of nm-sized barium titanate fine particles and their powder dielectric properties. *Japanese journal of applied physics* **2003,** *42* (9S), 6188.

40. Lee, M. B.; Kawasaki, M.; Yoshimoto, M.; Koinuma, H., Heteroepitaxial growth of BaTiO3 films on Si by pulsed laser deposition. *Applied Physics Letters* **1995,** *66* (11), 1331-1333.

41. Gajović, A.; Pleština, J. V.; Žagar, K.; Plodinec, M.; Šturm, S.; Čeh, M., Temperature-dependent Raman spectroscopy of $BaTiO_3$ nanorods synthesized by using a template-assisted sol–gel procedure. *Journal of Raman Spectroscopy* **2013,** *44* (3), 412-420.

42. Aal, A. A.; Hammad, T.; Zawrah, M.; Battisha, I.; Abou Hammad, A., FTIR study of nanostructure perovskite $BaTiO_3$ doped with both Fe^{3+} and Ni^{2+} ions prepared by sol-gel technique. *Acta Phys. Pol. A* **2014,** *126* (6), 1318-1322.

43. Ashiri, R., Detailed FT-IR spectroscopy characterization and thermal analysis of synthesis of barium titanate nanoscale particles through a newly developed process. *Vibrational Spectroscopy* **2013,** *66*, 24-29.

44. Mullens, J.; Van Werde, K.; Vanhoyland, G.; Nouwen, R.; Van Bael, M.; Van Poucke, L., The use of TGA-MS, TGA-FTIR, HT-XRD and HT-DRIFT for the preparation and characterization of PbTiO3 and BaTiO3. *Thermochimica acta* **2002,** *392*, 29-35.

45. Patil, S. K.; Shah, N.; Blum, F. D.; Rahaman, M. N., Fourier transform infrared analysis of hydroxyl content of hydrothermally processed heteroepitaxial barium titanate films. *Journal of materials research* **2005,** *20* (12), 3312-3319.

CHAPTER IV

TEMPLATED GROWTH OF STRONTIUM TITANATE

Introduction

Strontium titanate ($SrTiO_3$) is a material of great interest as a low-temperature ferroelectric material that is also an insulator and dielectric material. This is because the transition temperature for this perovskite is -163 °C (110 K),[1] making it one of the few titanium-based perovskites that has a cubic structure at room temperature. Here we describe the attempts to synthesize freestanding nanosheets of $SrTiO_3$ by a templated direct flux synthesis. The template is $(TBA)_{1.07}Ti_{1.73}O_4$, a well-known, 2D-nanostructured analog of TiO_2(B). $(TBA)_{1.07}Ti_{1.73}O_4$ is converted to a more reactive form, H_xTiO_2, prior to reactions with $Sr(OH)_2 \bullet 8H_2O$, a low-melting salt that acts as both flux and Sr source. These initial synthetic studies are described in this chapter.

Strontium titanate is the third and last member of the inorganic perovskite family that I will be discussing. This material is of great interest as a low temperature, ferroelectric material. This is because the transition temperature for this perovskite is -163 °C (110 K),[1] making it one of the few titanium perovskites that has a cubic structure at room temperature. However, this material is an insulator at room temperature, making it extremely useful as a dielectric material. It also has a band gap of 3.15eV making it possible for this material to be used as a photocatalytic material.

The synthetic route that we want to take with this material is the same as with the $BaTiO_3$, a melt flux method. Like it was stated in the previous chapter, flux-based syntheses are used to prepare materials at lower temperatures than solid state reactions. The flux acts as a solvent by enhancing the diffusion of reactants.[2] Common flux materials include oxides,[3-4] sulfides,[5-7] chlorides,[8-10] and hydroxides.[11-15]

We utilize a hydrated chloride salt as the source of strontium ($SrCl_2 \cdot 6H_2O$) as well as two different sources of titanium ($Cs_{0.7}Ti_{1.825}\square_{0.175}O_4$ (□ = vacancy) and $(TBA)_{1.07}Ti_{1.73}O_4$).[16-17] In this chapter we examine the attempts that we have made to synthesize nanosheets of $SrTiO_3$ as well as the results and characterizations of the obtained materials.

Experimental

Materials: Li_2CO_3 (Sigma-Aldrich Corp.), MoO_3 (Sigma-Aldrich Corp., 99.5%), K_2CO_3 (Sigma-Aldrich Corp.), Anatase (Sigma-Aldrich Corp., 99.8%), TBAOH (Sigma-Aldrich Corp., 1M HPLC), HCl (Sigma-Aldrich Corp., 37% w/v).

Preparation of the nanostructured cesium titanate precursor: This procedure followed the details published by Sasaki et al.,[17] where cesium titanate of composition $Cs_{0.7}Ti_{1.825}\square_{0.175}O_4$ (□ = vacancy) was synthesized by firing a finely ground mixture of 3.2582 g Cs_2CO_3 and 4.2329 g TiO_2 (1:5.3 in molar ratio) at 1173 K. The sample was calcined twice for a period of 24 h each time, with additional grinding (mortar & pestle) between calcinations. The resulting material was ground down once more before being dispersed in 1 M HCl(aq) (150 mL g^{-1}) and shaken for 5 d with a linear shaker at 74 RPM. The acid was replaced each day (by centrifugation at 10,000 RPM on an Allegra 64-R centrifuge. Following this acid leaching of Cs^+, the remaining solid was washed with copious amounts of deionized water to remove all acid residue and re-dispersed in 500 mL of 0.5 M TBA(OH) solution. The resulting nanosheets were washed by centrifugation and re-dispersed in water before being used for the reactions after calculating the grams of material per mL of water by drying 1mL of the solution in a previously measured microscope slide.

Preparation of $SrTiO_3$ from the cesium titanate precursor: 0.1000 g $Cs_{0.7}Ti_{1.825}\square_{0.175}O_4$ nanosheets (of the 1.25 mM dispersion) were mixed with 3.000 g of $SrCl_2 \cdot 6H_2O$ (19 mmol) and transferred to a 18.6 g (size) platinum crucible. The mixture was then gently melted at 95 °C inside a furnace over a period of 2 h with periodic stirring with a Teflon stirring rod. Once melted, the homogenous mixture was transferred to a Teflon sleeve, sealed in a stainless steel autoclave, and quickly heated to 180 °C, which was maintained for 45 min. After cooling to room temperature, the sample was removed and washed with copious amounts of boiling water, followed by mild sonication for 1 h.

The sample was then centrifuged for 10 min at 10,000 rpm on an allegra 64-R centrifuge, after which the supernatant was discarded and the precipitate re-dispersed in fresh deionized water. The centrifuge step was repeated twice more before re-dispersing the solid in ~5 mL of water.

Preparation of $(TBA)_{1.07}Ti_{1.73}O_4$: 5.000 g (62.6 mmol) of TiO_2 anatase is ground together with 8.3522 g (60.4 mmol) of K_2CO_3, 0.347 6g (4.70 mmol) of Li_2CO_3, and 6.6152g (45.9 mmol) of MoO_3 in a mortar and pestle for 15 minutes. The powder is placed into a Pt crucible and ramped up to 1200 °C at 10 °C/min and held there for 10 h. It is cooled slowly at 4 °C/h down to 900 °C and then it is cool down to room temperature. The large $K_{0.8}Ti_{1.73}Li_{0.27}O_4$ crystals are separated from the K_2MoO_4 flux using excess hot water. The $K_{0.8}Ti_{1.73}Li_{0.27}O_4$ crystals are shaken in 500 mL of 1M HCl for 5 days in a linear shaker at 78 RPM. A fresh 500 mL of 1M HCl is added each day by decanting the acid after centrifuging for 30 min at 10,000 RPM. After the fifth day the crystals are fully protonated ($H_{1.07}Ti_{1.73}O_4$) and the acid is exchanged for 500 mL of 0.5 M tetrabutylammonium hydroxide (TBAOH) solution and shaken again at 78 RPM for 7 days. Finally, the excess TBAOH solution is decanted by centrifuging at 10,000 RPM for 1 hour and the nanosheets are re-dispersed in 1L DI water.

Reaction of $(TBA)_{1.07}Ti_{1.73}O_4$ with $SrCl_2 \cdot 6H_2O$: 0.3965 g (2.5 mmol) of $SrCl_2 \cdot 6H_2O$ were added to a Schlenk tube containing 0.2000 g of the *$(TBA)_{1.07}Ti_{1.73}O_4$* (from a suspension of 0.0056 g/mL). The reaction was sealed in air, and the tube was half submerged in an oil bath. The reaction was heated up to 120 °C and left to react for 1 d. After the reaction was done, the solids were washed with 30 mL of water 4× to dissolve any remaining $SrCl_2 \cdot 6H_2O$. The resulting dispersion was centrifuged at 10,000 RPM on an allegra 64-R centrifuge.

Characterization details

Powder X-ray diffraction (PXRD) data was collected on a Bruker D8 instrument utilizing a Co−Kα X-ray source (λ = 1.78890 Å) operated at 40 kV and 35 mA. Data was collected from 10° to 80° 2θ with a scan rate of 0.1 s/step. Samples were prepared as powder mounts or drop cast from solution.

Transmission electron microscopy (TEM) imaging and selected area electron diffraction (SAED) analyses were performed using a FEI Tecnai 20 transmission electron microscope with an accelerating voltage of 200 kV. High resolution transmission electron microscopy (HRTEM) was performed with a FEI Tecnai G2 F30 S-TWIN operating at 300 kV. Samples were drop cast onto Formvar, holey carbon, or lacey carbon grids and air-dried.

Scanning electron microscopy (SEM) and scanning transmission electron microscopy (STEM) analyses were performed using a FEI Teneo FE-SEM at 10-30 kV with a spot size of 10. Samples were drop cast onto silicon wafer or Formvar grids.

Results and discussion

During the initial stage of this project, I re-examined experiments conducted by a former lab member, Dr. Chris Barrett, starting from $Cs_xTi_{2-x/4}\square_{x/4}O_4$ (□ = vacancy) nanosheets (as synthesized from procedure in chapter III) as the template for $SrTiO_3$ nanosheet formation.[17] The $Cs_xTi_{2-x/4}\square_{x/4}O_4$ morphology, like previously mention on Chapter III, is thicker than the $(TBA)_{1.07}Ti_{1.73}O_4$ nanosheets. However, the nanosheets are still in the TiO_2(B) structure. Reactions of $Cs_xTi_{2-x/4}\square_{x/4}O_4$ nanosheets with $SrCl_2{\bullet}6H_2O$ in an 8:1 molar ratio under hydrothermal conditions (120 °C) yielded nanoparticles of TiO_2 as seen in **Figure 4.1a**. In **Figure 4.1b**, PXRD shows the nanoparticles being the bronze polymorph of $Cs_{0.68}Ti_{1.83}O_4$ (ICDD#00-040-0827).

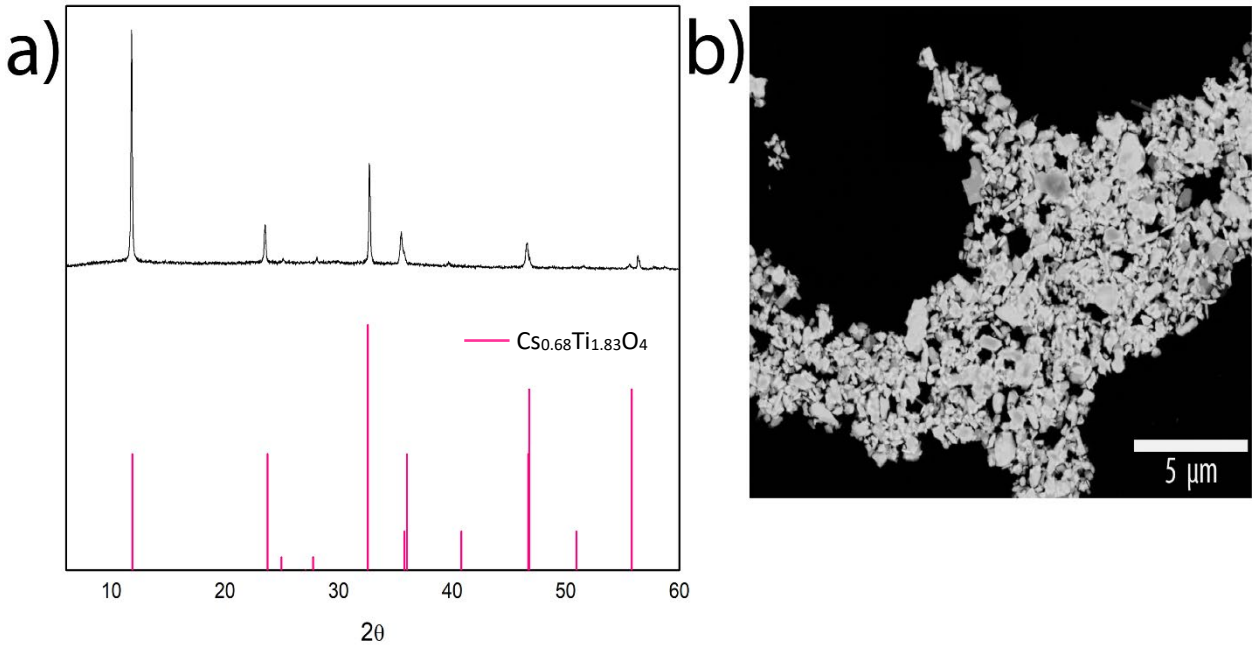

Figure 4.1. a) PXRD and b) STEM image of $Cs_{0.68}Ti_{1.83}O_4$ nanoparticles.

Based on these results, I next examined direct reactions of $Cs_xTi_{2-x/4}\square_{x/4}O_4$ with $SrCl_2 \cdot 6H_2O$ as both flux and Sr source. The reaction vessel was a sealed Schlenk tube to prevent the evaporation of the water in the system. Similarly, to the barium system, the strontium salts when anhydrous have a higher melting point (874°C anhydrous vs. 115°C hexahydrate). However, even with these changes, no $SrTiO_3$ nanosheets were isolated.

Because the $Cs_xTi_{2-x/4}\square_{x/4}O_4$ nanosheets did not yield the desired $SrTiO_3$ nanosheets, we decided to switch the nanosheet template/precursor that led to success in the $PbTiO_3$ and $BaTiO_3$ systems, namely $(TBA)_{1.07}Ti_{1.73}O_4$.[16] The reaction of still TBA-capped $(TBA)_{1.07}Ti_{1.73}O_4$ nanosheets with $SrCl_2 \cdot 6H_2O$, provided a nanosheet product as seen by STEM imaging (**Figure 4.2a**). However, EDS analysis showed that Cl was present at 2% (Sr had 11%), which suggests that $SrCl_2$ ions may be coordinated to the surface of the titanate nanosheet rather than in the form of $SrTiO_3$. . To further confirm this, the PXRD (**Figure 4.2b**) showed TiO_2(B) (ICDD#03-065-6429) to be the only phase present.

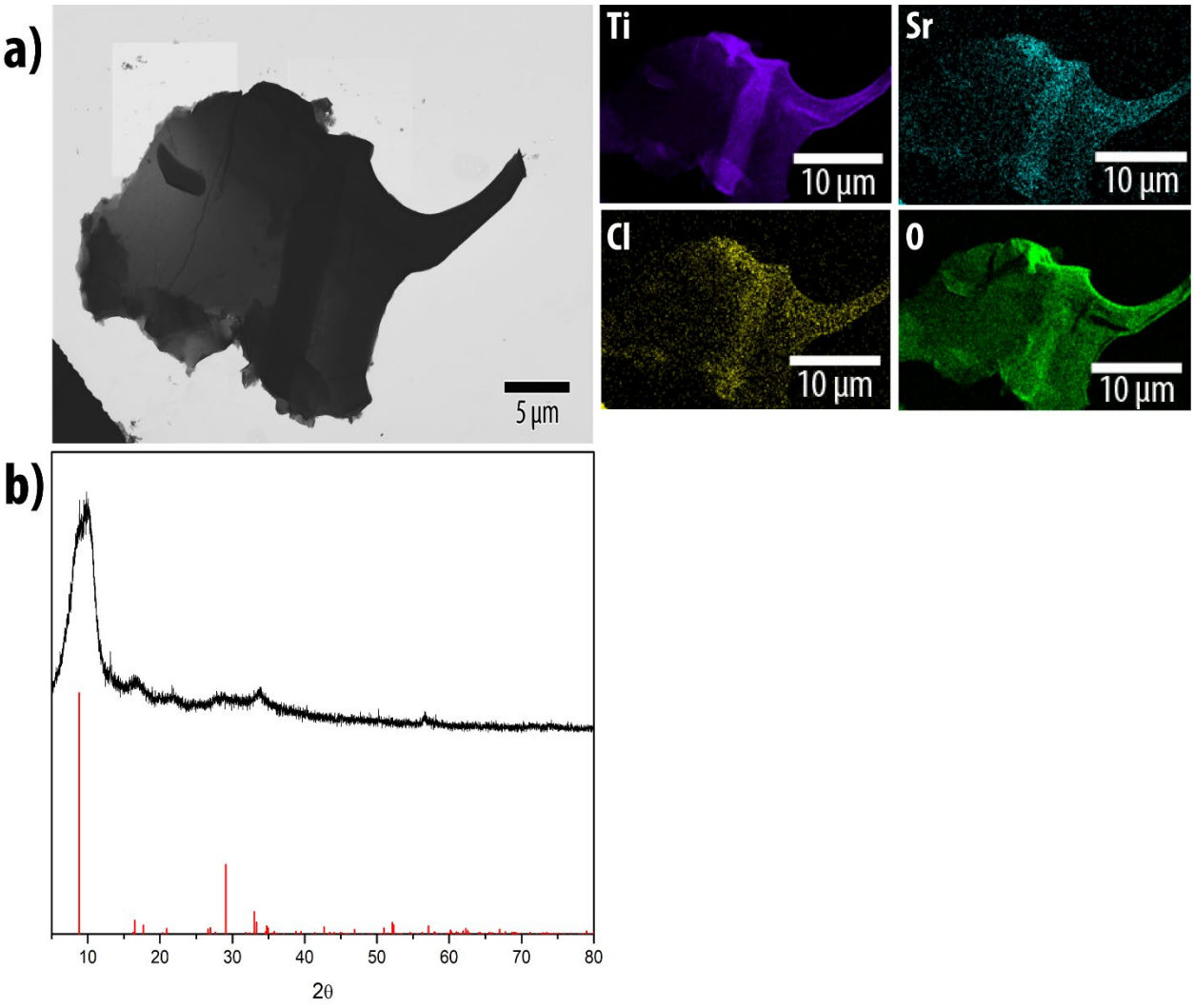

Figure 4.2. a) STEM image with EDX analysis and b) PXRD of TiO_2 nanosheets.

For the next set of reactions, the $(TBA)_{1.07}Ti_{1.73}O_4$ nanosheets were treated with acid to create H_x-TiO_2 flocculate, which was reacted with $SrCl_2 \cdot 6H_2O$ in a Schlenk vessel for 1 day at 120 °C. The resulting powder was bath sonicated and re-dispersed in water. As seen by STEM imaging and EDS mapping (**Figure 4.3**), the product maintains a nanosheet morphology and exhibits good overlap of Ti and O. However, Sr is present in low concentration at a ratio of 0.14:1 Sr:Ti. This result means that Sr is not being fully incorporated into the titanate structure.

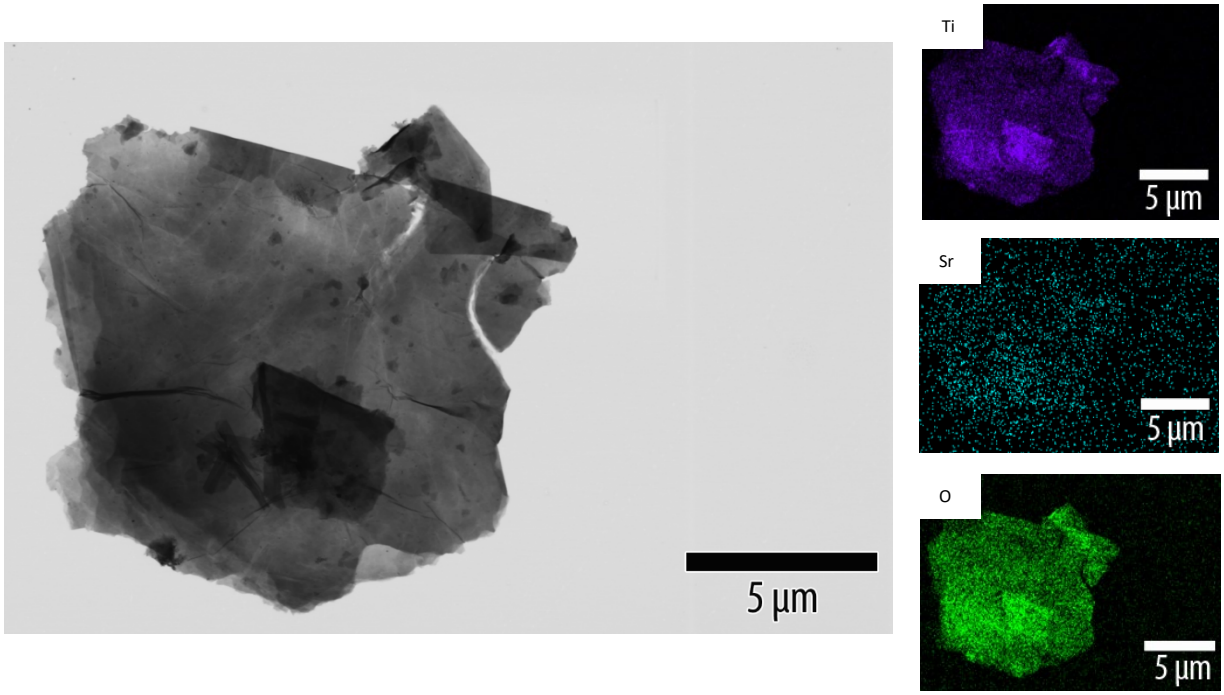

Figure 4.3. STEM imaging and EDS mapping of product.

Conclusion

These initial results are promising. Continuing work should focus on the reaction between H_x-TiO_2 and strontium. The next step on the process would be to try a different salt of strontium such as $Sr(OH)_2 \bullet 8H_2O$. The hydroxide salts have shown great results when used with the H_x-TiO_2 nanosheets, as demonstrated in Chapter IV. In the $BaTiO_3$ system, we discovered that hydroxide salts yielded better nanosheets than the chloride salt, and thus are the better alkaline earth source and flux for these types of reactions. We also discovered that heat affects H_x-TiO_2 nanosheets, causing them to fragment at >160 °C. This is important to consider since the we do not want to form nanoparticles of $SrTiO_3$, and we are using this nanosheets as templates.

Overall, more studies need to be made for the $SrTiO_3$ system but, given all that we have learned from the $PbTiO_3$ and $BaTiO_3$ systems, we are confident that it will be possible to create nanosheets of $SrTiO_3$.

References

1. Saifi, M. A.; Cross, L., Dielectric properties of strontium titanate at low temperature. *Physical Review B* **1970,** *2* (3), 677.

2. Stein, A.; Keller, S. W.; Mallouk, T. E., Turning down the heat: Design and mechanism in solid-state synthesis. *Science* **1993,** *259* (5101), 1558-1564.

3. Malachevsky, M. T.; Fiscina, J. E.; Esparza, D. A., Preparation of Synthetic Cordierite by Solid-State Reaction via Bismuth Oxide Flux. *Journal of the American Ceramic Society* **2001,** *84* (7), 1575-1577.

4. Bouwmeester, H. J.; Kruidhof, H.; Burggraaf, A., Importance of the surface exchange kinetics as rate limiting step in oxygen permeation through mixed-conducting oxides. *Solid state ionics* **1994,** *72*, 185-194.

5. Afanasiev, P.; Rawas, L.; Vrinat, M., Synthesis of dispersed Mo sulfides in the reactive fluxes containing liquid sulfur and alkali metal carbonates. *Materials chemistry and physics* **2002,** *73* (2-3), 295-300.

6. Wold, A.; Dwight, K., *Solid state chemistry: synthesis, structure, and properties of selected oxides and sulfides*. Springer Science & Business Media: 2012.

7. Kanatzidis, M. G.; Sutorik, A. C., The application of polychalcogenide salts to the exploratory synthesis of solid state multinary chalcogenides at intermediate temperatures. *Progress in Inorganic Chemistry* **1995**, 151-265.

8. Han, P.; Jiang, X., Regulation on the synthesis temperature and optical properties of SmBO3 prepared by chloride fluxes assisted the solid state reaction method. *Advanced Powder Technology* **2015,** *26* (3), 977-982.

9. Kim, Y., Lithium nickel cobalt manganese oxide synthesized using alkali chloride flux: morphology and performance as a cathode material for lithium ion batteries. *ACS applied materials & interfaces* **2012,** *4* (5), 2329-2333.

10. Teshima, Katsuya, et al. "Growth of well-developed Li4Ti5O12 crystals by the cooling of a sodium chloride flux." *Crystal growth & design* 11.10 (2011): 4401-4405.

11. Khan, A. I.; O'Hare, D., Intercalation chemistry of layered double hydroxides: recent developments and applications. *Journal of Materials Chemistry* **2002,** *12* (11), 3191-3198.

12. Mugavero III, S. J.; Gemmill, W. R.; Roof, I. P.; zur Loye, H.-C., Materials discovery by crystal growth: Lanthanide metal containing oxides of the platinum group metals (Ru, Os, Ir, Rh, Pd, Pt) from molten alkali metal hydroxides. *Journal of Solid State Chemistry* **2009,** *182* (7), 1950-1963.

13. Bharathy, M.; Fox, A. H.; Mugavero, S.; zur Loye, H.-C., Crystal growth of inter-lanthanide $LaLn'O_3$ (Ln′= Y, Ho–Lu) perovskites from hydroxide fluxes. *Solid state sciences* **2009,** *11* (3), 651-654.

14. Roof, I. P.; Smith, M. D.; zur Loye, H.-C., Crystal growth of K2UO4 and Na_4UO_5 using hydroxide fluxes. *Journal of crystal growth* **2010,** *312* (8), 1240-1243.

15. Stitzer, K. E.; Smith, M. D.; zur Loye, H.-C., Crystal growth of Ba_2MOsO_6 (M= Li, Na) from reactive hydroxide fluxes. *Solid State Sciences* **2002,** *4* (3), 311-316.

16. Tanaka, T.; Ebina, Y.; Takada, K.; Kurashima, K.; Sasaki, T., Oversized titania nanosheet crystallites derived from flux-grown layered titanate single crystals. *Chemistry of materials* **2003,** *15* (18), 3564-3568.

17. Sasaki, T.; Watanabe, M.; Michiue, Y.; Komatsu, Y.; Izumi, F.; Takenouchi, S., Preparation and acid-base properties of a protonated titanate with the lepidocrocite-like layer structure. *Chemistry of materials* **1995,** *7* (5), 1001-1007.

CHAPTER VI

PLUMBONACRITE SYNTHESIS AND CHARACTERIZATION

Introduction

Plumbonacrite is a basic lead carbonate with the formula $Pb_{10}(CO_3)_6O(OH)_6$. This material has not been well studied in literature and, therefore, the synthesis and formation are not very well known. For my research on the formation of $PbTiO_3$ it was extremely important to understand the formation of this carbonate as well as the role this material plays in our system. The synthesis and stability studies of plumbonacrite are described in this chapter.

Plumbonacrite is a basic lead carbonate first discovered in 1889. This material was first observed when lead corrosion started to turn white.[1] The material is an intermediate in the lead oxide carbonization and transforms easily to lead carbonate (hydrocerussite).[2] This material has been studied due to the degradation of orange lead based paints. [3]

This material has been observed in our reactions involving the formation of $PbTiO_3$, as described in Chapter II. Because of its rarity in nature, we decided to synthesize the material so we could study its mechanism of formation as well as the importance of the material in the reactions between lead oxide and TiO_2.

The synthesis of this material is not very well stablished. The process described here yielded the best results in the formation of plumbonacrite in the nanosheet morphology. The process, characterization and reaction studies of this material will be discussed in this chapter.

Experimental

Hydrocerussite synthesis: Method #1: 5.000 g of PCO_3 (18.7 mmol) was added to a 200 mL solution containing 8.000g of K_2CO_3 (57.9 mmol) in a round-bottom flask and left to stir at room temperature for 48 hours. Method #2: Alternatively, 5.000 g of $PbCO_3$ was dispersed in a 200 mL solution of 1 M KOH(aq) and stirred at room temperature for 24 h while maintaining the pH at 11 by the addition of a 0.1 M solution of KOH(aq) as necessary.

Taylor's plumbonacrite synthesis: 5.000 g of hydrocerussite was dispersed in a 200 mL solution containing 13.000g of K_2CO_3 and 2.000g of KOH and stirred for 48 hours at 100 °C. The solid was then centrifuged out at 10,000 RMP and crushed with a mortar and pestle before being returned to the solution to react for 24 hours at 100 °C.

Olby's plumbonacrite synthesis: 200g of litharge (PbO) was suspended in 500 mL of DI water. After that 1 mL of 1M acetic acid was added to the solution and stirred at room temperature. Dry ice was added slowly to the solution to facilitate CO_2 to the reaction. The pH was monitored closely, when the solution reached at pH of 7, the reaction was ended.

Plumbonacrite synthesis: For this reaction, 0.200 g of PbO was added to a solution with 0.02 g of $Pb(C_2H_3O_2)_2$ in 40 mL of DI water in an Erlenmeyer flask creating an orange dispersion. The flask was capped with a rubber stock containing two holes. A 13-gauge needle connected through a tube to a 3-neck round bottom flask was attached to one hole while the other one was left open for release of pressure. 10 mL of DI water were placed in the round bottom flask, which was then placed on a water bath. Dry ice was slowly dropped into the round bottom flask through the top neck while the last neck was used for pressure release. The PbO solution started to change colors to beige and then to white. As soon as the solution started to appear beige, the pH was followed closely. Once the pH reached ~7.4, all the PbO was converted into plumbonacrite.

Characterization details

Powder X-ray diffraction (PXRD) data was collected on a Bruker D8 instrument utilizing a Co−Kα X-ray source (λ = 1.78890 Å) operated at 40 kV and 35 mA. Data was collected from 10 to 80° 2θ with a scan rate of 0.1 s/step. Samples were prepared as powder mounts or drop cast from solution.

Transmission electron microscopy (TEM) imaging and selected area electron diffraction (SAED) analyses were performed using a FEI Tecnai 20 transmission electron microscope with an accelerating voltage of 200 kV. High resolution transmission electron microscopy (HRTEM) was performed with a FEI Tecnai G2 F30 S-TWIN operating at 300 kV. Samples were drop cast onto Formvar, holey carbon, or lacey carbon grids and air dried.

Scanning electron microscopy (SEM) and scanning transmission electron microscopy (STEM) analyses were performed using a FEI Teneo FE-SEM at 10-30 kV with a spot size of 10. Samples were drop cast onto silicon wafer or Formvar grids.

Results and discussion

The chemistry of plumbonacrite has not been very well studied, aside from some reports by archeologists and museums because of the degradation of the paint known as 'red lead'. This paint, famously used by artists like Van Gogh, has been turning white over time. Samples from these paintings have revealed the presence of the basic lead carbonate plumbonacrite, $Pb_{10}(CO_3)_6O(OH)_6$.[3-5]

The first reactions attempted were taken from the synthetic approach published by Taylor et al.[4] This synthetic approach used hydrocerussite $Pb_3(OH)_2(CO_3)_2$ as the precursor for the reactions (a material synthesized by hydrating (cerussite) $PbCO_3$). The synthesis of hydrocerussite was successful and the material was used in the synthesis of plumbonacrite, also published in the same paper by Taylor et al. This reaction of hydrocerussite with potassium carbonate yielded plumbonacrite as well as unreacted hydrocerussite, as shown in **Figure 5.1**.

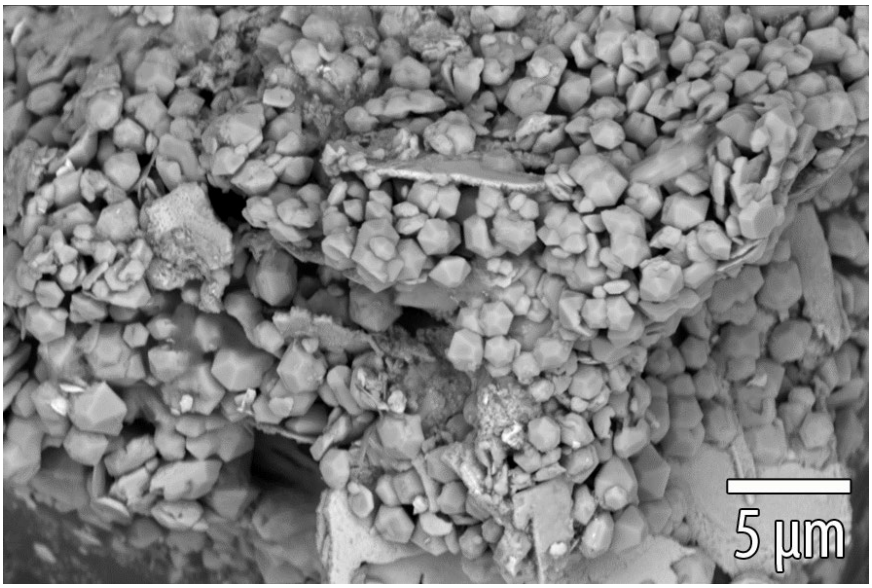

Figure 5.1. Mixture of plumbonacrite and hydrocerussite produced by Taylor's method.

The results from this reaction were not ideal, since the hydrocerussite was still present and the plumbonacrite was not in the nanosheet morphology that we had observed from our reactions. However, by observing the reaction, we could see that the plumbonacrite still grew in hexagonal form (its crystal structure is hexagonal) while the hydrocerussite grew in a platelet morphology as seen in **Figure 5.1**, which made it easy to distinguish.

Next we followed the procedure published by Olby et al. in 1966, to our knowledge the first synthetic approach to plumbonacrite described in a research paper.[7] In their procedure, they utilized 200 g of PbO; we scaled down the amounts for our reaction. After the reaction with acetic acid and CO_2(g) (via dry ice) was done, we observed the same results as from Taylor's method. The reaction mixture contained hydrocerussite, which would then not convert fully into plumbonacrite. **Figure 5.2** shows an SEM image of this product mixture.

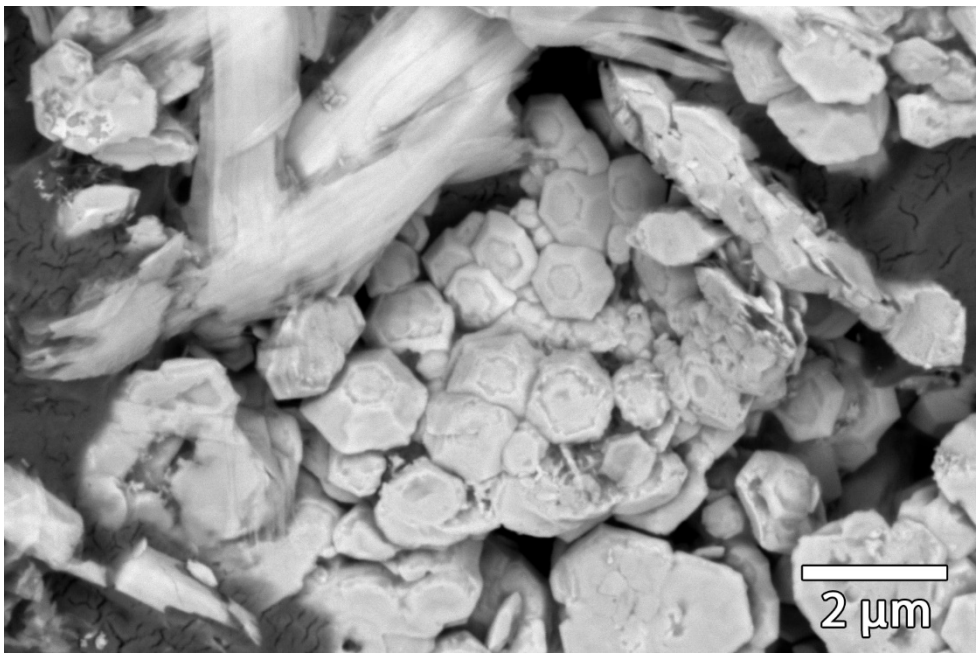

Figure 5.2. SEM image of the product mixture from Olby's plumbonacrite synthesis.

Given these results, we decided to re-examine an obscure citation by Olby et al. in which they mention that Partington was the person to discover this method of synthesizing plumbonacrite. This reference was from a 1950 book with a one-sentence procedure: "A better product [plumbonacrite] is obtained by passing carbon dioxide into a suspension of lead oxide in water containing a little lead acetate".[8] We decided to test this reaction of PbO and $Pb(C_2H_3O_2)_2$ in water. The lead acetate was added in small amounts, but it proved to be crucial in the synthesis of plumbonacrite because it acts as a catalyst for the conversion of PbO to plumbonacrite. After 5 minutes reaction time, we observed most of the orange lead (PbO, litharge) turning into 'white lead' (plumbonacrite).

The pH of the solution was closely monitored for a sign of the reaction going to completion, as research has shown that below the pH of 7, hydrocerussite starts to form.[5] The reaction was stopped when it reached a pH of 7.4, which provided a pearlescent white dispersion. This dispersion was divided into three layers by pipetting the solution into vials. The first, top layer showed greatest pearlescence and the most stable dispersion, whereas the second layer did not stay suspended in water. The third layer contained orange material (litharge, PbO) as well as plumbonacrite that did not disperse well in water.

After imaging the three layers of the solution, we were able to observe the middle layer of the material had both the nanosheet and nano platelets of plumbonacrite, as seen in **Figure 5.3a.** However, the bottom layer of the solution (**Figure 5.3b**) had aggregates of plumbonacrite as well as other lead oxides that (based on the paper) are more likely hydrocerussite. The first layer had the nanosheets of hexagonal plumbonacrite that we were looking for (**Figure 5.3c**) with sizes ranging from 1-4 μm. However, even with these results, we still observed unreacted litharge (PbO) in the solution.

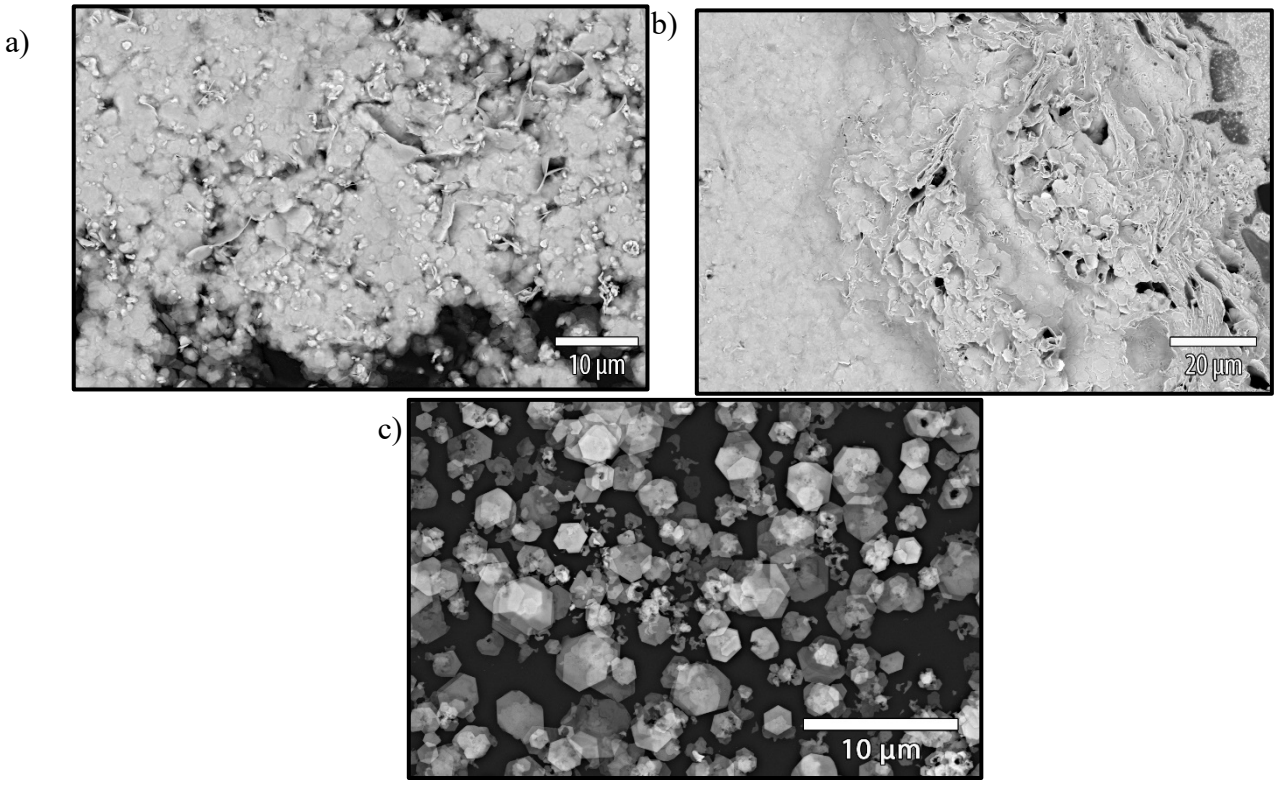

Figure 5.3. a) middle, b) top, and c) top layered of plumbonacrite reaction.

Given the results of the first reaction, we decided to use less starting material with a higher amount of water to prevent the aggregation of plumbonacrite. After the reactions, we were able to obtain a homogeneous dispersion containing no large aggregates of plumbonacrite, but with a nice dispersion of the hexagonal nanosheets. As we can see in **Figure 5.4a**, the hexagonal nanosheets are fully formed. However, after the nanosheets were left on the silicon wafer for 1 month in atmosphere, we started to see the nanosheets degrading and nanorods forming on the surface of the nanosheets (**Figure 5.4b**). After 3 months, the solution turned orange and, after PXRD was performed, we discovered that plumbonacrite degraded into PbO.

a)

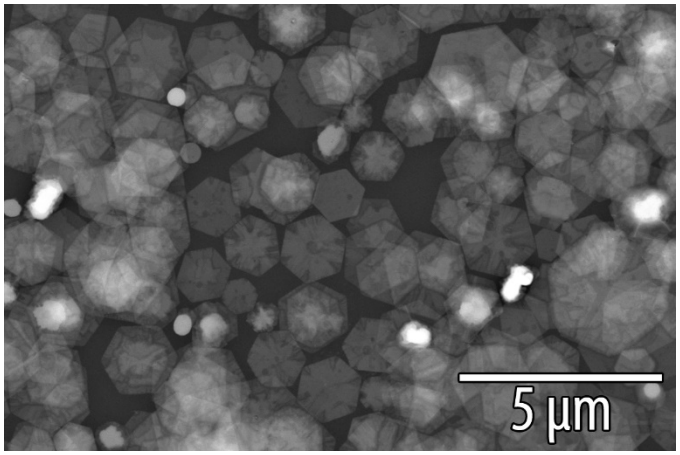

b)

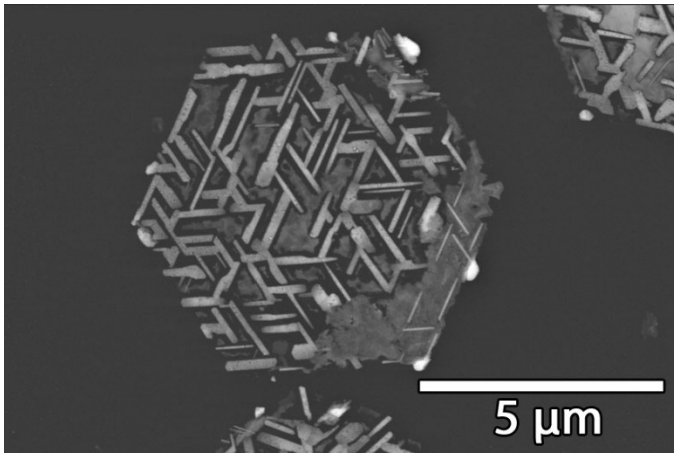

Figure 5.4. a) fresh and b) 1-month-old plumbonacrite.

Conclusion

Plumbonacrite is a basic lead carbonate also known as white lead. This composition has not been well studied in literature, even though this material has been observed extensively throughout history. From lead reactions to Van Gogh's disappearing paintings, it has always been present, yet the formation chemistry of this lead species was not throughly described.

An optimized method to synthesizing plumbonacrite was found, which allowed us to start understanding the importance that pH plays in the formation of this material. This allowed us to pursue a better route to the formation of our $PbTiO_3$ nanosheets. We also were able to observe the stability of plumbonacrite in water under atmospheric conditions. More studies on the stability, as well as the degradation, of plumbonacrite must be performed. Studies to characterize the stability of the nanosheets under an electron beam are in progress.

References

1. Krivovichev, S. V.; Burns, P., Crystal chemistry of basic lead carbonates. II. Crystal structure of synthetic 'plumbonacrite'. *Mineralogical Magazine* **2000,** *64* (6), 1069-1075.

2. Flemming, N. J.; Lopata, V. J.; Sanipelli, B. L.; Taylor, P., Thermal decomposition of basic lead carbonates: a comparison of hydrocerussite and plumbonacrite. *Thermochimica acta* **1984,** *81*, 1-8.

3. Gonzalez, V.; Cotte, M.; Wallez, G.; van Loon, A.; de Nolf, W.; Eveno, M.; Keune, K.; Noble, P.; Dik, J., Unraveling the Composition of Rembrandt's Impasto through the Identification of Unusual Plumbonacrite by Multimodal X-ray Diffraction Analysis. *Angewandte Chemie* **2019,** *131* (17), 5675-5678.

4. Corbeil, M.-C.; Sirois, P. J., A Note on a Modern Lead White, also Known as' Synthetic Plumbonacrite'. *Studies in conservation* **2007,** *52* (4), 281-288.

5. Vanmeert, F.; Van der Snickt, G.; Janssens, K., Plumbonacrite identified by X-ray powder diffraction tomography as a missing link during degradation of red lead in a Van Gogh painting. *Angewandte Chemie* **2015,** *127* (12), 3678-3681.

6. Taylor, P.; Lopata, V. J., Stability and solubility relationships between some solids in the system PbO–CO2–H2O. *Canadian Journal of Chemistry* **1984,** *62* (3), 395-402.

7. Olby, J., The basic lead carbonates. *Journal of Inorganic and Nuclear Chemistry* **1966,** *28* (11), 2507-2512.

8. Partington, J. R. *A text-book of inorganic chemistry*; 1950.

CHAPTER VI

CONCLUSIONS AND FUTURE OUTLOOK

Lead Titanate - $PbTiO_3$

In Chapters II and III I detail the synthesis and characterization of novel $PbTiO_3$ nanosheets, grown by a templated growth method with a TiO_2(B) nanosheet precursor. These nanosheets have a thickness of ~5 nm, according to AFM analysis. The study of the formation of the nanosheets lead us to synthesize the basic lead carbonate plumbonacrite [$(Pb_{10}(CO_3)_6O(OH)_6$]. We had to synthesize this compound since it was always observed in our reactions, and we needed to know if the product was needed to yield the nanosheet of $PbTiO_3$ or if it was an unnecessary side product.

The research for the answer took us down 3 different pathways to synthesize the nanosheets, all using the same templated growth hydrothermal approach. The precursors used were nanosheets of $(TBA)_{1.07}Ti_{1.73}O_4$ (previously synthesized by Sasaki et al.)[1] that were treated with $Pb(NO_3)_2$ in order to exchange the TBA^+ ion for Pb^{2+} ions, forming what we called the Pb_x-TiO_2 flocculate. For the lead salt, after several studies were performed, we discovered that PbO was the best salt to be utilized in these studies (yielded the best results). Once the precursors were chosen, we started to study their reactivity under different conditions.

The first set of conditions was under normal atmosphere with a ratio of 1:2 Pb_x-TiO_2:PbO. These reactions resulted in the formation of $PbTiO_3$ nanosheets as well as plumbonacrite nanosheets. The nanosheets of $PbTiO_3$ were hard to isolate, since dissolving the plumbonacrite in

acid also resulted in the breakage of the nanosheets and the formation of more plumbonacrite. Given the difficulty we had isolating the nanosheets of $PbTiO_3$, more studies started to garner a higher importance.

The second set of conditions we tried was to create a solution with a pH lower than the pH for the formation of plumbonacrite(~7.4),[2] which we achieved by the addition of 1M HCl solution. As soon as the acid was added to the solution, a change in color was observed. The more acid that was added, the more the solution turned transparent, which we correlated to the fact that the PbO (litharge) was reacting with the HCl to create $PbCl_2$. Once all the PbO turned into $PbCl_2$ (pH~4), no reaction occurred with the Pb_x-TiO_2 nanosheets. After optimizing the pH of the solution, it was found that pH ~6.88 yielded the best results. The solutions resulted in the formation of $PbTiO_3$ nanosheets with no plumbonacrite forming. However, PXRD showed a side product of Ti_4O_7.

The nanosheets were studied under high resolution TEM and the results showed two different morphologies of nanosheets. The first was a granulated nanosheet with clear crystalline domains that matched to the (101) plane of $PbTiO_3$ (JCPDS #00-066-0336) with a *c/a* ratio of 1.051 confirming the structure to be tetragonal. The second morphology was nanosheets of $PbTiO_3$ which were single crystalline and also matched to (101) plane of $PbTiO_3$ after performing FFT calculations and atomic resolutions studies. These nanosheets had a *c/a* ratio of 1.047, confirming that these nanosheets are also in the tetragonal structure.

After the pH reactions, another set of conditions tried were N_2 atmosphere reactions, because plumbonacrite requires CO_2 from the atmosphere to form. For the reactions, we converted an old glove box into what we called a “wetbox” to provide a CO_2-free environment to prepare the hydrothermal reactions. The Pb_x-TiO_2 flocculate proved to be more of a challenge since the drying

of this material by heat or vacuum results in the restacking of the nanosheets. Because of this reason, the nanosheets of Pb_x-TiO_2 had to be freeze-dried before being used in the wet box.

The results showed the formation of $PbTiO_3$ nanosheets as well as excess PbO left after the reaction was done. This was clearly visible since the orange color of PbO is very clear, as well as by PXRD. Given these results, the ratio used between Pb_x-TiO_2 and PbO had to be adjusted. After many tests, we concluded that when the PbO: Pb_x-TiO_2 ratio is higher than 1.67:1, the reaction will have excess PbO. Any lower and the reaction will have unreacted Pb_x-TiO_2 nanosheets. However, when the ratio of Pb_x-TiO_2:PbO is 1:1.67, the reactions yielded nanosheets of $PbTiO_3$, and plumbonacrite did not form even after the solution was exposed to CO_2.

The results of the N_2 atmosphere reactions helped us understand that the excess PbO readily reacts with atmospheric CO_2 to create plumbonacrite. These results led us to the next and final set of conditions for this system, the optimized ratio between Pb_x-TiO_2:PbO of 1:1.67. Once these reactions were done even under atmospheric reactions, no plumbonacrite is observed; instead, $PbTiO_3$ nanosheets are formed. High resolution TEM studies showed that the nanosheets matched to the (100) plane of $PbTiO_3$ (JCPDS #00-066-0336) and had a *c/a* ratio of 1.021 confirming that the nanosheets have a tetragonal crystal structure.

After the formation of the nanosheets, diffuse reflectance studies were made on the material to test their band gap by utilizing the Kubelka-Monk method.[3] These calculations gave us a direct allow band gap of 2.18, making it lower than previously shown nanomaterials of $PbTiO_3$[4-5] in literature. However, these results cannot be altogether taken at face value since it was a mixture of $PbTiO_3$ and Ti_4O_7 and the solid was, therefore, not phase pure. With these results, die degradation studies were performed to test their photocatalytic abilities showing a maximum decay rate of

0.062 h^{-1}. The low photocatalytic activity can be explained by the fact that the nanosheets of $PbTiO_3$ are not stable in water and they start to degrade when light hits them.

Overall, nanosheets of tetragonal $PbTiO_3$ were synthesized by 3 different routes. Their size has proven to be hard to characterize because the material is extremely small and tends to stick to the AFM probe. Diffuse reflectance studies yielded an optical band gap of 2.87 eV, a very small band gap that can be extremely useful for photocatalytic studies. However, since the material was not pure, we cannot fully state that the band gap calculated was of our nanosheets of $PbTiO_3$. Even then, we performed dye degradation studies with our material to study their catalytic activity. The result showed us that our nanosheets were not stable in water when exposed to light. Even with these results, a lot more must be done for this system. The AFM has been proven hard to perform with the nanosheets being so small and with their tendency to move under the probe. More studies on the affinity of our nanosheets with different substrates will be required in order to study the properties of the material, such as the piezoelectric and ferroelectric response of the $PbTiO_3$ nanosheets.

Barium titanate - $BaTiO_3$

Nanosheets of $BaTiO_3$ were synthesized by a templated flux-based method. The reactions utilized a H_x-TiO_2 flocculate as the template with $Ba(OH)_2 \bullet 8H_2O$ as the barium salt and the flux. The reactions with the autoclaves resulted in nanoparticles of $BaTiO_3$. Therefore, a Schlenk tube vessel was used that would allow the water to not evaporate while the material got heated to 120 °C.

After some optimization, the nanosheets of $BaTiO_3$ were synthesized and characterized by STEM coupled with EDS, PXRD, and Raman. Although PXRD showed the nanosheets to be $BaTiO_3$ (JCPDS #00-005-0626), EDS analysis showed a 1:3 Ba:Ti ratio. Raman studies showed peaks at 250 cm^{-1}, 307 cm^{-1}, and 715 cm^{-1} which correlates to the (A_1(TO)), (B_1, E(TO + LO)), and (A_1(LO), E(LO)) active modes. However, the peak at 515 cm^{-1} corresponding to the active mode (A_1(TO), E(TO)) was not observed.[6] Even after these characterizations, a lot more studies must be performed in the system. High resolution TEM and atomic resolution studies are needed in order to confirm the structure of $BaTiO_3$. After confirming the structure, AFM and PFM studies must be performed to calculate their thickness as well as their piezoelectric and ferroelectric response.

Strontium titanate - $SrTiO_3$

Efforts to synthesize nanosheets of $SrTiO_3$ have been performed by utilizing the same method as the $BaTiO_3$ reactions with promising results. Even though the nanosheets that have been synthesized so far are strontium deficient, the templated growth method seems to be working for this system as well. More studies on the necessary ratio of the precursors, as well as the strontium salts being used in the system, must be performed.

In conclusion, nanosheets of the inorganic perovskite family of materials have been synthesized. $PbTiO_3$ was synthesized by a templated growth method under hydrothermal conditions while $BaTiO_3$ and $SrTiO_3$ nanosheets were synthesized using a templated growth solid-state method. The materials used in this system proved to be useful in synthesizing the nanosheets in the tetragonal form of $PbTiO_3$ and possibly $BaTiO_3$. These results confirm that a considerable amount of studies must still be performed in the systems to fully characterize the nanosheets and their properties.

References

1. Tanaka, T.; Ebina, Y.; Takada, K.; Kurashima, K.; Sasaki, T., Oversized titania nanosheet crystallites derived from flux-grown layered titanate single crystals. *Chemistry of materials* **2003,** *15* (18), 3564-3568.

2. Olby, J., The basic lead carbonates. *Journal of Inorganic and Nuclear Chemistry* **1966,** *28* (11), 2507-2512.

3. Myrick, M. L.; Simcock, M. N.; Baranowski, M.; Brooke, H.; Morgan, S. L.; McCutcheon, J. N., The Kubelka-Munk diffuse reflectance formula revisited. *Applied Spectroscopy Reviews* **2011,** *46* (2), 140-165.

4. Robertson, J., Band offsets of wide-band-gap oxides and implications for future electronic devices. *Journal of Vacuum Science & Technology B: Microelectronics and Nanometer Structures Processing, Measurement, and Phenomena* **2000,** *18* (3), 1785-1791.

5. Piskunov, S.; Heifets, E.; Eglitis, R.; Borstel, G., Bulk properties and electronic structure of $SrTiO_3$, $BaTiO_3$, $PbTiO_3$ perovskites: an ab initio HF/DFT study. *Computational Materials Science* **2004,** *29* (2), 165-178.

6. Gajović, A.; Pleština, J. V.; Žagar, K.; Plodinec, M.; Šturm, S.; Čeh, M., Temperature-dependent Raman spectroscopy of $BaTiO_3$ nanorods synthesized by using a template-assisted sol–gel procedure. *Journal of Raman Spectroscopy* **2013,** *44* (3), 412-420.